Title
Efficient Methods for Calculating and Analyzing Excited States in Molecular Complexes

Author
Ge, Qinghui

Publication Date
2019

Efficient Methods for Calculating and Analyzing Excited States in Molecular Complexes

by

Qinghui Ge

A dissertation submitted in partial satisfaction of the

requirements for the degree of

Doctor of Philosophy

in

Chemistry

in the

Graduate Division

of the

University of California, Berkeley

Committee in charge:

Professor Martin P. Head-Gordon, Chair
Professor K. Birgitta Whaley
Professor Jeffrey B. Neaton

Spring 2019

Efficient Methods for Calculating and Analyzing Excited States in Molecular Complexes

Abstract

Efficient Methods for Calculating and Analyzing Excited States in Molecular Complexes

by

Qinghui Ge

Doctor of Philosophy in Chemistry

University of California, Berkeley

Professor Martin P. Head-Gordon, Chair

Understanding excited states is vital to photochemistry and spectroscopy, yet the study of excited states from a theoretical viewpoint is often much more challenging than that of ground states due to the more complicated nature of excited states systems. This thesis is primarily focused on a series of topics regarding excited state electronic structure theory, aiming to improve the accuracy, efficiency and interpretability of computational methods. In particular, we generalize the recently developed ALMO-CIS approach, which is a formulation of configuration interaction singles (CIS) for molecular complexes or clusters based on absolutely-localized molecular orbitals (ALMOs), in two ways. The first is to reintroduce charge-transfer (CT) effects, and the resulting ALMO-CIS+CT method is shown to provide better accuracy in simulating spectra of large helium clusters. Secondly, a multi-reference version of ALMO-CIS is formulated, and shown to be a promising method for systems where pure charge-transfer excitations are important. We also develop and implement an energy decomposition analysis (EDA) method for studying intermolecular interactions in excited molecular systems. This EDA scheme brings insight to interesting excited-state phenomena such as solvatochromism, charge-transfer-to-solvent (CTTS) spectrum and the formation of excimers.

Contents

List of Figures

List of Tables

Acknowledgments

I would like to thank my advisor, Professor Martin Head-Gordon for his encouragement and support during the past five years. The weekly meetings with Martin have always been a pleasant and memorable experience for me to learn about scientific problems and his way of thinking. I'd like to thank people in the Head-Gordon group for providing a collaborative and inspiring working environment. In specific, I'd like to thank Dr. Kristi Closser for helping me get started with my research work, Dr. Alec White for helping me with hard-core code development, Dr. Narbe Mardirossian for trouble shooting all kinds of technical issues, and Dr. Yuezhi Mao for providing expert advice about energy decomposition analysis and Q-Chem development, as well as being a wonderful companion in life.

I would also like to thank Shirley Tan, who has been my language partner since I started my graduate school. We have shared many great weekends and I learned many interesting things about America from her.

Finally, I would like to thank my parents. They always give me unconditional love and support even though they don't quite understand the work I am doing.

Chapter 1

Introduction

1.1 Quantum Chemistry

1.1.1 Schrödinger Equation

In quantum mechanics[1–3], the Schrödinger equation models the state of a microscopic system. For a chemical system, the state is described by a wavefunction $\Psi(\mathbf{r}, \mathbf{R}, t)$, which is fully defined by the electron position vector $\mathbf{r}$, the nuclei position vector $\mathbf{R}$ and the time t. The most general form of the Schrödinger equation is the time-dependent Schrödinger equation:

$$\hat{H}\Psi(\mathbf{r}, \mathbf{R}, t) = i\hbar\frac{\partial}{\partial t}\Psi(\mathbf{r}, \mathbf{R}, t) \tag{1.1}$$

When the Hamiltonian $\hat{H}$ does not depend on time explicitly, the wavefunction Ψ can be separated into a spatial part $\Phi(\mathbf{r}, \mathbf{R})$ and a time part $T(t)$. The spatial wavefunction can be solved from the time-independent Schrödinger equation:

$$\hat{H}\Phi(\mathbf{r}, \mathbf{R}) = E\Phi(\mathbf{r}, \mathbf{R}) \tag{1.2}$$

and the total wavefunction can then be expanded as:

$$\Psi(\mathbf{r}, \mathbf{R}, t) = \sum_n \Phi_n(\mathbf{r}, \mathbf{R})T_n(t) \tag{1.3}$$

where Φ_n is the eigensolution of eq. 1.2 with eigenvalue E_n, and $T_n(t) = e^{-iE_nt}$ as solved from $i\hbar\frac{\partial}{\partial t}T(t) = E_nT(t)$.

The Hamiltonian $\hat{H}$ can be further split into kinetic energy terms (for both electrons and nuclei) and potential energy terms that comprise electron-electron, electron-nuclei and nuclei-nuclei Coulomb interactions, i.e.

$$\begin{aligned}\hat{H} &= \hat{T}_{\mathrm{e}} + \hat{T}_{\mathrm{n}} + \hat{V}_{\mathrm{ne}} + \hat{V}_{\mathrm{ee}} + \hat{V}_{\mathrm{nn}} \\ &= -\sum_{i=1}^{n}\frac{1}{2}\nabla_i^2 - \sum_{A=1}^{N}\frac{1}{2m_A}\nabla_A^2 - \sum_{i=1}^{n}\sum_{A=1}^{N}\frac{Z_A}{|\mathbf{r}_i - \mathbf{R}_A|} \\ &\quad + \sum_{i=1}^{n}\sum_{j>i}^{n}\frac{1}{|\mathbf{r}_i - \mathbf{r}_j|} + \sum_{A=1}^{N}\sum_{B>A}^{N}\frac{Z_A Z_B}{|\mathbf{R}_A - \mathbf{R}_B|},\end{aligned} \tag{1.4}$$

where we have assumed that the system is comprised of n electrons and N nuclei. m_A, Z_A, $\mathbf{R}_A$ are the mass, charge and coordinate for nucleus A; $\mathbf{r}_i$ is the coordinate of electron i. Note that the equation is expressed in atomic units. Unfortunately, the Schrödinger equation in this form is unfeasible to be solved exactly except for very small systems. Thus, we have to resort to various approximations. Applying valid approximations to reduce the complexity of the Schrödinger equation is an essential challenge in quantum chemistry, and we will introduce some of the fundamental approximations in the following sections.

1.1.2 The Born-Oppenheimer Approximation

The Born-Oppenheimer Approximation[4, 5] is a simplification to the time-independent Schrödinger equation (eq. 1.2). The approximation utilizes the fact that the nuclei are at least 1800 times heavier than the electrons and move much slower. Thus, the electrons can be viewed as moving in a Coulomb potential generated by fixed nuclei, and the spatial wavefunction can be factorized as a product of electronic wavefunction Ψ_e and nuclei wavefunction Θ:

$$\Phi(\mathbf{r}, \mathbf{R}) = \Psi_e(\mathbf{r}; \mathbf{R})\Theta(\mathbf{R}) \tag{1.5}$$

where Θ only depends on the nuclei coordinates $\mathbf{R}$. $\Psi_{\mathrm{e}}(\mathbf{r}; \mathbf{R})$ is the adiabatic wavefunction that parametrically depends on $\mathbf{R}$. It can be obtained as the eigenstates of the electronic Schrödinger equation:

$$\hat{H}_e\Psi_{\mathrm{e}}(\mathbf{r}; \mathbf{R}) = E_{\mathrm{e}}(\mathbf{R})\Psi_{\mathrm{e}}(\mathbf{r}; \mathbf{R}) \tag{1.6}$$

with the electronic Hamiltonian $\hat{H}_e$ defined under a fixed nuclei configuration $\mathbf{R}$:

$$\hat{H}_e = \left(-\sum_{i=1}^{n}\frac{1}{2}\nabla_i^2 - \sum_{i=1}^{n}\sum_{A=1}^{N}\frac{Z_A}{|\mathbf{r}_i - \mathbf{R}_A|} + \sum_{i=1}^{n}\sum_{j>i}^{n}\frac{1}{|\mathbf{r}_i - \mathbf{r}_j|}\right) \tag{1.7}$$

The electronic energy $E_e(\mathbf{R})$ along with the nuclei potential $V_{nn}(\mathbf{R})$ defines the potential energy surface (PES) $V(\mathbf{R})$ that is a function of nuclear coordinates ($\mathbf{R}$):

$$V(\mathbf{R}) = E_{\mathrm{e}}(\mathbf{R}) + V_{nn}(\mathbf{R}) \tag{1.8}$$

$V(\mathbf{R})$ is often regarded as the “total” energy of a system and utilized as a metric of system stability at varying nuclei configurations. In the following chapters, we will be looking at PES constantly especially when discussing the intermolecular interactions.

The Born-Oppenheimer approximation can break down when the adiabatic states are close in energy. In such cases one has to expand the total wavefunction in terms of products of adiabatic wavefunction $\Psi_{\mathrm{e}}^{(m)}(\mathbf{r};\mathbf{R})$ and the associated nuclear wavefunction $\Theta_n^{(m)}(\mathbf{R})$ and consider the nonadiabatic (derivative) coupling between electronic states.

1.1.3 The Hartree-Fock Theory

The exact solution to the electronic Schrödinger equation (eq. 1.6) is still hard to find because the electronic Hamiltonian (eq. 1.7) contains a potential energy term that couples every pair of electrons. It would greatly simplify the equation if the electronic Hamiltonian can be approximated as a sum of one-electron operators, so that eq. 1.6 can be reduced to a set of one-particle eigenvalue problems. The Hartree-Fock theory achieves this through the mean-field approximation, i.e., each electron is moving in the mean-field potential created by all other electrons. The approximated wavefunction has the form of an antisymmetric product of one-particle wavefunctions, i.e. a Slater determinant[6]:

$$\Psi_e = \frac{1}{\sqrt{n!}} \begin{vmatrix} \chi_1(q_1) & \chi_1(q_2) & \cdots & \chi_1(q_n) \\ \chi_2(q_1) & \chi_2(q_2) & \cdots & \chi_2(q_n) \\ \vdots & \vdots & \ddots & \vdots \\ \chi_n(q_1) & \chi_n(q_2) & \cdots & \chi_n(q_n) \end{vmatrix}, \tag{1.9}$$

where $q_i = \{\mathbf{r_i}, \sigma_i\}$ is a combination of electron i's spatial and spin degrees of freedom. The single particle wavefunction χ is called a spin-orbital, which is the product of a spatial orbital $\psi(\mathbf{r})$ and the spin function $\alpha(\sigma)$ or $\beta(\sigma)$.

The variational principle[3, 6] states that minimizing the energy expectation value of any trial wavefunction gives an upper bound to the true ground state energy. For the wavefunction in the form of a Slater determinant, we can find the expectation value of the energy:

$$\begin{aligned} E_0 &= \langle \Psi_e | \hat{H}_e | \Psi_e \rangle \\ &= \sum_{i=1}^{n} \langle \chi_i | h_i | \chi_i \rangle + \frac{1}{2} \sum_{i=1}^{n} \sum_{j=1}^{n} \langle \chi_i \chi_j | \frac{1}{r_{ij}} | \chi_i \chi_j \rangle - \langle \chi_i \chi_j | \frac{1}{r_{ij}} | \chi_j \chi_i \rangle \\ &= \sum_{i=1}^{n} \langle \chi_i | h_i | \chi_i \rangle + \frac{1}{2} \sum_{i=1}^{n} \sum_{j=1}^{n} \langle \chi_i \chi_j || \chi_i \chi_j \rangle \end{aligned} \tag{1.10}$$

where

$$h_i = -\frac{1}{2}\nabla_i^2 - \sum_A \frac{Z_A}{|\mathbf{r}_i - \mathbf{R}_A|} \tag{1.11}$$

is a one-electron operator, and the antisymmetrical integral, $\langle \chi_i \chi_j || \chi_i \chi_j \rangle$, is a compact way to put together the Coulomb integral $\langle \chi_i \chi_j | \frac{1}{r_{ij}} | \chi_i \chi_j \rangle$ and the exchange integral $\langle \chi_i \chi_j | \frac{1}{r_{ij}} | \chi_j \chi_i \rangle$.

A common practice is to express the spatial part of a one-particle wavefunction as a linear combination of atomic orbital (AO) basis functions $\omega_\mu(\mathbf{r})$: $\psi_i(\mathbf{r}) = \sum_\mu \omega_\mu(\mathbf{r}) C_{\mu i}$, and the ground state energy can be written in terms of AO functions and molecular orbital (MO) coefficients $C_{\mu i}$:

$$\begin{aligned} E_0 &= \sum_{\mu\nu}\sum_{i} C_{\mu i}C_{\nu i}\langle\mu|h|\nu\rangle + \frac{1}{2}\sum_{\mu\nu\lambda\sigma}\sum_{ij} C_{\mu i}C_{\nu i}C_{\lambda j}C_{\sigma j}\langle\mu\lambda||\nu\sigma\rangle \\ &= \sum_{\mu\nu}(P_{\mu\nu}H_{\mu\nu}) + \frac{1}{2}\sum_{\mu\nu}P_{\mu\nu}(J_{\mu\nu} - K_{\mu\nu}) \end{aligned} \tag{1.12}$$

where $P_{\mu\nu} = \sum_i C_{\mu i}C_{\nu i}$ is called the density matrix, $H_{\mu\nu} = \langle\mu|h|\nu\rangle$ is the core Hamiltonian, $J_{\mu\nu} = \sum_{\lambda\sigma} P_{\lambda\sigma}\langle\mu\lambda|\nu\sigma\rangle$ and $K_{\mu\nu} = \sum_{\lambda\sigma} P_{\lambda\sigma}\langle\mu\lambda|\sigma\nu\rangle$ are the Coulomb and Exchange matrix, respectively.

Minimizing E_0 subject to the constraint that $\langle\chi_i|\chi_i\rangle = \sum_{\mu\nu} C_{i\mu}C_{i\nu}\langle\mu|\nu\rangle = 1$ gives the Hartree-Fock equation[6, 7]:

$$\mathbf{FC} = \mathbf{SC}\boldsymbol{\epsilon} \tag{1.13}$$

where $F_{\mu\nu} = H_{\mu\nu} + J_{\mu\nu} - K_{\mu\nu}$ is the Fock operator, $S_{\mu\nu} = \langle\mu|\nu\rangle$ is the overlap matrix. The eigenvalues of this generalized eigenvalue problem, $\boldsymbol{\epsilon}$, are the orbital energies. When employing an atomic basis set of size M (typically $M \gg n$, the number of electrons), the lowest n eigenvectors solved from eq. 1.13 are the occupied orbitals used to construct the Slater determinant. The remaining $M - n$ orbitals are called the unoccupied or virtual orbitals, which represent higher single-particle energy levels.

The Hartree-Fock equations are solved through a self-consistent field (SCF) procedure, as the Fock operator depends on MO coefficients $\mathbf{C}$ through the density matrix. In practical calculations, the choice of how to construct spin-orbitals would give rise to different flavors of SCF. For closed-shell systems, restricted Hartree-Fock (RHF) is commonly used, where the spatial orbitals are constrained to be the same for α and β electrons, and the form of the Hartree-Fock equation can be further simplified. For open-shell systems, one can choose to employ different sets of spatial orbitals for α and β electrons, or retain the constraint that α and β electrons share a common set of spatial orbitals, leading to unrestricted Hartree-Fock (UHF) and restricted open-shell Hartree-Fock (ROHF) theory, respectively.

The Hartree-Fock theory is perhaps the simplest method for ground state electronic structure theory. While successful in many cases, the Hartree-Fock method neglects dynamical electron correlation as the mean-field approximation is applied, which can result in large deviations from experimental results for properties such as bond dissociation energies. [8] Moreover, as a single Slater determinant is employed to construct system's electronic wavefunction, the Hartree-Fock theory is incapable of describing systems of multireference character where static correlation prevails. Considering the covalent bond in H_2 and its dissociation, RHF underestimates the bond energy at equilibrium distance (compared to the exact theoretical value) due to lack of dynamical correlation, and it yields an incorrect dissociation limit as the RHF wavefunction still has 50% ionic character even when two H atoms are infinitely separated, which is unphysical for the homolysis of H_2. UHF, on the other hand, gives the correct dissociation behavior energetically at the cost of spin symmetry breaking: the resulting electronic wavefunction is either H(α)$\cdots$H(β) or H(β)$\cdots$H(α).

[6] Also, due to the mix with the higher-energy triplet state, UHF still underestimates the binding energy compared to the exact result.

1.2 Excited State Electronic Structure Theory

1.2.1 Configuration Interaction Singles and Beyond

Configuration Interaction Singles (CIS)[9, 10] is the simplest and most intuitive *ab initio* method for electronic excited states. Starting from the ground state wavefunction, which is a Slater determinant constructed by the n occupied orbitals (eq. 1.9), one can replace an occupied orbital i by a virtual orbital a to form a singly substituted determinant $|\Psi_a^i\rangle$, and the CIS wavefunction is a linear combination of all possible such single excitations:

$$|\Psi_{ex}\rangle = \sum_i^{\text{occ}} \sum_a^{\text{virt}} t_i^a |\Psi_a^i\rangle \tag{1.14}$$

The single excitations are orthogonal to the ground state wavefunction. In addition, the Brillouin's theorem[11] states that the single excitations do not couple with the ground state through the Hamiltonian, i.e. $\langle\Psi_{gs}|\hat{H}_e|\Psi_a^i\rangle = 0$. As a result, the coefficients t_i^a can be variationally determined by projecting the time-independent Schrödinger equation into the space of single substituted determinants:

$$\sum_{jb} \langle\Psi_b^j|\hat{H}_e|\Psi_a^i\rangle t_j^b = E_{\text{CIS}} \sum_{jb} t_j^b \delta_{ij}\delta_{ab} \tag{1.15}$$

with the matrix elements computed as:

$$\langle\Psi_b^j|\hat{H}_e|\Psi_a^i\rangle = (E_0 + \epsilon_a - \epsilon_i)\delta_{ij}\delta_{ab} + \langle\chi_i\chi_b||\chi_a\chi_j\rangle \tag{1.16}$$

Subtracting the ground state energy E_0 on both sides, we obtain the eigenvalue equation for excitation energy $\omega = E_{\text{CIS}} - E_0$:

$$\mathbf{At} = \omega\mathbf{t} \tag{1.17}$$

with

$$A_{ia,jb} = (\epsilon_a - \epsilon_i)\delta_{ij}\delta_{ab} + \langle\chi_i\chi_b||\chi_a\chi_j\rangle \tag{1.18}$$

which is a standard eigenvalue problem that can be solved using either direct or iterative methods[12, 13].

Just like Hartree-Fock theory, CIS neglects dynamical electron correlation. This will inevitably introduce an error in CIS excitation energies unless the magnitude of correlation energy is similar in ground and excited states. For the ground state, dynamical correlation can be treated using post-Hartree-Fock methods such as Configuration Interaction (CI)[14, 15], Møller-Plesset perturbation theory (MP)[16, 17], and Coupled-Cluster theory (CC)[18, 19]. Analogous ideas can be applied to excited states. For example, CIS(D)[20] is the analog of second-order Møller-Plesset perturbation theory applied to CIS states; EOM-CCSD[21] (equation-of-motion coupled cluster singles and doubles) is related to ground-state CCSD. All these methods incorporate higher-order excitations into the multi-electron wavefunction in order to account for dynamical correlation. The correct treatment of static correlation is also of great importance in modeling excited states, especially for open-shell systems and special points on potential energy surface where two electronic states are close to each other in energy. A common strategy is to include multiple important configurations or references when constructing the wavefunction, which is adopted in methods like multireference CI (MRCI)[22, 23], multi-configurational self-consistent field (MCSCF), [24, 25] and spin-flip approaches. [26–28]

1.2.2 Time-Dependent Density Functional Theory

Besides the above mentioned wavefunction-based methods, there exists another family of methods based on electron density in quantum chemistry that takes dynamical correlation into consideration. The density functional theory (DFT) is based on the first and second Hohenberg-Kohn theorems: [29] (i) the ground state properties of a many-electron system are uniquely determined by the electron density; (ii) the correct electron density minimizes the ground state energy. In the Kohn-Sham formalism[30], the density of a given system is mapped to the density of a non-interacting fictitious system, whose wavefunction is a single Slater determinant constructed from a set of orbitals obtained from solving the Kohn-Sham equation:

$$\left[-\frac{1}{2}\nabla^2 + v_{\text{eff}}(\mathbf{r})\right]\psi(\mathbf{r}) = \epsilon\psi(\mathbf{r}) \tag{1.19}$$

where $v_{\text{eff}} = v_{\text{ext}} + v_{\text{J}} + v_{\text{xc}}$ is the effective potential consisting of three parts: the external potential, $v_{\text{ext}}(\mathbf{r}) = \sum_A Z_A/|\mathbf{r} - \mathbf{R}_A|$ for a molecular system (with nuclear-electron attraction only); the classical Coulomb interaction between electrons, $v_{\text{J}}(\mathbf{r}) = \int \frac{\rho(\mathbf{r})}{|\mathbf{r}-\mathbf{r}'|}\mathrm{d}\mathbf{r}'$; an exchange-correlation (XC) potential that accounts the remaining non-classical contribution to electron-electron interaction, $v_{\text{xc}}(\mathbf{r}) = \delta E_{\text{xc}}[\rho]/\delta\rho(\mathbf{r})$. In the AO basis, the Kohn-Sham equation is in the same form as the Hartree-Fock equation (eq. 1.13), with the effective one-electron Hamiltonian (analogous to the Fock matrix) being $\mathbf{F}^{\text{KS}} = \mathbf{H} + \mathbf{J} + \mathbf{V}_{\text{xc}}$.

The time-dependent density functional theory (TDDFT)[9, 31–33] is an extension of DFT for time-dependent electronic densities. The linear response formalism of TDDFT is a widely used method for studying excited states. The excitation energy is obtained by calculating the response of the ground state density to an external electric field that oscillates with time, which reduces to solving the following eigenvalue equation:

$$\begin{pmatrix} \mathbf{A} & \mathbf{B} \\ \mathbf{B}^* & \mathbf{A}^* \end{pmatrix}\begin{pmatrix} \mathbf{X} \\ \mathbf{Y} \end{pmatrix} = \omega \begin{pmatrix} 1 & 0 \\ 0 & -1 \end{pmatrix}\begin{pmatrix} \mathbf{X} \\ \mathbf{Y} \end{pmatrix} \tag{1.20}$$

where the matrix elements of **A** and **B** are defined by:

$$A_{ia,jb} = (\epsilon_a - \epsilon_i)\delta_{ij}\delta_{ab} + \langle \chi_i \chi_b | \chi_a \chi_j \rangle + \langle \chi_i \chi_b | f_{\text{xc}} | \chi_a \chi_j \rangle \tag{1.21}$$

$$B_{ia,jb} = \langle \chi_i \chi_a | \chi_b \chi_j \rangle + \langle \chi_i \chi_a | f_{\text{xc}} | \chi_b \chi_j \rangle \tag{1.22}$$

where $f_{\text{xc}} = \delta^2 E_{\text{xc}}/\delta\rho(\mathbf{r})\delta\rho(\mathbf{r}')$ is the exchange-correlation kernel (second derivative of the XC energy with respect to electron density). Vectors **X** and **Y** represent the excitation and de-excitation amplitudes. In Tamm-Dancoff approximation (TDA)[34], matrix **B** is neglected, and eq. 1.20 resembles the CIS equation (eq. 1.17), with the exchange term in matrix **A** replaced by the exchange-correlation term.

The computational cost of TDDFT and TDA is comparable to that of CIS, while in many cases TDDFT/TDA offers better accuracy as dynamical electron correlation is incorporated through the use of DFT. However, TDDFT and TDA are not without disadvantages. They suffer from self-interaction error and often qualitatively fail for excited states of charge-transfer or Rydberg character[35]. In addition, the performance of TDDFT/TDA often strongly depends on the density functional employed, and choosing the best functional often involves trial and error, which may introduce extra complexity.

In summary, CIS is usually a good starting point for computational modeling of excited states, and therefore most of the method development in this thesis is based on or exemplified with CIS. In the meantime, we also employ TDDFT or TDA for certain applications when we believe that they offer better accuracy, as well as other high-level methods to provide reference data from time to time.

1.3 Intermolecular Interaction for Excited States

1.3.1 Chemical Significance

Intermolecular interactions[36] are ubiquitous in nature. The term generally refers to the attractive or repulsive force that act between molecules. Intermolecular interactions are important because they affect the physical and chemical properties of a substance: for instance, the strength of intermolecular interaction may determine whether a compound is solid, liquid or gas at a given temperature, or whether a chemical reaction can happen between certain species.

Intermolecular interactions are responsible for many interesting phenomena in systems involving excited molecules. For example, the color of a solute can be different when dissolved in different solvents. Such a phenomenon is known as solvatochromism[37], and it can be explained by the environmental effect of solvents that causes the change in the solute's excitation energy. Some small inorganic anions such as halides can form stable excited states in aqueous solution while they would simply ionize in gas phase. This effect can be measured by the charge-transfer-to-solvent (CTTS) spectrum[38–47]. Intermolecular interactions can be substantially different in ground and excited states: some molecules that are unbound or only weakly bound in the ground state can form stable complexes once excited. All these facts motivate us to develop theoretical tools that facilitate study of intermolecular interactions in excited states.

1.3.2 Physical Components of Interaction

Based on different physical origins, the source of intermolecular interactions can be qualitatively categorized into the following components:

- **Permanent Electrostatics**
  Permanent electrostatics accounts for the Coulomb interaction between molecules without adapting their charge distribution to their surroundings. At well-separated distances, the permanent electrostatics can be approximated by a multipole expansion. The asymptotic distance dependence of permanent electrostatics is determined by the leading term of the expansion, e.g. it decays as R^{-1} if the leading term is monopole-monopole, R^{-2} for monopole-dipole, R^{-3} for dipole-dipole, R^{-4} for dipole-quadrupole, etc. The permanent electrostatics term can be either repulsive or attractive.

- **Pauli Repulsion**
  Pauli repulsion is a consequence of the Pauli principle, which states that Fermions such as electrons cannot occupy the same state. As a result, bringing two molecules very close to each other results in an unfavorable energy change, as electrons with the same spin may be forced to have similar spatial wavefunctions. The Pauli repulsion is a short-range effect and it decays exponentially with distance, as the overlap between the wavefunctions of two molecules vanishes when they are well-separated.

- **Polarization**
  The charge distribution of one molecule will relax due to the presence of the electric field produced by other molecules. This effect is called polarization or induced electrostatics, and always has a favorable contribution to the interaction energy. The long-range behavior of polarization also follows classical electrostatics. For example, the contribution from a dipole-induced dipole interaction would decay as R^{-6}.

- **Charge Transfer**
  Charge transfer refers to the phenomenon that a fraction of electron population can transfer between molecules when they interact. In the MO picture, it can be viewed as the shift of electron density from a donor orbital on one molecule to an acceptor orbital on the other molecule. Contrary to polarization, CT accounts for the *intermolecular* relaxation of the supersystem. Similar to Pauli repulsion, it also decays exponentially with intermolecular distance.

- **Dispersion**
  The dispersion is a purely non-classical effect which results from the interaction of instantaneous dipole moments. Capturing the dispersion requires proper description of

the dynamic motion of electrons, and thus dispersion is missing from methods without dynamical correlation such as the Hartree-Fock theory. Dispersion is always a favorable effect and decays as R^{-6} asymptotically. It can be the dominant binding force in systems without permanent multipoles (e.g. rare gas dimers or clusters).

- **Excimer Interaction**
  Molecules that weakly interact in the ground state may form a strongly bound complex called an excimer once excited[48]. There are two types of molecular interaction that contribute to formation of excimers: exciton resonance (ER) and charge resonance (CR). ER describes the interaction between two localized excited states, $A^*B \leftrightarrow AB^*$. While ER is often attributed to the interaction of two transition dipoles, the exact exchange and the overlap between localized states should also be taken into account at short distance. CR arises from the interaction between two charge-transfer configurations, $A^+B^- \leftrightarrow A^-B^+$, which is Coulombic in nature. Both ER and CR states can contribute to the final states through configuration mixing. The excimer interaction is often important when discussing intermolecular interactions in excited states.

1.3.3 Energy Decomposition Analysis

The strength of intermolecular interaction is often measured by the interaction energy, which, with a "supermolecular" approach, is defined as the difference between the energy of the supersystem and the sum of the energies of the constituent molecular fragment in isolation:

$$\Delta E_{\text{INT}} = E_{\text{super}} - \sum_{I}^{\text{frag}} E_I \tag{1.23}$$

The interaction energy alone does not provides a full picture of intermolecular interaction. It is often desirable to understand the mechanism behind the interaction, i.e. what roles does one of the aforementioned physical components play in a certain system? This is not an easy task as the mechanism can be different from case to case, depending on the molecular species and their arrangement into a complex. The energy decomposition analysis (EDA) is a tool designed for achieving better understanding of intermolecular interaction. It refers to a category of methods that decomposes the total interaction energy into terms corresponding to the physical components mentioned above. As such, the EDA serves as a way to bridge the gap between interaction energies obtained from *ab initio* calculations (eq. 1.23) and physical intuition, and it helps chemists assess the relative importance of each interaction component.

While the total interaction energy can be measured by experiments, the EDA components are not measurable quantities. Thus, there is no unique or "correct" EDA method. In practice, the development of EDA involves confirming the expected asymptotic behavior and validation on model systems where the interactions are well understood. Once confirmed to be reasonable, a proposed EDA can then be applied to other systems of interests.

Various EDA methods have been developed for studying interaction of ground state systems[49–70]. For molecules in excited states, an EDA for the interaction energy can be useful to explain the formation of exciplexes/excimers. The excitation energy is another quantity that is important and unique for excited systems. It is thus of interest to decompose the *shift in excitation energy*, which has many applications in understanding the effect of environment on molecular excitations.

1.4 Outline

This thesis presents some recent progress in excited state electronic structure theory, with a particular focus on molecular complexes or clusters. We first discuss some improvements to the computational methods for obtaining excited states. This is approached in two perspectives: in Chapter 2, we developed a variant of traditional method, which with efficient implementation, can handle much larger system without significant loss of accuracy. In Chapter 3, the goal of methodology development is to tackle certain systems that are not treated properly with traditional methods, and improve the accuracy on these systems. In the final two chapters, we present an EDA scheme for excited states that allows decomposition for both the interaction energy and shifts in excitation energies. A summary of the remaining chapters is as follows.

Chapter 2

Simulations of the $n = 2$ absorption spectra of $\mathrm{He_N}(\mathrm{N} = 70, 150, 231, 300)$ clusters are reported, with nuclear configurations sampled by path integral molecular dynamics. The electronic structure is treated by a new approach, ALMO-CIS+CT, which is a formulation of configuration interaction singles (CIS) based on absolutely-localized molecular orbitals (ALMOs). The method generalizes the previously reported ALMO-CIS model (*J. Chem. Theory Comput.* **11**, 5791 (2015)) to include spatially localized charge transfer (CT) effects. It is designed to recover large numbers of excited states in atomic and molecular clusters, such as the entire $n = 2$ Rydberg band in helium clusters. ALMO-CIS+CT is shown to recover most of the error caused by neglecting charge transfer in ALMO-CIS, and has comparable accuracy to standard CIS for helium clusters. For the $n = 2$ band, CT stabilizes states towards the blue edge by up to 0.5 eV. ALMO-CIS+CT retains the formal cubic scaling of ALMO-CIS with respect to system size. With improvements to the implementation over that originally reported for ALMO-CIS, ALMO-CIS+CT is able to treat helium clusters with hundreds of atoms using modest computing resources. A detailed simulation of the absorption spectra associated with the $2s$ and $2p$ bands of helium clusters up to 300 atoms is reported, using path integral molecular dynamics with a spherical boundary condition to generate atomic configurations at 3 K. The main features of experimentally reported fluorescence excitation spectra for helium clusters are reproduced. This work has been published in *The Journal of Chemical Physics*[71].

Chapter 3

It is well-known that simple theories of excited states such as configuration interaction singles (CIS) exhibit a systematic bias against charge transfer (CT) states. To address this issue in molecular complexes, we propose MR-ALMOCIS, a multi-reference formulation of CIS based on absolutely-localized molecular orbitals (ALMOs). The MR-ALMOCIS wavefunction is constructed as a superposition of ALMO-CIS [*J. Chem. Theory Comput.* **11**, 5791 (2015)] states computed from multiple references with distinct charge and spin constraints applied, and the weight (coefficient) of each ALMO-CIS state in such a superposition is determined by solving a non-orthogonal configuration interaction (NOCI) problem. We applied MR-ALMOCIS to several model systems: the He dimer cation (He_2^+), the water-Mg^{2+} complex, and a series of aromatic-tetracyanoethylene (Ar-TCNE) complexes, and several desirable features of this method were demonstrated: (i) for systems of strong multi-reference character, MR-ALMOCIS is able to produce correct excited-state structure and asymptotic behavior of excitation energies (e.g. correct degeneracy at long range); (ii) for conventional charge-transfer complexes, MR-ALMOCIS is able to produce multiple states of interest (both CT and non-CT) simultaneously, and it outperforms standard CIS for the excitation energies of CT states. This method can be a suitable model for studying the interplay of local excitations and CT states in photochemical processes involving molecular complexes.

Chapter 4

An energy decomposition analysis (EDA) scheme is developed for understanding the intermolecular interaction involving molecules in their excited states. The EDA utilizes absolutely localized molecular orbitals (ALMOs) to define intermediate states, and is compatible with excited state methods based on linear response theory such as configuration interaction singles (CIS) and time-dependent density functional theory (TDDFT). The shift in excitation energy when an excited molecule interacts with the environment is decomposed into frozen, polarization and charge transfer contributions, and the frozen term can be further separated into Pauli repulsion and electrostatics. These terms can be added to their counterparts obtained from the ground state EDA to form a decomposition of the total interaction energy. The EDA scheme is applied to study a variety of systems, including some model systems to demonstrate the correct behavior of all the proposed energy components, as well as more realistic systems such as hydrogen-bonding complexes (e.g. formamide-water, pyridine/pyrimidine-water) and halide (F^-, Cl^-)-water clusters that involve charge-transfer-to-solvent (CTTS) excitations. This work has been published in *The Journal of Chemical Physics*[72].

Chapter 5

We present an improved energy decomposition analysis (EDA) scheme for understanding intermolecular interactions in delocalized excited states, especially in excimers. In the EDA procedure, excited states are treated with linear response theory such as configuration interaction singles (CIS) or time-dependent density functional theory (TDDFT), and absolutely localized molecular orbitals (ALMOs) are used to define the intermediate (frozen, excitonic coupling, and polarized) states. The intermolecular interaction energy is thereby separated into frozen, excitonic splitting, polarization and charge transfer contributions. The excitonic splitting term describes the delocalization effect as two or more degenerate local excitations couple with each other, which is often an important binding force in excimers. A maximum overlap state-tracking procedure is introduced to connect the initial fragment excitations to the constrained intermediate states, and finally to the unconstrained delocalized states of the complex. The EDA scheme is applied to several excimer systems, including the He_2^* and Ne_2^* noble gas excimers, the doubly hydrogen-bonded 2-pyridone dimer, and the aromatic benzene and perylene excimers. We are able to gain some useful insights into the role each term is playing in the formation of these excimers, and the resulting method may also be useful for understanding a range of other complexes in excited states. This work has been published in *The Journal of Chemical Theory and Computation[73].*

Chapter 2

ALMO-CIS with CT correction

2.1 Introduction

Atomic and molecular clusters span the range between the gas phase and bulk limits, and they are useful for investigating fundamental differences between bulk and surface properties. Helium clusters are of particular interest: they are weakly interacting, superfluidic[74] and can be used as a spectroscopic medium[75, 76]. Experimentally, fluorescence spectra[77–79] provide a way to understand how the excited electronic states are modified when a helium atom is adjacent to the others. Typical spectra of helium clusters consist of sharp atomic lines accompanied by blue-shifted wings, and their relative intensities depend on the cluster sizes.

Even for helium, the simplest many-electron atom, theoretical study of the excited electronic states remains a challenge for large clusters. A method must balance accuracy against efficiency to be practically useful. Two of the simplest methods are time-dependent density functional theory (TDDFT)[9, 31–33] and configuration interaction singles (CIS)[9, 10]. TDDFT is more widely used, because in many cases where the dynamic electron correlation is important, it outperforms CIS in terms of accuracy. CIS often has quite large ($\sim 1\,\mathrm{eV}$) errors in excitation energies due to the neglect of dynamic electron correlation.

Nonetheless, CIS does not suffer from the incorrect asymptotic potential and self-interaction error of TDDFT. For this reason, for relative energies of Rydberg states in helium clusters, CIS is the method of choice. Moreover, CIS can be improved systematically by adding higher substitutions to the CI wavefunction[20]. Previous CIS calculations on small clusters involving up to 25 helium atoms shows that CIS is capable of elucidating the spectroscopy[80] and the post-excitation dynamics of helium clusters[81].

However, modern experiments mainly focus on helium clusters with hundreds to tens of thousands of atoms or even larger, which is beyond the normal capability of CIS due to its high order scaling with respect to system size: a conventional CIS calculation for all states scales as $O(M^6)$, with the number of (identical) atoms or molecules, M, in the cluster. When only a handful of the low-lying excited states are requested, the CIS eigen-equation can be solved iteratively using Davidson's method[12, 13], which reduces the scaling to $O(M^4)$ in the molecular orbital (MO) basis per state. In the atomic orbital (AO) basis, matrix element sparsity reduces the cost to as low as $O(M^2)$ per state (with a large prefactor) for the rate-determining matrix-vector contraction.

Unfortunately, to directly compare with the experimental spectra of large homogeneous clusters, we need a full description of the energy bands of He clusters. The number of states required then grows at least linearly with the number of atoms (for instance, the $n = 2$ band of a 1000-atom helium cluster requires a minimum of 4000 states), suggesting that iterative methods are not preferred. On the other hand, direct solution for all states is not feasible, as already discussed.

Great effort has gone into reducing the scaling of CIS and TDDFT methods. By exploiting certain types of spatial locality or sparsity in matrix representations, some linear scaling methods have been developed[82–84]. However, rigorous linear scaling is only achieved in substantially large systems, especially since the electronic density of excited states are often much more delocalized than that of the ground state (here we mainly focus on systems whose excitations cannot be localized in a certain region, such as homogeneous clusters). For this reason, these linear scaling methods are not fully applicable for systems consisting of hundreds of atoms, and different approximations seem to be desirable for these cases. A common feature of the above mentioned methods is that the localized molecular orbitals (LMOs) are obtained by localizing canonical molecular orbitals (CMOs) into confined physical regions. This "top-down" scheme is often found to be inefficient due to the difficulty of localizing virtual orbitals when system size increases[85, 86].

Fragment-based methods, by contrast, follow a "bottom-up" scheme, where LMOs are obtained directly from subsystem calculations without computing the CMOs first. One example is the fragment molecular orbital (FMO) method developed by Kitaura and coworkers[87]. The idea is to divide the system into fragments and perform ab initio calculations of fragments and their dimers. The method was extended to excited state calculations by employing the multilayer FMO method, in which the region of chemical interest is treated with CIS[88], CIS(D)[89] or TDDFT[90], while the environment is kept at the HF/DFT level. Wu *et al.* proposed a linear scaling TDDFT method through the use of fragment LMOs which are orthogonal but still well localized[91]. More recently, Herbert and co-workers implemented the Frenkel-Davydov exciton model to study the excited states of aggregates, where an excitonic state is constructed from direct products of fragment configuration state function basis[92–94].

Another bottom-up method, which is fully self-consistent, is the approach based on absolutely localized molecular orbitals (ALMOs), which were first introduced to speed up SCF calculations on weakly interacting systems[95–99]. ALMOs are defined by the constraint that the MO coefficient matrix is block diagonal between fragments. This type of constrained SCF procedure is commonly referred to as SCF for molecular interactions (SCF-MI). Subsequently ALMOs from SCF-MI have also proven useful in the development of energy decomposition analysis (EDA) methods[68–70, 100, 101].

In a previous publication, we reported ALMO-CIS[102], an ALMO-based excited state method, and its application to helium clusters. The ALMO-CIS method scales as only $O(M^3)$ for the evaluation of $O(M)$ states. Two factors contribute to the reduction of the scaling: (a) The molecular orbitals (MOs) are linear combination of only AOs centered on a certain fragment, which greatly reduces the cost of transforming the electron-repulsion integrals (ERIs) from AOs to MOs; (b) the locality of MOs allows us to associate a single substitution to fragments, and the CIS equation can be truncated in a physically meaningful manner. In the ALMO-CIS model, only intrafragment single excitations are considered, and this reduces the matrix dimension from $O(M^2)$ to $O(M)$ in the CIS equation and thereby reduces the scaling of the method.

A TDDFT(MI) method has also been recently proposed by Liu and Herbert[103], which shares the same spirit with ALMO-CIS. The major difference is that TDDFT(MI) computes several lowest excited states for the monomers first, then evaluates the supersystem excited states as the linear combination of these local states, using the Davidson algorithm. This current implementation is optimized for systems such as solvated chromophores, where a relatively small number of the excited states are of interest. With some modification of the algorithm, TDDFT(MI) could also be extended to obtain the full spectrum of molecular clusters.

Both ALMO-CIS and TDDFT(MI) restrict the excitations to be intrafragment, which means the charge transfer (CT) effect is neglected. For helium clusters, the ALMO-CIS method is found to have $\sim 0.5\,\mathrm{eV}$ overestimation for excitation energies at the blue end of the $n = 2$ band, when measured against standard CIS. It also has systematic error for predicting the spectrum profiles[102]. For many other systems with stronger interaction than helium, we expect the error will be more pronounced. All these considerations motivate us to seek a way to correct the ALMO-CIS model by at least partially reintroducing the neglected charge transfer class of excitations.

In this work, we add back the charge transfer effect by using a real-space distance cutoff. The model presented here is called ALMO-CIS+CT. The remainder of the paper is organized as follows: in the Theory section, we introduce the generalization of the ALMO-CIS model to ALMO-CIS+CT, and a Davidson-like variational method that is used to solve the eigenvalue problem. Next, we discuss some optimization we have done for the fast implementation of the ALMO-CIS+CT model. The accuracy and timing results are presented in the Result section. Finally, we apply ALMO-CIS+CT for the study of helium clusters, and the resulting spectra are compared with the experimental data. A brief description of a more rigorous simulation for the cluster geometries with path integral molecular dynamics can also be found in the Application section.

2.2 Theory

2.2.1 Notation

The following notation is used throughout the paper. i, j, k, l: occupied MO indices; a, b: virtual MO indices; p, q, r: generic MO indices. χ_μ: atomic orbitals; χ_P, χ_Q: auxiliary basis functions. The ALMOs are denoted by ψ, and ϕ is used for projected virtual orbitals. Fragments are indicated by I,J or F_I, F_J. Unless otherwise specified, two orbital indices connected as $\underbracket{pq}$ or $\overbracket{pq}$ belong to two near-neighbor fragments.

We use capital letters to indicate quantities that scale with system size, and lowercase letters for quantities that do not: O, V, N: total number of occupied/virtual/atomic orbitals in the system; o, v, n: the average numbers of occupied/virtual/atomic orbitals per fragment; $\tilde{o}$, $\tilde{v}$, $\tilde{n}$: the average numbers of occupied/virtual/atomic orbitals within the near-neighbor fragments defined by the distance criterion. For a system with identical fragments, the number of fragments M can be used to denote the size of the system.

We use standard tensor notation to work with nonorthogonal functions[104]. A covariant function is denoted by a subscript and a contravariant function is denoted by a superscript. The Einstein summation convention is also employed, where an index that occurs once covariant and once contravariant implies a sum.

2.2.2 ALMO-CIS and its generalization to include charge transfer

Let us begin by defining the ALMOs. The atoms in an atomic cluster (or molecules in a molecular cluster) are divided into non-overlapping subsets that are referred to as fragments. The atom centered AOs can thus be partitioned based on the fragments they belong to. In the ALMO formalism, each molecular orbital (MO) on a given fragment is a superposition of AOs centered on the same fragment exclusively, and this results in a block-diagonal MO coefficient matrix.

$$|\psi_p\rangle = \sum_{\mu \in F_I} |\chi_\mu\rangle C_p^\mu, \qquad p \in F_I \tag{2.1}$$

The MO coefficients can be solved within the framework of self-consistent field theory with the constraint that the MO coefficient matrix should be fragment-blocked. The resulting ALMOs are orthogonal within a fragment but are nonorthogonal between fragments.

In the previous ALMO-CIS publication[102], we have derived the generalized CIS equations that apply to nonorthogonal molecular orbitals:

$$A_{ia,jb} t^{jb} = \omega_{CIS} S_{ab} S_{ij} t^{jb} \tag{2.2}$$

Here $\omega_{CIS} = E - E_{HF}$ is the excitation energy, and t^{jb} are the CIS amplitudes. The overlap metric S appears because of the interfragment nonorthogonality of ALMOs. We have chosen known matrix elements to be covariant, and the unknown amplitudes to be contravariant.

The (restricted) CIS Hamiltonian can be constructed from the Fock matrices f, overlap metric S and the two-electron integrals:

$$A_{ia,jb} = f_{ab}S_{ij} - f_{ij}S_{ab} + 2\left(\psi_i\phi_a \mid \phi_b\psi_j\right) - \left(\psi_i\psi_j \mid \phi_a\phi_b\right) \tag{2.3}$$

All virtual orbitals above are technically "projected virtuals", which are defined by projecting out the occupied space from the ALMO virtuals to ensure that occupieds and virtuals are orthogonal (the unprojected ALMO virtuals on a fragment are non-orthogonal to both occupied and virtual ALMOs on other fragments).

$$\begin{aligned} |\phi_a\rangle &= N_a\big(|\psi_a\rangle - \hat{P}_{occ}|\psi_a\rangle\big) \\ &= N_a(|\psi_a\rangle - |\psi_k\rangle(S^{-1})^{kl}\langle\psi_l|\psi_a\rangle \\ &= N_a\big(|\psi_a\rangle - |\psi_k\rangle\langle\psi^k|\psi_a\rangle\big) \end{aligned} \tag{2.4}$$

where N_a is the normalization constant and $|\psi^k\rangle = |\psi_l\rangle(S^{-1})^{lk}$ are the contravariant occupied orbitals.

In the ALMO-CIS model, the CIS matrices are truncated by including only "intra-fragment" single substitutions (i.e. those that promote an electron from an occupied level to a virtual level assigned to same fragment), which can be denoted as follows:

$$A_{\underbracket{ia},\underbracket{jb}}t^{\overbracket{jb}} = \omega_{CIS}\underbracket{S_{ab}S_{ij}}t^{\overbracket{jb}} = \omega_{CIS}G_{\underbracket{ia},\underbracket{jb}}t^{\overbracket{jb}} \tag{2.5}$$

G is the metric associated with the retained intra-fragment single substitutions. It is intuitive that the ALMO-CIS model is free of charge-transfer contributions. As shown in the appendix, this can also be proven, in the sense that fragment Mulliken populations are unchanged from the ground state in the ALMO-CIS model.

The ALMO-CIS equation, Eq. 2.5 can be generalized to include some charge transfer (CT) type single substitutions based on a selection of significant fragment pairs within which CT will be permitted. Specifically, we use a distance based cutoff (r_{cut}) to determine whether two fragments are to be considered as neighboring fragments. A significant fragment pair list can be created, comprising all pairs of fragments whose distances are smaller than r_{cut}. Pairs of a same fragment repeated twice are considered as zero distance pairs and thus are also included in the list.

As a result, when a single substitution has corresponding occupied and virtual orbitals that belong to a pair of fragments in the pair list, we will include it in the truncated matrices. In this way, the form of the working ALMO-CIS equation (eq. 2.5) remains the same, but the meaning of the contraction lines is generalized. In the ALMO-CIS model, a contraction line connects two indices that belong to a same fragment. Now, in the generalization that we will refer to as ALMO-CIS+CT, the two indices belong to a significant pair of fragments.

The cutoff distance is a user-defined parameter in the ALMO-CIS+CT model. At one extreme, in the limit of $r_{cut} \to 0$, the fragment pair list will only include the pairs that contain the same fragment twice, and ALMO-CIS+CT reduces to the original ALMO-CIS model.

At the other extreme, when a very large r_{cut} is chosen, all possible single substitutions are included, and the untruncated CIS equations (eq. 2.2) are recovered. For a weakly interacting system, such as a helium cluster, a cutoff that corresponds to including the first shell of neighboring atoms will be shown (in the Results section) to be sufficient to recover most of the error caused by neglecting CT in ALMO-CIS.

The oscillator strength of an excited state κ is defined as:

$$f_\kappa = \frac{2}{3}\omega_\kappa |\langle\psi_0|\hat{\mu}|\psi_\kappa\rangle|^2 \tag{2.6}$$

Within the ALMO-CIS+CT theory, the dipole matrix elements can be calculated as:

$$\begin{aligned}\langle\psi_0|\hat{\mu}|\psi_\kappa\rangle &= \sum_{\substack{F_I,F_A\in\\ \text{FrgPairList}}} \sum_{\substack{i\in F_I\\ a\in F_A}} t_\kappa^{\overbracket{ia}} \langle \underbracket{\psi_i|\hat{\mu}|\phi_a}\rangle \\ &= \sum_{\substack{F_I,F_A\in\\ \text{FrgPairList}}} \sum_{\substack{i\in F_I\\ a\in F_A}} t_\kappa^{\overbracket{ia}} \underbracket{c^{\dagger\mu}_{\cdot i}\,\mu_{\mu\nu}c^{\nu}_{\cdot a}}\end{aligned} \tag{2.7}$$

These matrix elements will be used later in evaluating the absorption spectrum of helium clusters.

2.2.3 Davidson-like variational method

The eigenvalue problem of eq. 2.5 can be solved by a full diagonalization. In the ALMO-CIS model, this $O(M^3)$ scaling step was found to be a minor step because of its relatively small prefactor. However, when CT substitutions are included, the computational effort will increase by the cube of the factor by which the number of single substitutions has increased. For the nearest-neighbor cutoff, applied to a medium-sized helium cluster, the ALMO-CIS+CT matrix size is roughly five to six times larger than for ALMO-CIS, and as a result the diagonalization timing is about 200 times longer. Full diagonalization is still feasible, but becomes a dominant step. Thus, we propose a one-step Davidson-like variational method to alleviate this problem.

The eigenvalue problem of eq. 2.5 is now expressed in terms of the intra-fragment (local) subspace (denoted by l) and the charge transfer subspace (denoted by c). In the matrix elements below, each index l or c corresponds to an occupied-virtual pair ia. The dimensions of the two subspaces are denoted by N_l and N_c, respectively. Likewise, the trailing state index in the amplitudes, $\mathbf{t}$, and eigenvalues, $\boldsymbol{\omega}$, can be associated with a state that is primarily local (l) or primarily CT (c).

$$\begin{bmatrix} A_{ll} & A_{lc} \\ A_{cl} & A_{cc} \end{bmatrix} \begin{bmatrix} t_{ll} & t_{lc} \\ t_{cl} & t_{cc} \end{bmatrix} = \begin{bmatrix} G_{ll} & G_{lc} \\ G_{cl} & G_{cc} \end{bmatrix} \begin{bmatrix} t_{ll} & t_{lc} \\ t_{cl} & t_{cc} \end{bmatrix} \begin{bmatrix} \boldsymbol{\omega}_l & 0 \\ 0 & \boldsymbol{\omega}_c \end{bmatrix} \tag{2.8}$$

Solving the above full-size eigenvalue problem can be avoided since we are wanting to obtain corrected roots only for the ALMO-CIS states (ie. only for the l block). We will show that the dimension of the eigenvalue problem to be solved for those corrected roots can be reduced to just $2 \times N_l$ by using a one-step Davidson-like method.

We first solve an eigenvalue problem in the local subspace, i.e., solve $A_{ll}t_{ll}^{(0)} = G_{ll}t_{ll}^{(0)}\boldsymbol{\omega}_l^{(0)}$ and obtain $t_{ll}^{(0)}$ and $\boldsymbol{\omega}_l^{(0)}$ as the uncorrected eigenvectors and eigenvalues. They are simply the ALMO-CIS eigenvectors and eigenvalues. Next, we form a transformation to a projected CT basis $\tilde{C}$ that is constructed to be orthogonal to the local subspace.

$$\tilde{C} = \begin{bmatrix} -t_{ll}^{(0)}t_{ll}^{(0)\dagger}G_{lc} \\ I \end{bmatrix} = \begin{bmatrix} C \\ I \end{bmatrix} \tag{2.9}$$

where I is the $N_c \times N_c$ identity matrix. With the projected CT basis, the eigenvalue problem becomes:

$$\begin{bmatrix} \tilde{A}_{ll} & \tilde{A}_{lc} \\ \tilde{A}_{cl} & \tilde{A}_{cc} \end{bmatrix} \begin{bmatrix} t_{ll} & t_{lc} \\ t_{cl} & t_{cc} \end{bmatrix} = \begin{bmatrix} \tilde{G}_{ll} & 0 \\ 0 & \tilde{G}_{cc} \end{bmatrix} \begin{bmatrix} t_{ll} & t_{lc} \\ t_{cl} & t_{cc} \end{bmatrix} \begin{bmatrix} \boldsymbol{\omega}_l & 0 \\ 0 & \boldsymbol{\omega}_c \end{bmatrix} \tag{2.10}$$

where the projected blocks are given by

$$\begin{aligned} &\tilde{A}_{ll} = A_{ll}; \qquad \tilde{A}_{lc} = A_{ll}C + A_{lc}; \\ &\tilde{A}_{cc} = \tilde{C}^\dagger A \tilde{C} = C^\dagger A_{ll} C + A_{cl}C + C^\dagger A_{lc} + A_{cc} \\ &\tilde{G}_{ll} = G_{ll}; \qquad \tilde{G}_{lc} = 0 \\ &\tilde{G}_{cc} = \tilde{C}^\dagger S \tilde{C} = C^\dagger G_{ll} C + G_{cl}C + C^\dagger G_{lc} + G_{cc} \end{aligned} \tag{2.11}$$

Similar to the Davidson method, we compute the correction vectors by

$$\boldsymbol{\delta} = (\tilde{A}_{cc} - \bar{\omega}\tilde{G}_{cc})^{-1} r \tag{2.12}$$

where $r = \tilde{A}_{cl}t_{ll}^{(0)}$ are the residue vectors of the uncorrected ALMO-CIS excited states. The scalar, $\bar{\omega}$, involved in the preconditioner is a parameter which should be chosen based on the states that one is interested in, and it should be close to the target eigenvalues. For example, in our study of helium clusters, we target the $n = 2$ manifold of states, and thus $\bar{\omega}$ is approximated by the average of the uncorrected $n = 2$ eigenenergies $\boldsymbol{\omega}_l^{(0)}$, so that separate preconditioning for each state can be avoided. It is thus required to solve an N_c-dimensional linear equation once to apply the preconditioner in Eq. 2.12. One can avoid this third-order scaling step by considering keeping only diagonal elements of the preconditioner. However, the cost of solving the linear equation has a quite small prefactor. In fact, for the helium cluster systems we have studied, it is actually not the dominant step in the whole Davidson-like procedure. Therefore, the reduction of computational cost from a simplified preconditioner does not seem to be worthwhile, considering the diminished accuracy that comes with it. Detailed timings for the Davidson-like method and tests showing the accuracy of different types of preconditioners are reported in the Results section.

We can now attach the correction vectors to the local subspace, and form A and G in a $2 \times N_l$ subspace spanned by $t_{ll}^{(0)}$ and $\boldsymbol{\delta}$. The result is a generalized eigenvalue problem of dimension $2 \times N_l$, which is typically 3 times smaller than that of the full ALMO-CIS+CT model. The eigenstates and eigenvalues corresponding to intrafragment excited states (now corrected for CT) can be obtained by taking the lowest N_l eigen-solutions. This approach is like a one-step Davidson method, and the resulting excitation energies are variational upper bounds to the exact ALMO-CIS+CT eigenvalues that come from solving Eq. 2.5 exactly.

2.3 Efficient Implementation and Scaling

An efficient implementation of the ALMO-CIS+CT model has been completed within a development version of Q-Chem quantum chemistry program package[105, 106]. With CT states included, the size of the truncated Hamiltonian and overlap metric will increase by a factor that depends on the cutoff distance one chooses. However, the storage for these matrices still scales as $O(M^2)$. For the size of systems we have studied, this fact allows the matrices to be explicitly calculated and stored in memory, and Eq. 2.5 to be solved as a final step without memory issues. Thus, the algorithms for building the Hamiltonian reported in the implementation of the ALMO-CIS method[102] can be inherited without major modification. Nevertheless, some aspects of the two-electron integral evaluation have been reformulated to further increase computational efficiency. The following subsections will discuss these aspects in detail.

2.3.1 Strategy for Two-Electron Integral Evaluation

The two electron integrals appearing in Eq. 2.3, including a Coulomb-like term $(\underbracket{\psi_i\phi_a} \mid \underbracket{\psi_j\phi_b})$ and an exchange-like term $(\overbracket{\psi_i\psi_j \mid \phi_a}\phi_b)$, are expanded in terms of unprojected ALMO contributions and projection corrections:

$$\begin{aligned}
(\underbracket{\psi_i\phi_a} \mid \underbracket{\psi_j\phi_b}) = \mathcal{N}_a\mathcal{N}_b\{\, & (\underbracket{\psi_i\psi_a} \mid \underbracket{\psi_j\psi_b}) \\
& - 2\,(\underbracket{\psi_i\psi_a} \mid \overbracket{\psi_j\psi_k)\,\left(\psi^k \mid \psi_b\right.})\\
& + (\underbracket{\psi_i\psi_k \mid \overbracket{\psi_j\psi_l)\,\left(\psi^k \mid \psi_a\right.}}\!\!\overbracket{\,)\,\left(\psi^l \mid \psi_b\right.})\}\\
J = \mathcal{N}_a\mathcal{N}_b(& J1 - 2\cdot J23 + J4)
\end{aligned} \tag{2.13}$$

$$\begin{aligned}
(\overbracket{\psi_i\underbracket{\psi_j \mid \phi_a}}\underbracket{\phi_b}) = \mathcal{N}_a\mathcal{N}_b\{ & (\overbracket{\psi_i\underbracket{\psi_j \mid \psi_a}}\underbracket{\psi_b}) \\
& - 2\,(\overbracket{\psi_i\underbracket{\psi_j \mid \psi_a}}\underbracket{\psi_k)\,\left(\psi^k \mid \psi_b\right.}) \\
& + (\overbracket{\psi_i\underbracket{\psi_j \mid \psi_k\psi_l)\,\left(\psi^k \mid \psi_a\right.}}\underbracket{)\,\left(\psi^l \mid \psi_b\right.})\}\\
K = \mathcal{N}_a\mathcal{N}_b(& K1 - 2\cdot K23 + K4)
\end{aligned} \tag{2.14}$$

The expansion is exactly the same as in the ALMO-CIS model, except here two indices connected by a contraction line belong to two neighboring fragments, rather than being restricted to the same fragment. The terms involving four-center two-electron integrals with three or four occupied indices ($J23$, $J4$, $K23$ and $K4$) are corrections to the four-center unprojected integrals and are essential for quantitative accuracy.

We evaluate the correction terms using the resolution of the identity (RI) approximation[107–109], where the four-center two-electron integrals are decomposed into three-center integrals, $(\psi_i\psi_j \mid \chi_P)$ and $(\psi_i\psi_a \mid \chi_P)$, as well as the inverse of the Coulomb metric in the auxiliary basis $\left(\chi^P \mid \chi^Q\right)$:

$$
\begin{aligned}
J23 &= (\psi_i\psi_a|\psi_j\psi_k)\left(\psi^k \mid \psi_b\right) = (\psi_i\psi_a|\chi_P)\left(\chi^P \mid \chi^Q\right)(\chi_Q|\phi_j\psi_k)\left(\psi^k \mid \psi_b\right)\\
J4 &= (\psi_i\psi_k \mid \psi_j\psi_l)\left(\psi^k|\psi_a\right)\left(\psi^l|\psi_b\right) = \left(\psi^k\middle|\psi_a\right)(\psi_i\psi_k|\chi_P)\left(\chi^P \mid \chi^Q\right)(\chi_Q|\phi_j\psi_l)\left(\psi^l \mid \psi_b\right)\\
K23 &= (\psi_i\psi_j|\psi_a\psi_k)\left(\psi^k|\psi_b\right) = \Big(\psi_i\psi_j \mid \chi_P\Big)\left(\chi^P \mid \chi^Q\right)(\chi_Q \mid \psi_a\psi_k)\left(\psi^k|\psi_b\right)\\
K4 &= (\psi_i\psi_j \mid \psi_k\psi_l)\left(\psi^k|\psi_a\right)\left(\psi^l|\psi_b\right) = \Big(\psi_i\psi_j \mid \chi_P\Big)\left(\chi^P \mid \chi^Q\right)(\chi_Q \mid \psi_k\psi_l)\left(\psi^k|\psi_a\right)\left(\psi^l|\psi_b\right)
\end{aligned}
$$

The number of three-center two-electron integrals needed does not depend on whether charge transfer states are included, since for both cases, the indices of three-center two-electron integrals should run over all the occupied and virtual orbitals, as well as all the auxiliary basis. Thus, the algorithm used in the ALMO-CIS model, namely, the "digestor" that transforms the three-center integrals from AO basis to MO basis can be adopted without any change. On the other hand, the following contraction steps need to be modified to account for the fact that more occupied-virtual pairs are now included.

The leading terms, $J1$ and $K1$, can be evaluated using the schemes that were presented previously[102]. However, this may not be optimal and we have developed new algorithms that will improve the computational efficiency. In the next two subsections, we shall compare different possible schemes in building the $J1$ and $K1$ terms, and discuss the necessity of adopting a better scheme when charge transfer states are present.

2.3.2 ALMO Coulomb Integral Evaluation

Let us begin by analyzing the formal scaling of the previous ALMO-CIS implementation. The most computationally significant step was to form the half-transformed integrals $J_{ia}^{\mu\nu} = (\chi_\mu\chi_\nu \mid \psi_i\psi_a)$, which were computed as a contraction of the AO integrals $(\mu\nu \mid \lambda\sigma)$ with the pseudo densities $P_{ia}^{\lambda\sigma} = c_i^\lambda c_a^{\dagger\sigma}$. When the excitations are restricted to be intrafragment, the only AO integrals we need to compute are those with μ and ν on the same fragment, and λ and σ on a different fragment. Their number is only $NNnn$. Because of the block structure of the density, each integral will contract with ov densities, so the scaling for the contraction step is $NNnnov$.

With CT excitations between near-neighbors included, the AO integrals that are needed will grow to become $NN\tilde{n}\tilde{n}$, and the scaling will become $NN\tilde{n}\tilde{n}ov$. Therefore, although the scaling of the contraction remains quadratic with system size, the prefactor is $(\tilde{n}/n)^2$

times larger, which is roughly a factor of 25 for the case of helium clusters. Based on the ALMO-CIS timing results[102], this suggests that building the Coulomb integrals is likely to become a dominant step if no improvements are made. Thus, we have to look into other ways of doing the Coulomb-type contraction.

One possibility is to replace the contraction of AO integrals with densities by two quarter transforms to the ALMO representation. The AO integrals $(\mu\underbracket{\nu}|\,\lambda\underbracket{\sigma})$ are first transformed with ALMO coefficients C_i^{λ} to form $(\mu\underbracket{\nu}|\,i\underbracket{\sigma})$, and then the quarter transformed integrals are contracted with C_a^{σ} to form the half-transformed integrals $(\mu\underbracket{\nu}|\,i\underbracket{a})$. In this scheme, with CT substitutions, the scaling for the first and second quarter transforms are given by $NN\tilde{n}\tilde{n}o$ and $NN\tilde{n}\tilde{o}v$, respectively. Thus, by replacing the contraction with densities by two quarter transformations, the computational cost can be reduced by a factor of v, the average number of virtual orbitals on a single fragment. This is a significant improvement.

However, there is a price to be paid for the two quarter transformation approach. When contracting with the densities, an AO integral can be used multiple times because of the permutation symmetries. For example, $(\mu\underbracket{\nu}|\,\lambda\underbracket{\sigma})$ is not only contracted with $P^{\overbracket{\lambda\sigma}}_{\underbracket{ia}}$, but also used as $(\lambda\underbracket{\sigma}|\,\mu\underbracket{\nu})$ to contract with $P^{\overbracket{\mu\nu}}_{\underbracket{jb}}$. As a result, only about one-eighth of the integrals are computed since there are eight such permutations. On the other hand, if the AO integrals are quarter-transformed with MO coefficients, the permutation between the bra side and ket side cannot be readily used. To understand this, one can look at the batching scheme shown in Algorithm 1. The second quarter transform is performed after the first quarter transformation of a particular batch of bra values is done, and only a batch of quarter transformed integrals $(\mu\underbracket{\nu}|\,i\underbracket{\sigma})$ is held in memory at one time. The first quarter transform must be completed by running over all pairs of ket indexes, so it is not possible to only loop over the ket batches with indices smaller or larger than the bra batch index. If one want to use "upper triangle" or "lower triangle" loop structures for batches, the second half transform has to be moved outside the loop over bra batches. This, however, will demand all the quarter transformed integrals to be stored in memory, which is impractical for large systems, since the number of quarter transformed integrals is $NN\tilde{n}\tilde{o}$. Therefore, in our current implementation, we employ the quarter transform at the price of computing twice as many AO integrals as we have before. The sacrifice is worthwhile if the cost of computing AO integrals is insignificant compared to the contraction steps, which is true for the Coulomb like integrals, as shown in the timing result in the Result section.

2.3.3 ALMO Exchange Integral Evaluation

The exchange term in ALMO-CIS was evaluated from half-transformed integrals $K^{\overbracket{ia}}_{\underbracket{\mu\lambda}} = (\chi_\mu\underbracket{\overbracket{\psi_i\,|\chi_\lambda}\psi_a})$, which were formed by contracting the AO integrals with pseudo-density matrices $P^{\overbracket{\nu\sigma}}_{\underbracket{ia}} = c_i^{\nu} c_a^{\dagger\sigma}$. If this density contraction scheme is used for the case with charge transfer excitations, the scaling is predicted to be $(NN)\tilde{n}\tilde{n}ov$. Here the parentheses on NN comes

Algorithm 1: (Half) integral transfrom for the Coulomb term, $J_{\mu\underbracket{\nu}i\underbracket{a}} = (\mu\underbracket{\nu}|\, i\underbracket{a})$

```
for $bra\ batches$ do
    for $ket\ batches$ do
        for $\mu\nu \in batch$ do
            for $\lambda\sigma \in batch$ do
                $\lambda \to F_I$, $\sigma \to F_J$
                for $i = 1, O_{F_I}$ do
                    $(\mu\underbracket{\nu}|\, i\underbracket{\sigma}) \mathrel{+}= (\mu\underbracket{\nu}|\, \lambda\underbracket{\sigma})\, C^{I\lambda}_{Ii}$
                for $j = 1, O_{F_J}$ do
                    $(\mu\underbracket{\nu}|\, j\underbracket{\lambda}) \mathrel{+}= (\mu\underbracket{\nu}|\, \lambda\underbracket{\sigma})\, C^{J\sigma}_{Jj}$
    for $\mu\nu \in batch$ do
        for $ia \in$ FrgPairList do
            $\sigma \to F_A$
            for $a = 1, V_{F_A}$ do
                $(\mu\underbracket{\nu}|\, i\underbracket{a}) \mathrel{+}= (\mu\underbracket{\nu}|\, i\underbracket{\sigma})\, C^{A\sigma}_{Aa}$
Use the permutation between $\mu\nu$ to scatter $\mu\nu$ from shellpair form to matrix form.
```

Table 2.1: Comparison of the density contraction and the MO Coefficient contraction schemes for the half-transform to build J1

scheme	step	scaling	computing AO-ERI twice
a	$(\mu\underbracket{\nu}|\, \lambda\underbracket{\sigma})\, P^{\overbracket{\lambda}\sigma}_{\underbracket{i}a} \to (\mu\underbracket{\nu}|\, i\underbracket{a})$	$NN\tilde{n}\tilde{n}ov$	No
b	$(\mu\underbracket{\nu}|\, \lambda\underbracket{\sigma})\, C^{\lambda}_{i} \to (\mu\underbracket{\nu}|\, i\underbracket{\sigma})$ $(\mu\underbracket{\nu}|\, i\underbracket{\sigma})\, C^{\sigma}_{a} \to (\mu\underbracket{\nu}|\, i\underbracket{a})$	$NN\tilde{n}\tilde{n}o$ $NN\tilde{n}\tilde{o}v$	Yes

from the sparsity of $\mu\nu$ pairs, namely, the number of significant shell pairs grows linearly with system size, and thus we expect the overall scaling to form the half transformed integrals is $O(M)$ for large enough systems (a limit that is not easily reached with the very diffuse basis sets needed for excited states).

It is promising to consider using the two quarter transformations for the exchange term as well. There will be further improvement in both scaling and memory concerns if we transform the two occupied indexes first. The first step transforms $(\overbracket{\mu\underbracket{\nu\,|\lambda}}\sigma)$ with C^{μ}_{i} to form $(\overbracket{i\underbracket{\nu\,|\lambda}}\sigma)$, with compute effort that scales as $(NN)\tilde{n}\tilde{n}o$. Next, the quarter transformed integrals are transformed with C^{ν}_{j} to form $(\overbracket{i\underbracket{j}}\underbracket{\,|\lambda\sigma})$, at a cost that scales as $(NN)\tilde{n}\tilde{o}o$. Therefore, the MO contraction scheme will reduce the cost of digesting the integrals by a factor of v as it did in the Coulomb case, and the memory storage for the half transformed integrals is also reduced by a factor of v/o.

However, we have not implemented that scheme yet. For the helium cluster systems we focus on, detailed timings show that, unlike the Coulomb-like terms, the cost of computing the AO integrals is comparable to the cost of the transformation steps. Thus the advantage in contraction is likely to be offset by computing twice as many integrals. For the special case of helium clusters, we implemented an alternative scheme for digestion, where the two occupied indices are transformed at the same time. The idea of this method is similar as using density matrices, one can view it as contracting with a density matrix built by occupied orbitals $P_{i\underbracket{j}}^{\mu\overbracket{\nu}} = c_i^{\mu} c_j^{\nu\dagger}$. Details of this scheme are shown in Algorithm 2.

Table 2.2 compares different aspects of the three schemes mentioned above. It is noteworthy that our current approach scales as $(NN)\tilde{n}\tilde{n}oo$. For the helium clusters, there is only one occupied orbital per fragment, i.e. $o = 1$. Therefore we actually achieve the same scaling as MO coefficient transformation scheme(which scales as $(NN)\tilde{n}\tilde{n}o$), without the disadvantage of doubling the cost of computing AO integrals. When the cost for digestion step is dominant, which is likely to happen for systems with larger fragments, successive quarter transformation scheme will be preferable.

We have also implemented some optimizations with respect to the screening of integrals. The previous scheme for making the "mini-list" (significant quartet of AO basis shells) is summarized in Algorithm 3. The screening is based on the Schwarz inequality $|\,(\mu\nu \mid \lambda\sigma)\,| \leq (\mu\nu \mid \mu\nu)^{\frac{1}{2}}\,(\lambda\sigma \mid \lambda\sigma)^{\frac{1}{2}}$. This screening step appears to be trivial, since all quantities needed in the algorithm can be pre-made, computations inside the loops are only a few multiplications and conditional evaluations. However, this is a quartic scaling step because of the loops over bra and ket shell pairs, and, for large systems, it actually dominates the evaluation of exchange integrals in the previous ALMO-CIS implementation. This is the reason that the overall scaling of computing exchange integrals was found to be 2.88, while it was supposed to be linear with system size.

The current scheme for mini-list selection is described in Algorithm 4. We preselect fragment pairs based on the maximum value of occupied four center integrals $(ij \mid ij)$ on a given pair. This allows us to have a selection before entering the loop of ket shell pairs. In this way, the scaling of the algorithm can be reduced to cubic, if the number of fragment pairs that has $(ij \mid ij)$ bigger than thresh is linear with system size.

Algorithm 2: (Half) integral transform for the Exchange term, $K_{\mu\nu ij} = (\mu\nu|ij)$

```
for bra batches do
    for ket batches do
        for $\mu\nu \in$ batch do
            for $\lambda\sigma \in$ batch do
                $\mu \to F_I$, $\nu \to F_J$, $\lambda \to F_K$, $\sigma \to F_L$,
                if $F_I, F_K \in$ FrgPairList and $F_J, F_L \in$ FrgPairList then
                    for $k = 1, O_{F_K}$ do
                        for $l = 1, O_{F_L}$ do
                            $(\mu\nu|kl) \mathrel{+}= (\mu\nu|\lambda\sigma)\, C^{K\lambda}_{Kk} C^{L\sigma}_{Ll}$
                    for $i = 1, O_{F_I}$ do
                        for $j = 1, O_{F_J}$ do
                            $(\lambda\sigma|ij) \mathrel{+}= (\mu\nu|\lambda\sigma)\, C^{I\mu}_{Ii} C^{L\nu}_{Jj}$
                if $F_I, F_L \in$ FrgPairList and $F_J, F_K \in$ FrgPairList then
                    for $k = 1, O_{F_K}$ do
                        for $l = 1, O_{F_L}$ do
                            $(\mu\nu|lk) \mathrel{+}= (\mu\nu|\lambda\sigma)\, C^{K\lambda}_{Kk} C^{L\sigma}_{Ll}$
                    for $i = 1, O_{F_I}$ do
                        for $j = 1, O_{F_J}$ do
                            $(\lambda\sigma|ji) \mathrel{+}= (\mu\nu|\lambda\sigma)\, C^{I\mu}_{Ii} C^{L\nu}_{Jj}$
$K_{\mu\nu ij} = K_{\mu\nu ij} + K_{\nu\mu ji}$
```

Table 2.2: Comparison of different schemes for the half-transform to build K1

scheme	step	scaling	computing AO-ERI twice
a	$(\mu\nu|\lambda\sigma)\, P^{\nu\sigma}_{ia} \to (\mu i|\lambda a)$	$(NN)\tilde{n}\tilde{n}ov$	No
b	$(\mu\nu|\lambda\sigma)\, C^{\mu}_{i} \to (i\nu|\lambda\sigma)$ $(i\nu|\lambda\sigma)\, C^{\nu}_{j} \to (ij|\lambda\sigma)$	$(NN)\tilde{n}\tilde{n}o$ $(NN)\tilde{n}\tilde{o}o$	Yes
c	$(\mu\nu|\lambda\sigma)\, C^{\mu}_{i} C^{\nu}_{j} \to (ij|\lambda\sigma)$	$(NN)\tilde{n}\tilde{n}oo$	No

Algorithm 3: previous scheme for mini-list selection in building K1

```
for bra shell pairs $(IShl, JShl)$ do
    $IShl \rightarrow F_I$; $JShl \rightarrow F_J$;
    for ket shell pairs $(KShl, LShl)$ do
        $KShl \rightarrow F_K$; $LShl \rightarrow F_L$;
        if $F_I, F_K \in$ FrgPairList and $F_J, F_L \in$ FrgPairList
        or $F_I, F_L \in$ FrgPairList and $F_J, F_K \in$ FrgPairList then
            $I_1$: max $(\mu\nu \mid \mu\nu)^{\frac{1}{2}}$, $\mu\nu \in$ bra shell pairs
            $I_2$: max $(\lambda\sigma \mid \lambda\sigma)^{\frac{1}{2}}$, $\lambda\sigma \in$ ket shell pairs
            if $F_I, F_K \in$ FrgPairList and $F_J, F_L \in$ FrgPairList then
                $P_{max}$: $\max(|P_{ia}^{\mu\lambda}|, |P_{ia}^{\nu\sigma}|)$
            if $F_I, F_L \in$ FrgPairList and $F_J, F_K \in$ FrgPairList then
                $P_{max}$: $\max(|P_{ia}^{\mu\sigma}|, |P_{ia}^{\nu\lambda}|)$
            if $I_1 I_2 P_{max} >$ thresh then
                add $IShl, JShl, KShl, LShl$ to mini-list.
```

Algorithm 4: current scheme for mini-list selection in building K1

```
for bra shell pairs $(IShl, JShl)$ do
    $IShl \rightarrow F_I$; $JShl \rightarrow F_J$
    if $\max(ij \mid ij) <$ thresh$(i \in F_I, j \in F_J)$ then
        continue
    for ket shell pairs $(KShl, LShl)$ do
        $KShl \rightarrow F_K$; $LShl \rightarrow F_L$;
        if $F_I, F_K \in$ FrgPairList and $F_J, F_L \in$ FrgPairList
        or $F_I, F_L \in$ FrgPairList and $F_J, F_K \in$ FrgPairList then
            add $IShl, JShl, KShl, LShl$ to mini-list.
```

Note: The algorithm presented here is a simplified version of our actual implementation. In practice, considering the permutation between bra and ket side, we also need to select F_K, F_L based on $\max(kl \mid kl)$, and find F_I, F_J that connect with F_K, F_L using FrgPairList. This leads to a more complicated algorithm although it does not affect the scaling.

2.4 Assessment of the ALMO-CIS+CT implementation

2.4.1 Accuracy

We first study the accuracy of the ALMO-CIS+CT model with different choices of r_{cut}, in the hope that a relatively small r_{cut} can yield satisfactory accuracy, so that this model can be practically useful. Our test system is a small He_{25} cluster that has been studied with both standard CIS and ALMO-CIS[102]. In this and all the following calculations for helium clusters, each helium atom will be treated as a fragment. Figure 2.1 shows the excitation energies of the first 100 states (which is the $n = 2$ manifold) when r_{cut} is chosen to be $6, 7, 8, 10\, a_0$, along with the results obtained by standard CIS and ALMO-CIS. In this test, the RI approximation and the Davidson-like method are not applied, so that any error purely comes from the truncation of matrices in Eq. 2.5 (the error due to the use of ALMOs instead of CMOs is negligible in the case of helium clusters). The basis we use here is a modified 6-311(2+)G basis, which has 11 functions per helium atom. Thus in the absence of truncation, there will be 6250 single substitutions in total. By contrast, ALMO-CIS retains only the 250 intrafragment excitations. The choices of $r_{cut} = 6, 7, 8, 10\, a_0$ lead to the number of retained excitations being 330, 730, 1030 and 1490, respectively. From Fig. 2.1, we find for $r_{cut} = 8, 10\, a_0$, the excitation energies are almost identical to those obtained in standard CIS. We know that ALMO-CIS is least accurate at the high-energy edge of each band because these are the states with stronger CT character (some insights are provided in Sec V.D.). For example, compared to standard CIS, ALMO-CIS exhibits errors of $\sim 0.5\,\text{eV}$ at the blue end of the $n = 2$ band. This error has been reduced to less than $0.02\,\text{eV}$ in the ALMO-CIS+CT model, when $r_{cut} = 8\, a_0$.

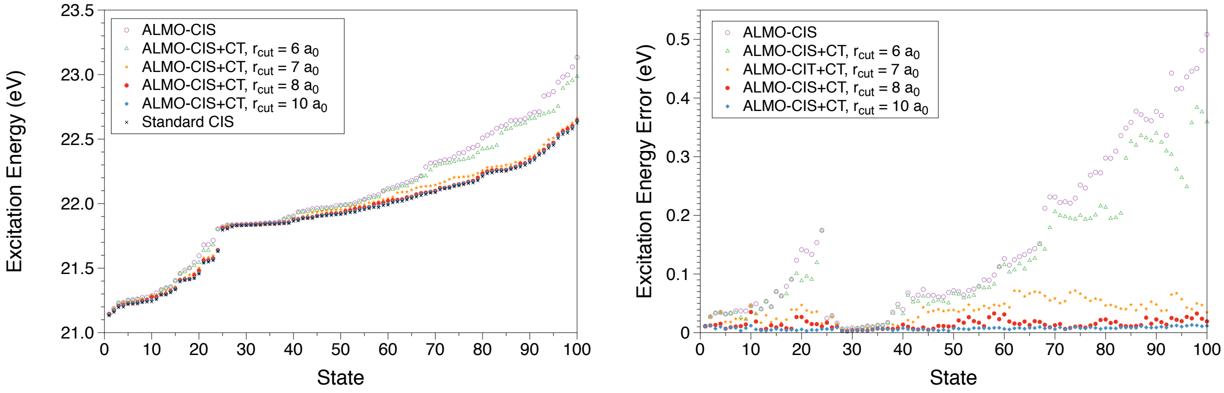

(a) (b)

Figure 2.1: (a) $n = 2$ manifold excitation energies for He_{25}, evaluated by CIS, ALMO-CIS and ALMO-CIS+CT with $r_{cut} = 6, 7, 8, 10\, a_0$. States 1-25 are of $2s$ character, and states 26-100 are of $2p$ character. (b) The absolute errors of excitation energies for ALMO-CIS and ALMO-CIS+CT model compared with standard CIS.

Figure 2.2 compares the spectrum of He_{25} calculated by standard CIS, ALMO-CIS and ALMO-CIS+CT with $r_{cut} = 8\, a_0$. We use the same He_{25} geometries that were used for the spectrum computed by CIS and ALMO-CIS, which come from 100 randomized clusters that are optimized subsequently at the MP2/6-311G level of theory[80]. It has been found that ALMO-CIS tends to give an overall more broadened spectrum, with the intensity at the low-energy edge (corresponding to surface states) being underestimated, and that at the

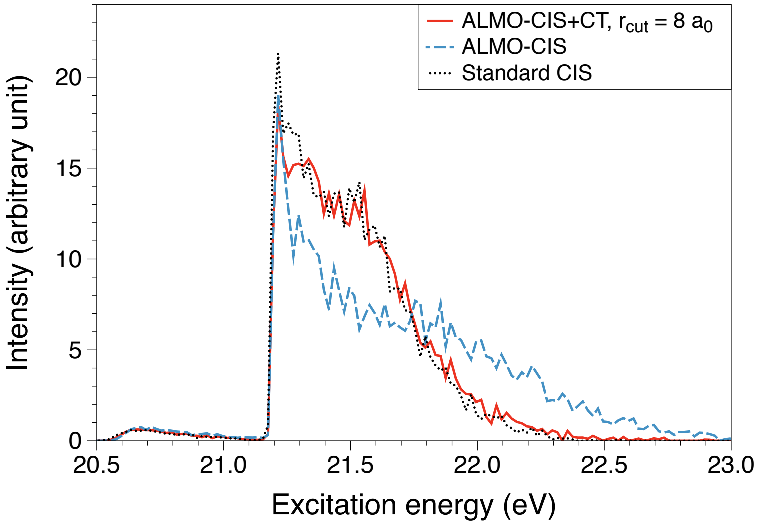

Figure 2.2: Absorption spectrum of He_{25} cluster at the ALMO-CIS, ALMO-CIS+CT ($r_{cut} = 8\,a_0$) and standard CIS level of theory. All spectrum profiles are shifted to the low-energy end by 0.625 eV to match the atomic peak of the experimental spectrum.

high-energy edge (corresponding to bulk states) being overestimated. Encouragingly, when a cutoff distance of $8\,a_0$ is employed, these errors are almost eliminated from the ALMO-CIS+CT spectrum.

Next we want to demonstrate the accuracy of the Davidson-like variational method for the excitation energies of the same He_{25} cluster. In Figure 2.3, we compare the ALMO-CIS and ALMO-CIS+CT results with and without the Davidson-like method ($r_{cut} = 8\,a_0$). Two different preconditioners were examined, the full preconditioner P_{full} and the diagonal preconditioner P_{diag}.

$$
\begin{aligned}
P_{full} &= (\tilde{A}_{cc} - \bar{\omega}\tilde{G}_{cc})^{-1} \\
P_{diag} &= (\mathrm{diag}(\tilde{A}_{cc} - \bar{\omega}\tilde{G}_{cc}))^{-1}
\end{aligned}
\tag{2.15}
$$

We find with the full preconditioner, the Davidson-like variational method causes nearly no additional error, since the data points of P_{full} almost overlap with those by solving Eq. 2.5 directly. When the diagonal preconditioner, P_{diag}, is utilized, only about 75% of the ALMO-CIS model error can be eliminated. These facts suggest that the matrices $\tilde{A}_{cc}$ and $\tilde{G}_{cc}$ are dense, most likely because there is already a truncation in Eq. 2.5.

At this moment, we conclude that $r_{cut} = 8\,a_0$ and a full preconditioner offer a good balance between accuracy and efficiency, and they will be used for all the calculations in the rest of the paper. Assuming that the structures of helium clusters more or less resemble that of the bulk system: an atom has 6 nearest neighbors[110] and the interatomic distance is 3.6 Å[111], the r_{cut} we have here will include the first shell of nearby atoms. This means that for the finite size clusters studied in this work, the matrix size of ALMO-CIS+CT will be no more than seven times (which is the bulk limit) of that in ALMO-CIS.

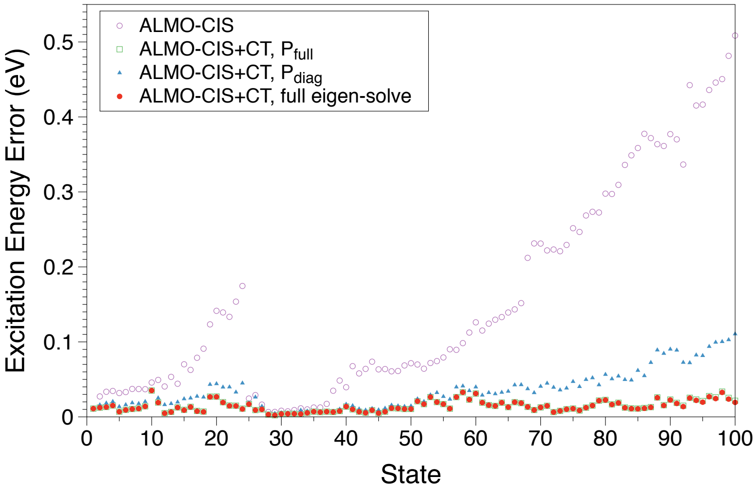

Figure 2.3: Errors of the excitation energies for He_{25} using ALMO-CIS, ALMO-CIS+CT solved exactly, and ALMO-CIS+CT solved by the Davidson-like method, with P_{full} and P_{diag} as the preconditioners. $r_{cut} = 8\,a_0$ for all ALMO-CIS+CT calculations

2.4.2 Timings

Two issues related to the efficiency of our models are of particular interest: the scaling versus system size, and the increase of computational effort when charge transfer is included. To address these two problems, we report timing results using helium clusters ranging from 44 to 377 regularly spaced atoms (4 Å) with both ALMO-CIS and ALMO-CIS+CT ($r_{cut} = 8\,a_0$) models. All calculations are performed with a single core on an AMD Opteron 6376 processor, using the same customized 6-311(2+)G basis as the previous subsection.

The relative costs of the major computational steps of ALMO-CIS and ALMO-CIS+CT are summarized in Figure 2.4. The slopes of the fitted lines show the scaling of each step. Overall, both methods have sub-cubic scaling, as we expected. It is noteworthy that forming the RI integrals, which is the most expensive step in ALMO-CIS, is exactly the same in ALMO-CIS+CT. The unchanged timing of this step is the main reason that the total cost of ALMO-CIS+CT is about only four times as large as that of ALMO-CIS, even though the matrix dimension is $5-6$ times larger.

Detailed timing of forming the Coulomb-like and exchange-like integrals are tested with He_{129} and He_{251} clusters, and the results are presented in Table 2.3 and Table 2.4. For the Coulomb-like integrals, the relatively expensive cost of contraction steps (especially the first quarter transform) supports our argument that it is worthwhile to apply the successive MO transform scheme at the cost of computing AO integrals twice. We note that for building AO

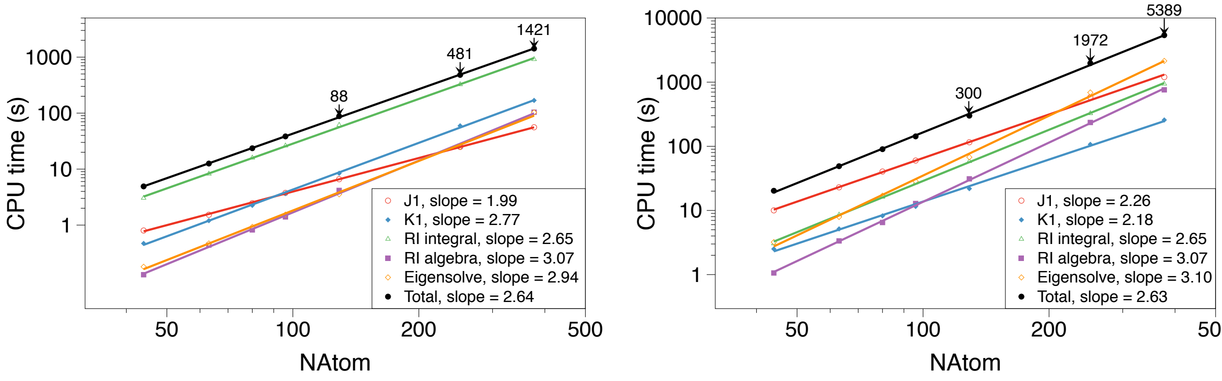

(a) ALMO-CIS

(b) ALMO-CIS+CT

Figure 2.4: CPU timing data for ALMO-CIS (a) and ALMO-CIS+CT with $r_{cut} = 8\,a_0$ (b). The y axis is in logarithm scale of the CPU time.

Table 2.3: CPU time (s) for significant steps in the construction of J1 integrals.

Method	System	NState	AO integrals	$(\underbracket{\mu\nu}\,|\,\underbracket{\lambda\sigma})\,C_i^\lambda \to (\underbracket{\mu\nu}\,|\,\underbracket{i\sigma})$	$(\underbracket{\mu\nu}\,|\,\underbracket{i\sigma})\,C_a^\sigma \to (\underbracket{\mu\nu}\,|\,\underbracket{ia})$	Total
ALMO-CIS	He_{129}	1290	3.75	2.31	0.17	6.60
	He_{251}	2510	14.24	8.66	0.64	24.89
ALMO-CIS+CT	He_{129}	6570	59.62	43.46	4.01	114.56
	He_{251}	14870	298.20	219.72	20.99	577.48

integrals in J1, an incompletely optimized new integral library is used. We expect roughly a four times speed-up of the AO integral computation in the future based on the performance of the old library. Also, we do not list the timing for mini-list selection as we do for the exchange-like integrals because the selection can be done at the shell-pair level, and it is a trivial step as it scales $O(M^2)$.

On the other hand, even with the optimizations described above, mini-list selection still takes about half of the time in forming the exchange integrals for ALMO-CIS+CT, and dominates in ALMO-CIS calculations where forming integrals and contractions are very cheap. The observed scaling of forming $K1$ is 2.77 for ALMO-CIS and 2.18 for ALMO-CIS+CT, instead of linear as is asymptotically possible. When charge transfer is included, we expect a $(\tilde{n}/n)^2$ times growth of computational effort in contraction steps and forming AO integrals. Based on the ratio of number of states in ALMO-CIS+CT and ALMO-CIS, $(\tilde{n}/n)^2$ is estimated to be 25 and 35 for He_{129} and He_{251}, respectively, and the observed growth in timing does not exceed these ratios.

To demonstrate the computational savings from the Davidson-like variational method, we also report the timing of the full eigen-solve for He_{129} and He_{251} in Table 2.5. It can be seen that although the Davidson-like method does not change the cubic scaling, it is about

Table 2.4: CPU time (s) for significant steps in the construction of K1 integrals.

Method	System	NState	Mini-list	AO integrals	$(\mu\nu\|\lambda\sigma)\,C_i^{\mu}C_j^{\nu} \rightarrow (ij\|\lambda\sigma)$	Total
ALMO-CIS	He_{129}	1290	7.81	0.26	0.34	9.48
	He_{251}	2510	56.06	0.64	0.92	61.48
ALMO-CIS+CT	He_{129}	6570	9.51	3.26	6.81	23.69
	He_{251}	14870	63.9	9.90	17.93	110.79

Table 2.5: CPU time (s) for the Davidson-like method and the full eigen-solve on He_{129} and He_{251} clusters.

System	Davidson-like method	Preconditioning	Full eigen-solve
He_{129}	71.68	11.81	490.18
He_{251}	696.87	131.48	6409.57

7 times faster than solving the full eigenvalue problem for these two systems. In addition, the preconditioning step (with full preconditioner) takes only about 1/6 of the total cost of the Davidson-like method. Thus, a simplified preconditioner such as P_{diag} would not significantly reduce the computational cost. Considering the additional error it entails, the diagonal preconditioner is not recommended at this time.

2.5 Calculating the absorption spectra of helium clusters

2.5.1 PIMD simulation

In the previous ALMO-CIS work[102], we generated an ensemble of cluster geometries starting from randomized initial geometries which were then optimized using either MP2 theory, or a classical force field for bigger clusters where MP2 is inaccessible. The resulting geometries are a myriad of local minima because of the shallow potential wells and many degrees of freedom. However, with a standard Lennard-Jones potential ($\epsilon_0 = 10.7\,\mathrm{K}, r_0 = 2.9\,\mathrm{\AA}$), we find the resulting clusters are too dense. To qualitatively match the known facts about helium clusters (for example, the average interatomic distance in bulk helium is 3.6 Å), we were forced to use a modified Lennard-Jones potential with a much shallower potential well ($\epsilon_0 = 0.05\,\mathrm{K}$) and a larger equilibrium distance ($r_0 = 3.6\,\mathrm{\AA}$). Of course the origin of the failure of the standard classical force field is due to neglecting the nuclear zero point motion, which is critical for helium atoms.

Feynman's path integral theory[112] treats nuclei quantum mechanically by mapping each quantum nucleus onto a classical system comprising several fictitious particles connected by springs ("ring-polymers"). This provides an ideal computational technique for the simulation of helium clusters, and there have been various successful applications of path integral Monte Carlo (PIMC)[113] and path integral molecular dynamics (PIMD)[114, 115] to helium systems. In this work, we employ PIMD to generate configurations of helium clusters of different sizes, which are then used to calculate the absorption spectrum.

The temperature of helium clusters in spectral measurements may be as low as 0.4 K, where the Bose statistics of ^{4}He atoms are significant. To properly account for the indistinguishability of identical particles, one has to sample the permutations as well. Ceperley *et al.* has employed a PIMC method that includes exchange to study helium clusters and found that superfluidity exists even in clusters as small as He_{64}[116]. For simplicity of implementation, our current PIMD formalism neglects the exchange between particles. Therefore our simulations are performed at 3 K, which is above the superfluid transition temperature.

In a PIMD formulation, the partition function is given by:

$$Z = \lim_{P\to\infty} \left(\frac{1}{2\pi\hbar}\right)^{NP} \int d^{NP}\mathbf{q} \int d^{NP}\mathbf{p}\, e^{-\beta_P H_P(\mathbf{p},\mathbf{q})} \tag{2.16}$$

where N is the number of distinguishable particles, P is the number of discretization points of quantum paths (or the number of chain particles in a ring polymer), $\beta_P = 1/Pk_BT$, and $H_P(\mathbf{p},\mathbf{q})$ is the ring polymer Hamiltonian:

$$\begin{aligned} H_P(\mathbf{p},\mathbf{q}) = &\sum_{i=1}^{N}\sum_{p=1}^{P}\left(\frac{\mathbf{p}_{i,p}^2}{2m_i} + \frac{1}{2}m_i\omega_P^2[\mathbf{q}_{i,p} - \mathbf{q}_{i,p+1}]^2\right) \\ &+ \sum_{p=1}^{P} V(\mathbf{q}_{1,p}, \mathbf{q}_{2,p}...\mathbf{q}_{N,p}) \end{aligned} \tag{2.17}$$

with $\omega_P = 1/\beta_P\hbar$. In our simulation, the interparticle potential V is described by the HFDHE2 potential[117]. The time evolution of PIMD follows the normal mode algorithm, and a white-noise Langevin thermostat[118] is employed (see Ref. 119 for further details). We find $P = 64$ and a time step of 2 fs yield converged results.

At finite temperature and zero pressure, the helium cluster will always evaporate in the long time limit. To avoid this issue, we confine the system within a sphere of radius R_c, so that an equilibrium between liquid and vapor can be established. The parameter R_c will affect the density of the system, and the available zero temperature density profile of helium clusters provide guidance for choosing R_c. A reasonable value of R_c should not be too small, so that the boundary will not have too much influence. It cannot be too big either, otherwise its role in preventing the system from evaporating is undermined. Unfortunately, we have no way to determine an optimal value of R_c. Therefore, for small clusters such as He_{70} and He_{150}, we perform simulations using several different R_c, and examine how the resulting spectra change. Then, to study the size-dependence of the spectra, we pick a reasonable density, and run the simulation with R_c determined based on the fixed density for clusters of different sizes.

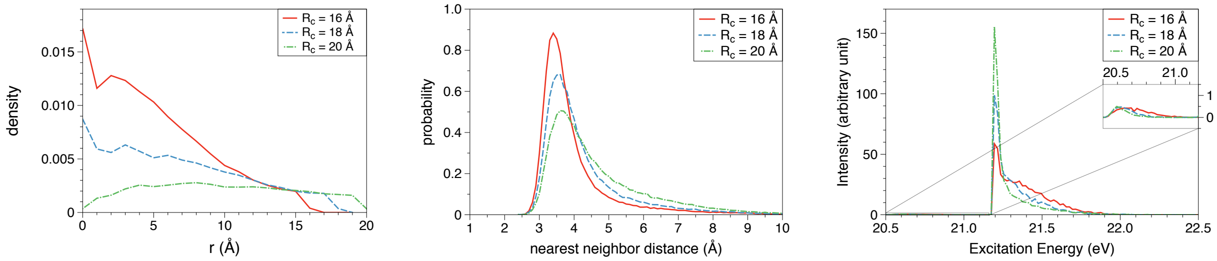

(a) He_{70}

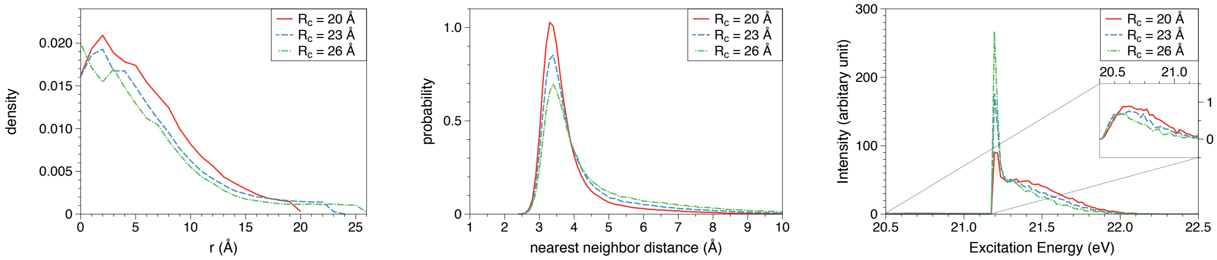

(b) He_{150}

Figure 2.5: Density profiles $\rho(r)$, nearest neighbor distributions $nn(r)$, and spectra of He_{70} (a) and He_{150} (b). The density profiles are plotted vs distance from the center of the confining sphere. Spectra are calculated by the ALMO-CIS+CT model, using 50 geometries from each PIMD simulation.

2.5.2 Dependence on R_c

Three different R_c are used for the simulation of He_{70} and He_{150}, respectively ($R_c = 16, 18, 20\,\text{Å}$ for He_{70}, $R_c = 20, 23, 26\,\text{Å}$ for He_{150}). The simulations are run with 200,000 warm-up steps (400 ps) to ensure that equilibrium is reached, and properties of interest and geometries used for spectral calculations are extracted from the following 400,000 time steps (800 ps). The resulting geometries can be characterized by density profiles $\rho(r)$ and nearest neighbor distribution $nn(r)$ (as defined in Ref.120), which are collected in Figure 2.5 along with the spectra. It is evident that the gas phase becomes increasingly dominant for larger R_c, which is reflected in a stronger atomic peak and smaller intensity at the high-energy edge of the spectra. This trend exists for both cluster sizes.

The kinetic energy (estimated by a virial estimator[121]), potential energy and total energy per helium atom are listed in Table 2.6. The positive total energies may imply that the system will eventually dissociate into the gas phase. To address this issue, we perform a simulation of He_{150} with $R_c = 24\,\text{Å}$, using only the repulsive part of the HFDHE2 potential. The system quickly develops into an evenly distributed gas, and the corresponding spectrum is more like a single atomic peak. Snapshots of He_{150} simulated with and without the attractive part of the potential (Figure 2.6) exhibit a clear difference. We conclude that liquid droplet structure exists at least for the time scale of our simulation. Meanwhile,

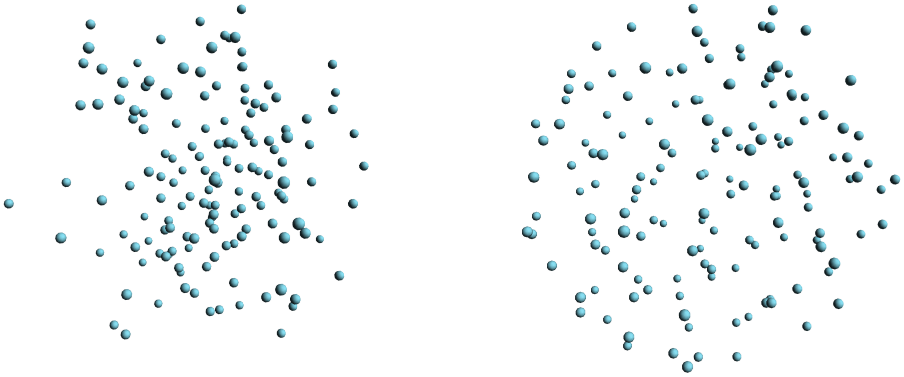

(a) droplet (b) gas

Figure 2.6: Snapshots of He_{150} cluster at $t = 400\,\mathrm{ps}$ when simulated with(a) and without(b) the attractive part of HFDHE2 potential. The resulting configurations are droplet and gas-like, respectively.

Barnett *et al.* has performed similar PIMD simulation of He_{70} with $R_c = 18.3\,\text{Å}$ and He_{150} with $R_c = 23.6\,\text{Å}$[114]. The energies and density profiles we obtained qualitatively agree with those available in their publication.

Table 2.6: The density, per-particle kinetic, potential and total energy of He_{70} and He_{150} clusters simulated by PIMD at 3 K with different choices of R_c.

System	R_c (Å)	$\rho\,(10^{-3}\,\text{Å}^{-3})$	T(K)	V(K)	E(K)
He_{70}	16	4.08	7.44	-5.94	1.50
	18	2.87	6.26	-3.67	2.59
	20	1.57	5.57	-2.32	3.25
He_{150}	20	4.48	8.50	-7.99	0.51
	23	2.94	7.61	-6.21	1.40
	26	2.04	6.85	-4.77	2.07

2.5.3 Size-dependence of the Spectra

To study the size-dependence of the spectra, we investigate four helium clusters of different sizes: He_{70}, He_{150}, He_{231} and He_{300}, and R_c is set to be $18, 23, 27, 29\,\text{Å}$, respectively, so that all four systems correspond to roughly the same density of $2.9 \times 10^{-3}\,\text{Å}^{-3}$. In Figure 2.7, we can see that the spectra of larger clusters have more intensity at the high-energy edge. This is reasonable since this "shoulder" next to the atomic peak results from the

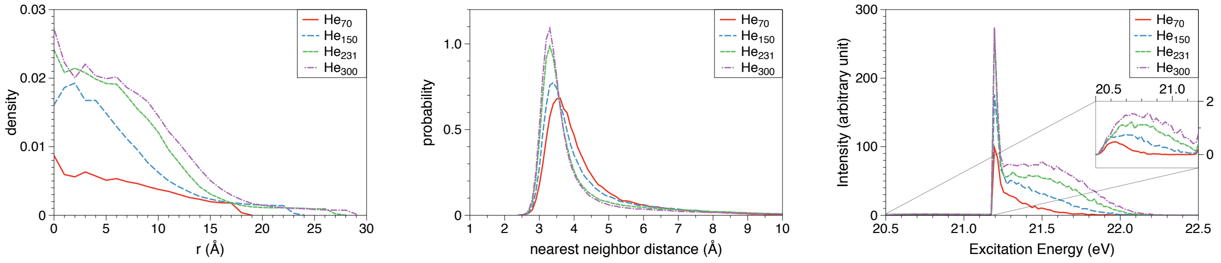

Figure 2.7: Density profiles $\rho(r)$, nearest neighbor distributions $nn(r)$ and spectra calculated by ALMO-CIS+CT for He_{70} ($R_c = 18\,\text{Å}$), He_{150}($R_c = 23\,\text{Å}$), He_{231}($R_c = 27\,\text{Å}$) and He_{300}($R_c = 29\,\text{Å}$) clusters

.

interaction between helium atoms, which should be stronger in larger clusters, as they have smaller interatomic spacing indicated by the density profile and nearest neighbor distribution. Moreover, the larger fraction of bulk atoms in the larger clusters also contributes to the broadening of the spectra.

2.5.4 Characterization of Excited States

A previous CIS study[80] of small helium clusters (He_7 and He_{25}) concluded that the higher-energy excited states mainly come from bulk-type excitations, while the lower-energy states come from surface excitations. To further understand this, we compare the droplet (Figure 2.6(a)) and gas (Figure 2.6(b)) spectra of He_{150} at $R_c = 16$ and $23\,\text{Å}$ (Figure 2.8(a)). The droplet typically has a gradually decreasing density from the core region to the surface, while the gas structure has a roughly uniform density in the whole sphere. For both R_c's, the droplet spectra are broader and more extended to the high-energy edge. This is because the droplet has a varying density, and its core density is higher than that of gas with the same R_c. It is also interesting to see, that when R_c decreases, the atomic peak diminishes in the droplet spectra, while for gas, we see a shift of the maximum peak instead.

The relation between the excitation energy and surface/bulk character of each state motivates us to find a mapping between these two. Previous state-by-state inspection[80] of the attachment and detachment density is unfeasible for large clusters and multiple configurations. Alternatively, here we introduce a scalar quantity $\bar{R}$ to represent the "average position" of the excitation relative to the center of the cluster. For state κ, $\bar{R}_\kappa$ is defined as:

$$\bar{R}_\kappa = \sum_{\substack{F_I, F_A \in \\ \text{FrgPairList}}} \sum_{\substack{i \in F_I \\ a \in F_A}} |\tilde{t}_\kappa^{\overset{\sqcap}{ia}}|^2 |(\vec{R}_I + \vec{R}_A)/2| \tag{2.18}$$

where $\vec{R}_I(\vec{R}_A)$ represents the position of $F_I(F_A)$ relative to the center of the cluster, and $\tilde{t} = G^{1/2}t$ so that $\tilde{t}$ is orthonormal between states.

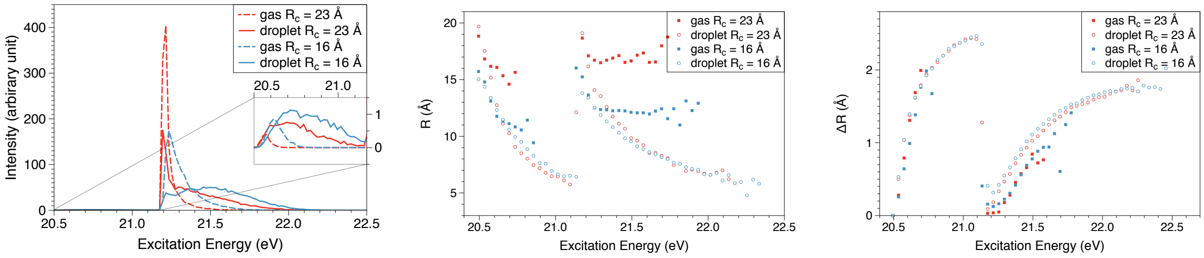

(a) (b) (c)

Figure 2.8: (a) The spectra of droplet and gas-like He_{150} at $R_c = 16\,\text{Å}$ and $23\,\text{Å}$. (b) $\bar{R}$ for the droplet and gas-like at $R_c = 16\,\text{Å}$ and $23\,\text{Å}$ as a function of excitation energy in the $n = 2$ band. (c) $\Delta\bar{R}$ evaluated in the same way. (both quantities are averaged over 50 geometries for each choice of R_c as in the spectrum calculations).

In the same spirit, we can define another quantity $\Delta\bar{R}$ as the weighted average of $|\bar{R}_I - \bar{R}_A|$, so that it serves as a metric of the charge transfer character of each state.

$$\Delta\bar{R}_\kappa = \sum_{\substack{F_I,F_A \in \\ \text{FrgPairList}}} \sum_{\substack{i\in F_I \\ a\in F_A}} |\tilde{t}_{\kappa}^{\overline{ia}}|^2 |\vec{R}_I - \vec{R}_A| \tag{2.19}$$

For each system, $\bar{R}$ and $\Delta\bar{R}$ can be plotted against the excitation energy. As shown in Figure 2.8(b) and (c), $\bar{R}$ and $\Delta\bar{R}$ are strongly correlated with the excitation energy in droplet systems. For both the $2s$ and the $2p$ band, the low-energy excitations correspond to larger $\bar{R}$ and smaller $\Delta\bar{R}$, which indicates that these excitations mainly come from the surface and have less CT character. As the excitation energy increases, bulk excitations with stronger CT character gain more importance, so we see the decrease of $\bar{R}$ and the increase of $\Delta\bar{R}$. For gas systems, it is still true that CT raises the excitation energy, so we can still see the patterns of $\Delta\bar{R}$. However, because the density distribution of gas systems is more uniform, the correlation between excitation energies and the location of the excitation site is much weaker. Thus, the curves of $\bar{R}$ are much flatter for the gas systems, except for the dips at the beginning of each band resulting from the boundary of the simulation sphere.

2.5.5 Comparison with Experiment

The size-dependence of helium droplet spectra have been studied by Möller and coworkers[77, 79]. In both Ref 77 and Ref 79, the authors observed that an increase in cluster size results in relative reduction of the atomic peak and relative enhancement of the hump at the high-energy edge. As was already demonstrated in Figure 2.7, this trend is reproduced by our computational simulation, and its origin is elucidated by the analysis of the surface/bulk character of each state introduced in Section 2.5.4. It is quite encouraging that the overall bandwidth seen experimentally is quite well reproduced by the simulation. This suggests that the destabilizing neighbor interactions responsible for the overall shift of the droplet excitations towards higher energy are quite well reproduced by the ALMO-CIS+CT treatment of the electronic structure.

However, it remains a challenge for the theoretically predicted spectra to quantitatively match the experimental results. There are several sources of difference between the simulations and the experiments. First is the fact that the experiments are technically fluorescence excitation spectra, while the calculations correspond to direct absorption. The fluorescence lifetime is on the order of 5-10 ns for "short-lived" excited states[79], and there is an additional longer-time fluorescence. The nuclear wavefunction is not an eigenstate of the electronically excited state, and the non-stationary wavepacket will certainly evolve, which is likely to affect the spectrum. This is an interesting topic for future investigation. A second issue is that the current PIMD simulation does not treat the Bose statistics of helium nuclei, and thus cannot account for the superfluidity that is present in the experiments. A third issue is that the current electronic structure model has limitations. Specifically, dynamic correlation is neglected in CIS, which results in an over-estimation of excitation energies. For this reason we have to shift all spectra to the left by 0.625 eV so that atomic peaks occur at the same position as in the experiments.

Uncertainty associated with experimental conditions adds further difficulty to a direct comparison of the calculated and observed spectra. The experiments usually prepare helium clusters by a nozzle expansion. The final cluster densities are sensitive to conditions such as nozzle temperature and pressure, and therefore the spectral profiles can vary in different experiments (for example when comparing cluster with similar sizes, spectra in Ref 77 have larger humps than those in Ref 79). As the actual density and other structure characters of helium clusters are hardly known, it is almost impossible to propose a simulation that can reproduce the condition at the experimental measurement. In addition, we believe that the systems are not at equilibrium in the experiment, while in the simulations we impose a confining boundary to obtain reasonably converged results for a system in liquid-vapor equilibrium.

Additionally, the current simulation model appears to miss some detailed features of the experimental spectra. One example is that as stated in Ref 79, a small hump associated with the $2s$ band exists at around 20.95 eV. Experimentally, the position of this maximum is nearly invariant as the cluster size changes, while our calculations show a feature that depends on both cluster size and density (for instance, see the magnified region in Figure 2.7(c)). It is hard to say whether this is due to the limitation in the electronic structure model or the difference between the simulation and experimental conditions. Despite the above mentioned deficiencies, we think that the PIMD simulation is a clear physical improvement over our previous excited state studies of helium clusters[80, 102]. With the charge transfer effect included via the new ALMO-CIS+CT approach, our methodology also improves the accuracy rendering it comparable to standard CIS, while the former is dramatically more efficient.

2.6 Conclusions

We have generalized the previously reported ALMO-CIS model to include charge transfer (CT) effects. Similar to ALMO-CIS, the ALMO-CIS+CT model presented in this work is a local variant of configuration interaction singles (CIS), and is formulated through the use of absolutely localized molecular orbitals (ALMOs). The difference is that unlike ALMO-CIS, where only intrafragment single excitations are involved, ALMO-CIS+CT retains interfragment excitations whose associated fragment pairs are within a cutoff distance. For helium clusters, the CT effects neglected by ALMO-CIS are mostly recovered when the first shell of neighboring atoms are included. When many excited states are requested (e.g. an entire band of states for a homogeneous cluster), ALMO-CIS+CT has a much lower computational cost (like ALMO-CIS) than standard CIS, while maintaining the same accuracy (in contrast to ALMO-CIS where systematic deviations are evident).

An efficient implementation has been described that minimizes the increase in computational cost versus ALMO-CIS. While the dimension of matrices in the eigenvalue problem is roughly six times larger than that in ALMO-CIS, the computational cost of building the Hamiltonian matrix does not grow enormously. This is partly because one of the most expensive steps (computing the three-center ERIs in the RI approximation) remains the same, and partly because the implementation of the Coulomb and Exchange integrals has been improved. Solving the eigenvalue problem can potentially be dominant in ALMO-CIS+CT calculations as its cost grows cubically with matrix size. This is remedied by employing a single step Davidson-like variational method without significant loss of accuracy. The overall scaling of ALMO-CIS+CT is third order with respect to system size, which is the same as ALMO-CIS. For medium sized helium clusters, the computational cost of ALMO-CIS+CT is about four times as large compared to that of ALMO-CIS. With our current implementation, systems with up to 377 helium atoms and 4147 atomic basis are reported in this work, using only standard workstation-level computer resources.

We apply ALMO-CIS+CT to study the $n = 2$ absorption spectra of helium clusters. To account for the quantum nature of helium nuclei, the geometries used for spectral calculations are generated from PIMD simulation (at 3 K to avoid the need to simulate the superfluid phase). This approach is not perfect due to the absence of indistinguishability between particles, but produces much more reasonable configurations than classical molecular dynamics. We report results on the size-dependence of the spectrum, as well as the effect of a confining boundary on the spectrum. We show that with reasonable choices of the confining radius, the system behaves as a liquid droplet in equilibrium with vapor on the timescale of the simulations. Broad features of the experimental spectrum, such as the bandwidth and size-dependence of the $2p$ band are qualitatively reproduced by the simulations. However, a number of finer details are not fully compatible between the simulations and reported experimental data.

As shown in the appendix, ALMO-CIS is CT-free because it preserves fragment populations in the Mulliken sense. Therefore differences between ALMO-CIS and ALMO-CIS+CT quantify the role of CT in cluster excited states. For He cluster absorption spectra, states towards the blue edge of the 2p band are stabilized by up to 0.5 eV by CT contributions while the red edge is virtually unaffected. The 2s states also show CT contributions that increase with excitation energy while they are negligible at the red edge. Even in a system whose electron affinity is as unfavorable as helium, CT effects provide significant excited state stabilization beyond a superposition of atomic excitations, and should not be neglected.

Interesting topics for future work include correcting the model for the neglected effect of dynamic correlations, either by incorporating higher substitutions into the wavefunction, or by extending the model to TDDFT. The applicability of this model to other molecular clusters with stronger interactions between monomers (for instance water clusters) is also potentially very interesting.

Chapter 3

Multireference ALMO-CIS

3.1 Introduction

While charge-transfer excited states play an important role in photochemical processes such as photosynthesis, [122] singlet fission, [123] etc., the accurate prediction of their excitation energies remains a challenge to theoretical methods. The two simple, computationally cheap, and widely-used methods, configuration interaction singles (CIS)[9, 10] and time-dependent density functional theory (TDDFT)[9, 31–33] have well-known difficulty in treating charge-transfer excited states. TDDFT suffers from the self-interaction error and a semi-local exchange-correlation functional is incapable of capturing the $1/R$ asymptotic behavior of CT excitation energies. [35] While range-separated hybrid functionals ameliorate this problem as they restore the correct long-range behavior, [124–126] the accuracy can be sensitive to the range-separation parameter ω, and that is probably why system-specific tuning of the ω value was suggested. [127, 128]

CIS, on the other hand, correctly recover the $1/R$ asymptotic behavior and can be improved systematically. However, CIS is highly biased against CT states, with CT excitation energies often overestimated by 1–2 eV. [129] The unfavorable CT energies can be explained by the fact that the molecular orbitals (MOs) are only optimized for the ground state (HF) solution, which may be far from being optimal for the CT states as the electrons are reorganized when charge transfer occurs. For example, in a donor(D)-acceptor(A) complex, the orbitals are optimized for the neutral DA configuration. When the D^+A^- excited state is formed, CIS provides no mechanism to contract or polarize the remaining electrons of donor or to expand and polarize the orbitals of the acceptor. Only the particle and hole orbitals are relaxed via CIS. Fundamentally similar problems affect more advanced excited state theories such as linear response or equation of motion coupled cluster methods. However, the presence of double or higher excitations allows the effect of orbital relaxation to be recovered indirectly. Subotnik and coworkers have shown that with incorporation of orbital relaxation effect, the perturbative orbital optimized (OO)-CIS [130, 131] and variationally orbital adapted CIS (VOA-CIS) [132] can achieve a more balanced description of CT and non-CT states. It should also be mentioned that Δ-SCF based on the maximum overlap method (MOM) [133] is also able to account for orbital relaxation effect and was reported to give satisfactory results for CT states. [134] However, this method can only compute one single excited state at a time and its success is limited to relatively simple cases where one dominant pair of donor-acceptor orbitals can be identified.

In cases where charge donor and acceptor can be clearly identified, the CT configuration is usually of higher energy than the closed-shell configuration, although their orders may be reversed along the reaction coordinate (e.g. the well-known LiF dissociation problem). This, however, does not hold for systems whose pre- and post-CT configurations are energetically degenerate or near-degenerate, such as a charged homogeneous dimer of organic molecules. For such a system, the $|D^+A\rangle$ and $|DA^+\rangle$ configurations naturally form two quasi-diabatic states, and the lowest two adiabatic states can be viewed as the in-phase and out-of-phase combinations of them. The multi-reference character renders the single-reference methods discussed above (CIS, TDDFT, or Δ-SCF) unsuitable for tackling the excited states of these systems, and one conventionally needs to resort to multi-reference electronic structure methods such as complete active space (CAS)SCF [25, 135] and perturbative corrections on top. [136, 137]

The non-orthogonal configuration interaction (NOCI) method [138–141] provides an alternative approach to addressing orbital relaxation and multi-reference problems. In NOCI, the wavefunction is constructed as a linear combination of multiple Hartree-Fock (HF) solutions (determinants) whose orbitals are independently relaxed. The orbital relaxation effect can be captured through the use of these pre-relaxed and thus non-orthogonal determinants, as opposed to including a full set of doubly promoted determinants — a common strategy in correlated wavefunction methods such as EOM-CCSD [21] or CIS(D) [20]. The NOCI method is able to obtain qualitatively correct results with much fewer determinants compared to conventional correlated wavefunction methods, and its extension to account for dynamical correlation through second-order Möller-Plesset perturbation theory (NOCI-MP2) further improves the accuracy. [142, 143]

One prerequisite for NOCI is to specify the basis determinants to be included. Besides using strategies such as SCF meta-dynamics, [144] MOM, [140] and spin-flip from high-spin restricted open-shell (RO) determinant [141] (plus further relaxation), another way to obtain well-defined basis state for molecular clusters is to use the SCF(MI) method. [99, 145] The SCF(MI) solutions are determinants constituted with absolutely localized molecular orbitals (ALMOs), [99] whose coefficients are constrained to be fragment block-diagonal such that each ALMO is only expanded by AOs from the same fragment. This scheme is well-suited for studying charge transfer states, as we can construct SCF(MI) basis states that resemble diabatic states. [146] For example, we can obtain two SCF(MI) solutions that represents the covalent ($\mathrm{D}\cdots\mathrm{A}$) and ionic ($\mathrm{D}^+\cdots\mathrm{A}^-$) configurations in a donor-acceptor system, and re-diagonalize through CI to obtain adiabatic wave-functions. Yost and Head-Gordon have implemented this ALMO-based NOCI scheme with the MP2 extension to study charged organic dimers and long C–C bonds in ethane derivatives. [143] Note that the idea of using quasi-diabatic states to construct the CI space was also employed in the multistate DFT

(MSDFT) method by Gao and co-workers, [147–150] as well as in the constrained DFT (CDFT)-CI formulated by Wu et al. [146, 151] for the evaluation of adiabatic state energies and electronic couplings between diabatic states.

The NOCI method typically solves for a few low lying states, e.g. we will obtain two adiabatic states that are linear combination of the D··A and $D^+ \cdots A^-$ configurations. To obtain higher CT and local excitation states, one can consider including excited states calculated from SCF(MI) references. Previously, we developed the ALMO-CIS method [102], which is the local version of CIS with SCF(MI) solution as the ground state. It is therefore possible to combine the idea of NOCI and ALMO-CIS: we can first perform ALMO-CIS calculations on different SCF(MI) references, and these ALMO-CIS states can form the CI space from which the final state can be obtained by solving a generalized secular equation. This excite-then-diagonalize scheme resembles the idea of perturb-then-diagonalize scheme in NOCI-MP2. We name this scheme as the MR-ALMOCIS method, as it is a generalized version of ALMO-CIS that utilizes multiple SCF(MI) references. In the rest of this paper, we will present a detailed formulation of this method and three application examples to demonstrate the desirable features as well as some potential limitations of this scheme.

3.2 Theory

3.2.1 Coupling of ALMO-CIS states from multiple references

Considering a donor-acceptor type of system, we first want to construct two reference wavefunctions $|\Psi_{DA}\rangle$ and $|\Psi_{D^+A^-}\rangle$ that describe DA and D^+A^- configurations, respectively. We use SCF(MI), a constrained SCF scheme based on absolutely localized molecular orbitals (ALMOs) [99] for this purpose: each reference state is obtained as the SCF(MI) solution with charge and spin on predefined fragments constrained (in the sense of Mulliken population[152]). For example, the first reference state for a ethylene-tetrafluoroethylene complex can be neutral C_2H_4 with neutral C_2F_4, both having $m_s = 0$. As C_2F_4 is more electronegative than C_2H_4, we would also consider charge transfer from C_2H_4 to C_2F_4 and include two other reference states: $C_2H_4^+(\uparrow)\cdot\cdot C_2F_4^-(\downarrow)$ and $C_2H_4^+(\downarrow)\cdot\cdot C_2F_4^-(\uparrow)$. The ALMO constraint forces the MO coefficient matrix to be block-diagonal across fragments. Note that the reference states constructed thereby use different sets of ALMOs as they are variationally optimized within different SCF(MI) calculations.

We can then construct singly excited states on top of each SCF(MI) reference wavefunction:

$$\begin{aligned} |\Psi^{\kappa}_{DA}\rangle &= \sum_{ia} t^{\kappa,ia}_{DA} |\Psi_{DA,ia}\rangle \\ |\Psi^{\kappa'}_{D^+A^-}\rangle &= \sum_{ia} t^{\kappa',ia}_{D^+A^-} |\Psi_{D^+A^-,ia}\rangle \end{aligned} \tag{3.1}$$

where i and a represent fragment-tagged occupied orbitals and projected virtuals, respectively, and κ (κ') is the index for excited states calculated from the neutral (ionic) reference.

In our previous work on ALMO-CIS, [102] we have derived generalized CIS equations that can work with nonorthogonal molecular orbitals (ALMOs in our case) and implemented an efficient algorithm to solve for the single-excitation amplitudes t^{ia}. One most important feature of this theory is that inter-fragment single excitations are excluded, i.e., amplitudes with occupied orbital i and virtual orbital a residing on different fragments are zero. As a result, the ALMO-CIS wavefunctions are ”CT-free” by nature (see the Appendix of Ref. 71).

Once ALMO-CIS solutions are obtained for each reference, we can select states of interest as basis states for an excitonic-type Hamiltonian. The global wavefunction of the system can be constructed as a linear combination of these selected ALMO-CIS excited states as well as the SCF(MI) reference states. The coefficients can then be obtained by solving a generalized eigenvalue problem $\mathbf{Hc} = E\mathbf{Sc}$, where the Hamiltonian matrix element and overlap between two ALMO-CIS basis states are defined as:

$$H_{\kappa\kappa'} = \langle \Psi^{\kappa'}_{D^+A^-} | \hat{H} | \Psi^{\kappa}_{DA} \rangle = \sum_{iajb} t^{\kappa',jb}_{D^+A^-} t^{\kappa,ia}_{DA} \langle \Psi_{D^+A^-,jb} | \hat{H} | \Psi_{DA,ia} \rangle \tag{3.2}$$

$$S_{\kappa\kappa'} = \langle \Psi^{\kappa'}_{D^+A^-} | \Psi^{\kappa}_{DA} \rangle = \sum_{iajb} t^{\kappa',jb}_{D^+A^-} t^{\kappa,ia}_{DA} \langle \Psi_{D^+A^-,jb} | \Psi_{DA,ia} \rangle \tag{3.3}$$

As ALMO-CIS solutions calculated from multiple reference states are included in this CI scheme, we call this method multi-reference (MR)-ALMOCIS.

To compute the matrix elements $\langle \Psi_{D^+A^-,jb} | \hat{H} | \Psi_{DA,ia} \rangle$ and $\langle \Psi_{D^+A^-,jb} | \Psi_{DA,ia} \rangle$, we first re-orthogonalize the occupied ALMOs within each singly-substituted determinant. Then, to tackle the non-orthogonality arising from the difference in ALMOs associated with each reference state, we can employ the generalized Slater-Condon rule as in previous NOCI works. [139, 153] However, summing over all pairs of singly-substituted determinants in two basis states is computational unfeasible. To reduce the computational cost, in our current implementation we perform a natural transition orbital (NTO) [154] analysis for each basis state, and then truncate the expansion of each ALMO-CIS basis state by including only a number of significant single transitions between occupied and virtual NTOs:

$$\begin{aligned} |\Psi^{\kappa}_{DA}\rangle &\approx \sum_{m=1}^{M} s^{\kappa,m}_{DA} |\Psi_{DA,\tilde{i}\tilde{a}}\rangle \\ |\Psi^{\kappa'}_{D^+A^-}\rangle &\approx \sum_{m=1}^{M} s^{\kappa',m}_{D^+A^-} |\Psi_{D^+A^-,\tilde{i}\tilde{a}}\rangle \end{aligned} \tag{3.4}$$

where M is the number of significant NTO pairs, s^m is the singular value that corresponds to the transition between occupied NTO $\tilde{i}$ and virtual NTO $\tilde{a}$ (included if above a given threshold), $|\Psi_{DA}\rangle$ is the determinant constructed from all occupied NTOs, and $|\Psi_{DA,\tilde{i}\tilde{a}}\rangle$ is prepared by promoting $\tilde{i}$ to $\tilde{a}$ in $|\Psi_{DA}\rangle$. With this approximation, the summation in eq. (3.3) only involves $O(M^2)$ terms so that the computational expense becomes tractable. Note that the NTO transformation was also applied in the *ab initio* exciton model developed by Morrison et al. for a similar purpose. [92]

3.2.2 Preparation of basis states

While ALMO-CIS calculations with closed-shell SCF(MI) references are straightforward, the proper handling of open-shell references can be rather challenging. Here we use He(↑↓)··He$^+$(↑) as an example to guide the discussion. The simplest way that one would consider to generate the reference state is to perform an unrestricted SCF(MI) calculation. [69] However, as the α and β electrons on the He atom are affected differently by the α electron on He$^+$, the neutral fragment will also be spin-polarized at the end of U-SCF(MI) calculation. In practice, we found that the ALMO-CIS states computed from such a U-SCF(MI) reference are often severely spin-contaminated, rendering the character of final MR-ALMOCIS states difficult to identify.

To alleviate the spin-contamination problem, we enforce each fragment to use the same set of spatial orbitals for α and β electrons so that each fragment remains restricted (R) or restricted open-shell (RO). The supersystem wavefunction, on the other hand, is not a spin eigenfunction but a spin-symmetry-broken state. To simplify the following discussion, we denote such a scheme as “FragRO-SCF(MI)”. Note that this scheme was employed by Levine et al. in the ALMO-EDA designed for studying single chemical bonds. [155, 156]

We then perform an unrestricted ALMO-CIS calculation on top of the FragRO-SCF(MI) reference and the resulting excited states (and the reference) can be employed as basis states in the final CI step. Note that these ALMO-CIS states are still not spin-pure as CIS amplitude equation differs for α and β orbitals, which makes $t_\alpha \neq t_\beta$ even on the neutral fragment. Moreover, using these ALMO-CIS states alone is unable to handle the coupling between a triplet excited state ($s = 1$) on the neutral He with He$^+$ ($s = 1/2$). According to the theory of angular momentum, such a coupling should yield a quartet ($S^2 = 3.75$) and a doublet ($S^2 = 0.75$) , while a spin-conserving excitation on top of the He(↑↓)··He$^+$(↑) reference can only generate states whose S^2 expectation value equals 2.75. In order to alleviate the spin-contamination problem of unrestricted ALMO-CIS as well as restore the correct S^2 values for states arising from a triplet-doublet coupling, a new set of reference states that can be denoted as He(↑↑)··He$^+$(↓) should also be added to the CI space, i.e., the neutral fragment is a high-spin triplet while the doublet fragment has the opposite spin. From the same FragRO-SCF(MI) reference, these states can be obtained by performing an $\alpha \to \beta$ spin-flip(SF)-ALMO-CIS calculation then swapping the α and β orbitals on each fragment. The SF-ALMO-CIS equation has a similar form as standard (spin-conserving) ALMO-CIS:

$$\mathcal{A}_{i\bar{a},j\bar{b}} t^{j\bar{b}} = \omega \mathcal{S}_{i\bar{a},j\bar{b}} t^{j\bar{b}} \tag{3.5}$$

i.e., an occupied α orbital (j) on one fragment is promoted to an empty β orbital (projected) belonging to the same fragment. The Hamiltonian matrix $\mathcal{A}$ can be constructed as follows:

$$\mathcal{A}_{i\bar{a},j\bar{b}} = F_{\bar{a}\bar{b}} S_{ij} - F_{\overline{i}\overline{j}} S_{ab} - (\overline{i}\overline{j}|ab) \tag{3.6}$$

where $\mathbf{F}$ and $\mathbf{S}$ denote the global Fock and overlap matrix, respectively. It resembles the $\mathcal{A}$ matrix for standard SF-CIS. [27] The addition of SF-ALMO-CIS states to the CI space

Table 3.1: Excitation energies (in eV) and S^2 by multiple methods for first 14 states of He_2^+ at 4 Å

State	CIS		MR-ALMOCIS		EOM-EE-CCSD		Full-CI		Character
	ΔE	S^2	ΔE	S^2	ΔE	S^2	ΔE	S^2	
0	0.00	0.75	0.00	0.75	0.00	0.75	0.00	0.75	He··He$^+$ in-phase
1	2.62	0.80	0.01	0.75	0.10	0.75	0.01	0.75	He··He$^+$ out-of-phase
2	19.07	2.67	18.46	3.75	18.21	2.77	18.16	3.75	$1s \to 2s$ quartet in-phase
3	19.78	0.85	18.65	0.75	18.62	0.98	18.32	0.75	$1s \to 2s$ doublet1 in-phase
4	21.29	2.60	19.16	0.75	19.59	1.48	18.70	0.75	$1s \to 2s$ doublet2 in-phase
5	21.71	2.73	20.77	3.74	20.38	2.94	20.28	3.75	$1s \to 2s$ quartet out-of-phase
6	21.71	2.73	21.26	0.76	20.67	2.65	20.56	0.75	$1s \to 2s$ doublet1 out-of-phase
7	21.79	0.77	21.38	3.75	20.67	2.65	20.67	3.75	$1s \to 2p_x$ quartet in-phase
8	21.79	0.77	21.38	3.75	20.71	0.86	20.67	3.75	$1s \to 2p_y$ quartet in-phase
9	22.03	1.15	21.41	0.75	20.71	0.86	20.69	0.75	$1s \to 2p_x$ doublet1 in-phase
10	22.32	2.44	21.41	0.75	20.88	1.01	20.69	0.75	$1s \to 2p_y$ doublet1 in-phase
11	22.52	0.76	21.47	0.75	21.23	2.75	20.72	0.75	$1s \to 2p_x$ doublet2 in-phase
12	22.89	2.73	21.47	0.75	21.41	0.76	20.72	0.75	$1s \to 2p_y$ doublet2 in-phase
13	22.89	2.73	21.90	0.75	21.85	2.68	20.97	0.75	$1s \to 2s$ doublet2 out-of-phase

enables nearly spin-adapted states to be obtained from the MR-ALMOCIS calculation, as illustrated in Sec. 3.3.

3.3 Application Examples

All calculations are performed with a development version of the Q-Chem 5.1 software package. [106] The geometric direct minimization (GDM) [157] algorithm is employed to converge the FragRO-SCF(MI) calculations. As in our previous works, [72, 73] a generalized Davidson algorithm is utilized to obtain the lowest-lying ALMO-CIS states from each SCF(MI) reference. To reduce the computational cost, we only include NTO pairs whose corresponding singular values are larger than 0.15 in the NOCI step.

3.3.1 He_2^+

We first illustrate the MR-ALMOCIS scheme with He_2^+, a simple system with two degenerate open-shell reference states. To study the excited states originating from the $1s \to 2s$ and $1s \to 2p$ transition of a neutral helium atom coupled with a helium cation (in its ground state, as the single electron is much more strongly bound than in neutral He), we included 26 basis states with $M_s = \frac{1}{2}$. The first 9 basis states include the ground state of $\mathrm{He}\cdots\mathrm{He}^+$ (ob-

Table 3.2: Excitation energies (in eV) and S^2 by multiple methods for first 14 states of He_2^+ at 10Å.

State	CIS		MR-ALMOCIS		EOM-EE-CCSD		Full-CI		Character
	ΔE	S^2	ΔE	S^2	ΔE	S^2	ΔE	S^2	
0	0.00	0.75	0.00	0.75	0.00	0.75	0.00	0.75	He··He$^+$ in-phase
1	2.62	0.80	0.00	0.75	0.10	0.75	0.00	0.75	He··He$^+$ out-of-phase
2	19.80	2.75	19.77	3.75	19.13	2.30	19.12	3.75	$1s \to 2s$ quartet in-phase
3	20.21	1.75	19.78	0.75	19.15	2.19	19.13	0.75	$1s \to 2s$ doublet1 in-phase
4	20.75	1.73	19.81	0.75	19.46	2.20	19.15	0.75	$1s \to 2s$ doublet2 in-phase
5	21.06	0.76	19.82	3.75	19.92	0.75	19.16	3.75	$1s \to 2s$ quartet out-of-phase
6	21.61	2.69	20.92	0.75	20.56	2.73	19.89	0.75	$1s \to 2s$ doublet1 out-of-phase
7	21.72	0.93	21.10	0.75	20.63	0.81	19.95	0.75	$1s \to 2s$ doublet2 out-of-phase
8	21.73	2.75	21.45	3.75	20.71	1.75	20.56	3.75	$1s \to 2p_z$ quartet in-phase
9	21.73	2.75	21.56	0.75	20.71	1.75	20.59	0.75	$1s \to 2p_z$ quartet in-phase
10	21.78	1.54	21.69	0.75	20.74	1.75	20.65	0.75	$1s \to 2p_z$ doublet1 in-phase
11	21.78	1.54	21.71	3.75	20.74	1.75	20.70	3.75	$1s \to 2p_x$ doublet1 in-phase
12	21.80	2.61	21.71	3.75	20.74	2.72	20.70	3.75	$1s \to 2p_y$ doublet2 in-phase
13	21.81	1.96	21.72	0.75	20.80	0.78	20.71	0.75	$1s \to 2p_x$ doublet2 in-phase

tained from SCF(MI)), and 8 ALMO-CIS excited states (singlet and triplet of one $1s \to 2s$ and three $1s \to 2p$ transitions on the neutral helium atom). The next 4 basis states account for the high-spin triplets of $1s \to 2s$ and $1s \to 2p$ on the neutral helium atom [He(↑↑)] coupled with a doublet helium cation in the opposite spin [He$^+$(↓)]. Because either one of the helium atoms can carry the positive charge, we can obtain another 13 states of the above characters starting from the He$^+\cdots$He reference.

In Table 3.1 and Table 3.2, we present the results for He-He distance of 4Å and 10Å and compare MR-ALMOCIS with standard CIS, EOM-EE-CCSD and Full-CI. We will focus on the lowest 14 states. All calculations employed a customized 6-311(2+)G basis, which includes two additional sets of diffuse functions to enable a better description of the Rydberg states of He. The MR-ALMOCIS method gives the same state structure as Full-CI. The ground and first low-lying excited state result from the coupling of two SCF(MI) references. Then, we see 6 states originating from the $1s \to 2s$ transition on the neutral helium atom. Because of the excitonic coupling, the 6 states first split into two groups, corresponding to in-phase and out-of-phase couplings, respectively. Within each group, the quartet and the lower doublet state come from triplet excitation of He coupled with the doublet He$^+$, and the higher doublet state comes from singlet excitation of He coupled with He$^+$. Similarly, $1s \to 2p_x$, $1s \to 2p_y$ and $1s \to 2p_z$ transitions on the neutral helium atom will also each result in 6 final states. We see pairs of states with the same excitation energies because of the degeneracy between $2p_x$ and $2p_y$. At short distance, the in-phase band of $1s \rightarrow 2p_{x/y}$ excitations crosses with the out-of-phase $1s \rightarrow 2s$ excitations, as illustrated in Figure 3.2. According to Tables 3.1 and 3.2, the standard CIS and EOM-EE-CCSD methods fail to produce the correct state structure and suffer from significant spin contamination. By including extra basis states (high-spin triplet excitations on neutral helium) generated from SF-ALMO-CIS calculations, the spin contamination issue is largely alleviated in MR-ALMOCIS, as indicated by the S^2 values that are close to Full-CI numbers (spin-pure).

It is also noteworthy that the split between the lowest two state is asymptotically correct with MR-ALMOCIS, i.e., at long distance, the two states are degenerate, as show in Figure 3.1. This is enforced by the symmetry of MR-ALMOCIS wavefunctions. At long distances, the excitonic coupling reduces to zero and the energies of MR-ALMOCIS states are the same as those of ALMO-CIS basis states. The standard CIS method, however, gives an unphysical excitation energy of 2.62 eV at 10Å) due to lack of orbital relaxation. EOM-EE-CCSD is also unable to fully resolve this problem, giving an excitation energy of 0.1 eV at long distance. Overall, standard CIS overestimates the excitation energies compared to Full-CI. MR-ALMOCIS makes a significant improvement over standard CIS, but is still unable to outperform EOM-EE-CCSD in terms of accuracy for excitation energies. This suggests that MR-ALMOCIS is able to capture static correlation through including basis states from multiple references, while further development of the method is required to account for dynamical correlation.

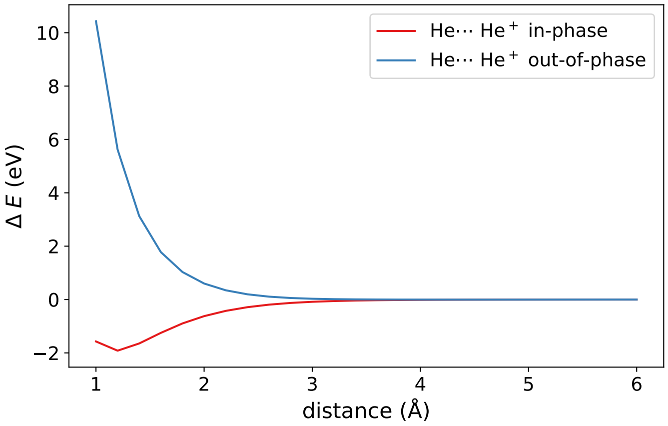

Figure 3.1: PES of the lowest two states for He_2^+ computed by MR-ALMOCIS. These two states mostly come from the in-phase and out-of-phase coupling of two SCF(MI) references ($He\cdots He^+$ and $He^+\cdots He$).

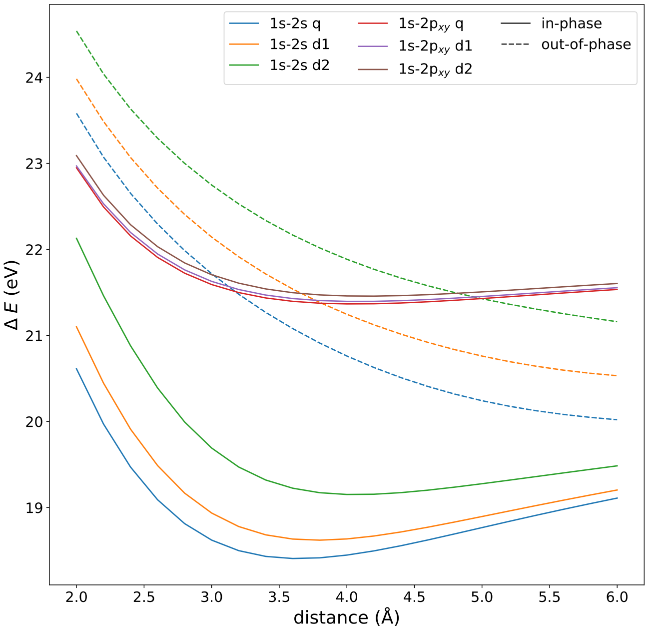

Figure 3.2: PES of the states 3–14 for He_2^+ computed by MR-ALMOCIS. Note that excitations dominated by the same character are connected so the curves are allowed to cross with each other.

3.3.2 water-Mg^{2+}

The next system we are looking at is the water-Mg^{2+} complex (see Fig. 3.3 for its structure). The Mg^{2+} is prone to accepting an electron from the water molecule. As a result, this system has several low-lying charge-transfer states. The lowest two CT states can be characterized as transitions from HOMO on water to $Mg^{2+}(3s)$, and HOMO-1 on water to $Mg^{2+}(3s)$. Higher in energy than these CT states, one can find states that resemble local excitations on the water molecule. We will be considering two such local excitations that correspond to transitions from the non-bond orbital (HOMO) to LUMO and LUMO+1, respectively. Both states have certain Rydberg characters. The relevant orbitals for these local excitations are plotted in Fig. 3.4.

To describe these four excited states and the ground state, our MR-ALMOCIS calculation includes 19 basis states from three reference SCF(MI) calculations. In the first reference, Mg is constrained to carry the +2 charge and water is set to be neutral. We solve for the ground state and six ALMO-CIS states that describe the local excitations on water. Next, given the FragRO-SCF(MI) solutions for the $H_2O^+ \cdot\cdot Mg^+$ configuration, we obtain the ground state and 5 charge-transfer excited states. We use two references with opposite spin constraint for the $H_2O^+ \cdot\cdot Mg^+$ configuration to facilitate spin adaptation when solving for the final

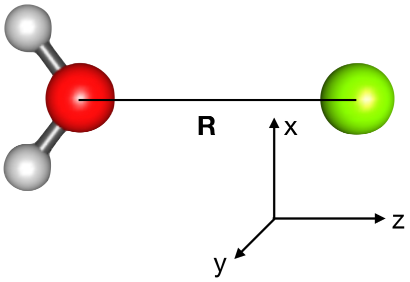

Figure 3.3: Illustration of water-Mg^{2+} system.

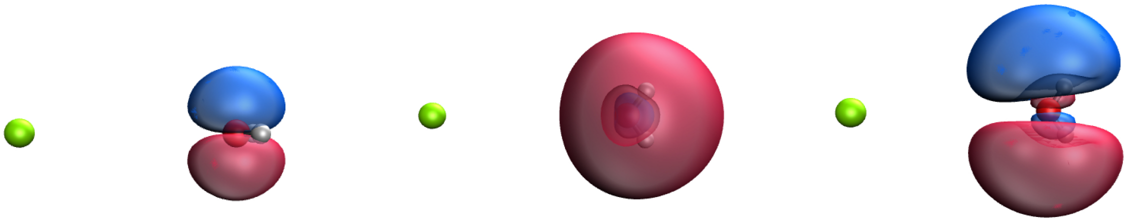

(a) water HOMO (b) water LUMO (c) water LUMO+1

Figure 3.4: Illustration of three most important molecular orbitals (calculated at the SCF(MI) level) involved in the two local excitations in water-Mg^{2+}. At 6 Å, the lowest local excitation on water is dominated by a transition from the non-bond orbital (HOMO) to LUMO, while the second lowest local excitation is dominated by the HOMO → LUMO+1 transition.

MR-ALMOCIS states. Note we have chosen the number of basis states to be larger than the number of target final states in case that the lowest ALMO-CIS states are not the ones that contribute the most to the lowest-lying MR-ALMOCIS states. In addition, a larger variational space also allows for better accuracy.

In Fig. 3.5, we scan the distance between Mg^{2+} and the oxygen atom and plot the potential energy curves for the five singlet states computed from MR-ALMOCIS. First we look at the lowest two states: at short distance, the closed-shell configuration ($H_2O{\cdot\cdot}Mg^{2+}$) has lower energy than the CT configuration water$^+$Mg$^+$ (which can be viewed as a CT from water's HOMO to the 3s orbital of Mg^{2+}). However, at large distance, these two states switch character, with the CT state becoming the ground state of the complex. The third state also has a charge-transfer character, which corresponds to the CT from H_2O(HOMO-1) to Mg^{2+}(3s) at large distance. The two highest states obtained correspond to the local HOMO→LUMO and HOMO→LUMO+1 excitations on water molecule at long distance. These two states also switch character at around 2.2 Å. The excitation energy corresponding to the HOMO→LUMO transition becomes pretty high in short range. A closer look at the

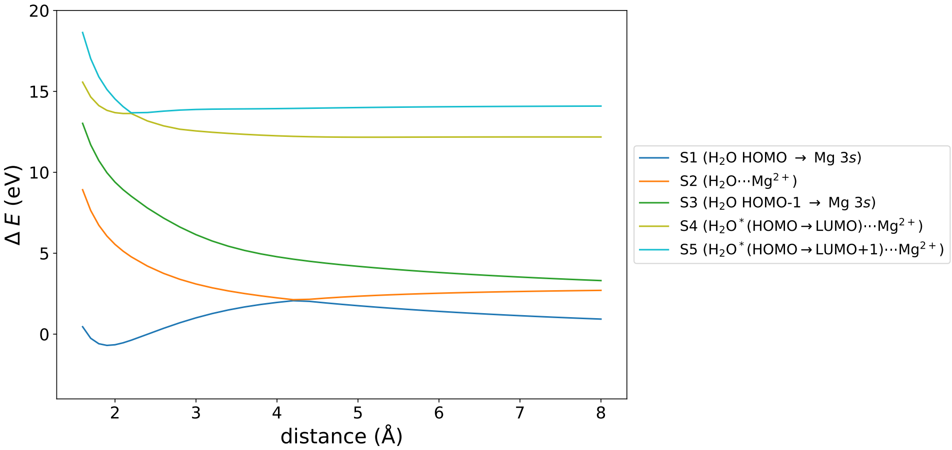

Figure 3.5: PES for 5 singlet states of $H_2O\cdots Mg^{2+}$ computed by MR-ALMOCIS with the 6-31G+(d) basis. The character of each state at long range are denoted in parentheses, while they are allowed to change at shorter distances.

MR-ALMOCIS Hamiltonian reveals that this local excitation is strongly coupled with the CT state from H_2O(HOMO) to $Mg^{2+}(3s)$, resulting in the significant rise of its excitation energy.

In Table 3.3 we compare the MR-ALMOCIS results with standard CIS and EOM-EE-CCSD at 2 Å, 4 Å, and 6 Å separations (O··Mg). For each method, the energy corresponding to the ground state of the closed-shell reference ($H_2O{\cdot\cdot}Mg^{2+}$) is chosen to be the zero-energy point. We compare the excitation energies of states with similar character, which may not have the same state number in different methods. For example, both MR-ALMOCIS and EOM-EE-CCSD predict that the $H_2O(\text{HOMO})\rightarrow Mg^{2+}(3s)$ CT state is lower than the closed-shell reference at 6 Å. As a general trend, CIS is inclined to overestimate excitation energies of CT states and it does not predict the crossing between the ionic and the lowest CT configurations within 6 Å. MR-ALMOCIS, on the other hand, usually gives lower excitation energies for CT states yet higher excitation energies for local states compared to the results of EOM-EE-CCSD.

3.3.3 TCNE-aromatic complexes

MR-ALMOCIS can also be employed to tackle charge-transfer excitations between organic molecules. Differing from the He_2^+ case, these systems have a well-defined (i.e. non-degenerate) ground reference state $|DA\rangle$, and the charge-transfer state $|D^+A^-\rangle$ is higher in energy. Nonetheless, MR-ALMOCIS can potentially provide a better description for charge-transfer excitations than standard CIS as the SCF(MI) preparation of $|D^+A^-\rangle$ can to some extent account for the effect of orbital relaxation.

Here we use the aromatic-tetracyanoethylene (Ar-TCNE) complexes that were studied by Stein et al. [127] as an illustrative example. The first excited state in these systems has

Table 3.3: Excitation energies (in eV) for the water-Mg^{2+} complex at 2 Å, 4 Å, and 6 Å intermolecular separations calculated by CIS, MR-ALMOCIS (denoted as "MR"), and EOM-EE-CCSD (denoted as "EOM"). All calculations are performed with the 6-31+G(d) basis. The excited states are sorted based on their characters, and the state energies in each column can change non-monotonically due to the crossing of states of different characters.

2 Å			4 Å			6 Å			Character
CIS	MR	EOM	CIS	MR	EOM	CIS	MR	EOM	
0	0	0	0	0	0	0	0	0	$H_2O\cdots Mg^{2+}$ (gs)
8.51	6.20	7.08	2.97	0.28	1.33	1.60	-1.12	-0.08	H_2O(HOMO) → Mg(3*s*)
11.85	10.05	10.37	5.06	2.82	3.77	3.59	1.28	2.24	H_2O(HOMO-1) → Mg(3*s*)
17.54	15.19	15.94	9.97	10.29	8.72	9.32	9.65	8.77	$H_2O^*(\text{HOMO}\rightarrow\text{LUMO})\cdots Mg^{2+}$
14.01	14.34	13.35	11.83	11.98	11.77	11.35	11.52	9.82	$H_2O^*(\text{HOMO}\rightarrow\text{LUMO+1})\cdots Mg^{2+}$

Table 3.4: Excitation energies (in eV) for charge transfer from Ar to TCNE.

	Benzene-TCNE	Toluene-TCNE	o-xylene-TCNE	Naphthalene-TCNE
MR-ALMOCIS	3.13	2.84	2.57	2.25
CIS	4.58	4.29	4.06	3.49
TDA(ωB97X-D)	2.94	2.70	2.44	1.97
CIS(D)	3.39	3.04	2.76	2.26
Exp. [127]	3.59	3.36	3.15	2.60

Table 3.5: Excitation energies (in eV) for the lowest local-exciton state on the aromatic ring in Ar-TCNE complexes.

	Standard CIS	MR-ALMOCIS
Benzene-TCNE	6.26	6.36
Toluene-TCNE	6.18	6.32
o-xylene-TCNE	6.15	6.27
Naphthalene-TCNE	5.35	5.58

a CT character, where the aromatic system serves as the electron donor and TCNE as the acceptor. The results for the excitation energy of this state with the donor being benzene, toluene, *o*-xylene and naphthalene are collected in Table 3.4. The geometries were taken from Ref. 127 and all calculations were performed with the 6-31G(d) basis.

We compare the MR-ALMOCIS results with standard CIS, TDA (with the ωB97X-D [158] functional), CIS(D), and also experimental results. All computational methods are able to reproduce the trend of decreasing excitation energies when the size of aromatic ring increases or when a methyl group is attached to the aromatic ring. Standard CIS tends to overestimate the excitation energies, yielding results that are roughly 0.9 eV higher than the experimental values. On the other hand, TDA with the (untuned) ωB97X-D functional significantly underestimates the excitation energies for the lowest CT state. MR-ALMOCIS excitation energies lie in between the results of TDA/ωB97X-D and standard CIS and thus are closer to the CIS(D) results (which serve as the theoretical reference here) than both: the CT excitation energy given by MR-ALMOCIS is typically 0.2 eV lower than the result of CIS(D), except for the naphthalene-TCNE system where excellent agreement between them is achieved.

It should be noted that MR-ALMOCIS is also able to predict excited states of local exciton (LE) character in these organic donor-acceptor systems, and the results should be similar to standard CIS. Table 3.5 compares the first LE state on the aromatic ring calculated by standard CIS and MR-ALMOCIS: for each system, the excitation energy given by MR-ALMOCIS is consistently 0.1–0.2 eV higher than that by standard CIS. This discrepancy stems from the lowering of ground state in MR-ALMOCIS, as well as the inexactness of ALMO-CIS (compared to full CIS) and NTO approximations. The ability of obtaining "absolutely localized" excitonic states together with CT states makes MR-ALMOCIS a suitable tool for studying the couplings between them, [159] which would be a useful future application of this method as these couplings play an important role in photochemical processes such as photo-induced electron transfer.

3.4 Conclusion

In this work, we extended the previously developed ALMO-CIS method to treat a class of complexes with a multi-reference nature. The resulting scheme, MR-ALMOCIS, shows several favorable features for a number of test systems. For He_2^+, MR-ALMOCIS significantly improves the excitation energies over standard CIS and reduces the amount of spin contamination compared to CIS and EOM-CCSD. It gives correct state structure (consistent with Full-CI) and reproduces the degeneracy of the lowest two states at long range, which even high-level method such as EOM-CCSD fails to produce. This should transfer to more complex excimers with degenerate ground state. For water-Mg^{2+}, MR-ALMOCIS successfully predicts the crossing between the closed-shell reference and the lowest charge transfer state. It also manages to describe several other charge-transfer excitations from H_2O to Mg^{2+}. For the Ar-TCNE complexes, MR-ALMOCIS gives more accurate results for the lowest CT state compared to conventional methods such as CIS or TDA.

We note that the current MR-ALMOCIS method still has several limitations that could be possible directions of future work:

1. The multi-reference scheme only allowed us to capture static correlation. As a result, MR-ALMOCIS still suffers from the error caused by lack of dynamical correlation and often shows lower accuracy than methods such as CIS(D) and EOM-CCSD that are designed

to account for dynamic correlation. As a next step, one may consider including double excitations in a perturbative way as done in CIS(D) or NOCI-MP2.

2. Choosing the reference and determining how many basis states to include in the CI space requires knowledge of the systems, which makes the MR-ALMOCIS scheme not entirely "black-box". Further, the number of basis states required is often larger than the number of states we target. Otherwise, we may not be able to get satisfactory results for those high-lying states, as for the local excitation in water-Mg^{2+}. These problems might be addressed by solving for the MR-ALMOCIS wave-function directly, i.e. fully relaxing the amplitudes starting from multiple references without constructing ALMO-CIS basis states from each reference first.

3. Although we have adjusted the MR-ALMOCIS scheme to avoid missing important spin configurations, the current scheme is still not strictly spin pure. For open-shell systems, although each fragment is R or RO in the SCF(MI) solution, the overall SCF(MI) state is an unrestricted wavefunction and an unrestricted ALMO-CIS calculation is performed on top of it. Therefore, spin contamination can still occur, especially at short distances where the ALMO-CIS amplitudes might be more severely spin-polarized (imagine the α and β amplitudes on He when it is in close contact with a doublet He^{+}). Following the idea of ROCIS [160] and spin-adapted SF-CIS [161, 162] may help address the spin contamination issue in this method.

4. As formulated here, MR-ALMOCI is restricted to describing excitations in molecular clusters. Yet the issue of achieving balance in describing CT and local excitations also arises in large molecules such as dyes with multiple interesting functional groups[163, 164]. It will be interesting to consider extensions or alternations to MR-ALMOCIS to address such problems.

Chapter 4

Energy Decomposition Analysis for Exciplexes

4.1 Introduction

Environment effects on ground states are the basis of solvation phenomena which are well-known to strongly affect solute molecular properties and chemical reactivity. Since electronically excited states involve less strongly bound electrons, often with much larger polarizabilities, environment effects on such states will typically be larger as well as less chemically intuitive than for ground states. One example is the study of the solvent effects on excitation energies, i.e., solvatochromism. Most dielectric continuum models[165–167] and combined quantum mechanics and molecular mechanics (QM/MM) methods[168–170] focus on the electrostatic effect (permanent and induced) of solvent on the solute molecules. Other studies also pointed out that intermolecular Pauli repulsion is important especially when the solute excited states are rather diffuse[171], and recently Kongsted and co-workers addressed this problem by introducing an effective confinement of the solute wavefunction[**olsen2015polarizable**, 172]. Anther interesting topic is the charge-transfer-to-solvent (CTTS) spectra[38], a unique class of electronic spectra which are present in dipolar (e.g., aqueous) solution of small inorganic anions such as halides, OH^- and NO_3^-. These anions undergo ionization rather than excitation in their gas phase, but can form stable excited states in solutions. There have been extensive experimental[39–41] and theoretical[42–47] studies on the CTTS spectra, and this phenomenon is often explained by transfer of charges from anions to solution, where the delocalized electron is stabilized by the surrounding solvent molecules.

Electrostatics, dispersion, and polarization (POL) are the three types of long-range forces by which non-overlapping molecules interact[36]. In addition, Pauli repulsion, and charge transfer (CT) are well-known repulsive and attractive forces between overlapping molecules. However, the definition of all terms in the overlapping regime is inherently non-unique. Energy decomposition analysis (EDA) decomposes the total interaction energy into several scalars corresponding to the aforementioned terms, thereby allowing an assessment of their relative importance. Many EDA schemes have been proposed and used for studying intermolecular interactions between molecules in their ground states, as discussed below. However, there are very few reported EDA approaches for excited states. Recently, Slipchenko *et al.* reported the hybrid QM/EFP (effective fragment potential) model[173–175] for studying excited states in the presence of a solvent environment. Other approaches aiming to construct the effective potential exerted by the environment as a combination of several physically meaningful components, such as the frozen density embedding (FDE) [**wesolowski1993**, **wesolowski2015frozen**, **Neugebauer2005**] and polarizable density embedding (PDE) [**olsen2015polarizable**, **reinholdt2017polarizable**, 172] schemes, can also be utilized to model solvatochromic shifts. The fragment molecular orbital (FMO) method has also been extended to excited states[176] and used to distinguish the role of POL and CT on examples of solvatochromism. Excited states of large clusters can also be treated by ab initio implementations of the Frenkel-Davydov exciton model[177–179], which uses a basis of monomer excitations, and reveals inter-monomer state mixings. These approaches all represent useful *adaptations* of numerical methods for interpretive purposes, rather than a systematic effort to *design* an excited state EDA.

Among the EDA schemes designed for ground state interactions, two main categories are symmetry-adapted perturbation theory (SAPT) [49–53] and variational approaches[54–70]. SAPT evaluates intermolecular interaction energies through a perturbative approach, and it also provides a decomposition of the resulting energies into electrostatic, exchange-repulsion, induction and dispersion terms. Recent SAPT advances include efficiency improvements using Kohn-Sham (KS)-DFT [180, 181] and efforts to separate POL and CT in the induction term. [182–184] Variational EDA methods date back to the early Kitaura-Morokuma [54, 55] (for the Hartree-Fock (HF) theory) and Ziegler-Rauk [56, 57] (for the Xα method) approaches. Such methods partition intermolecular interaction energies by constructing constrained intermediate states whose energies are upper bounds to the true total energy.

The absolutely localized molecular orbital (ALMO)-EDA [68, 69] (and the closely related block-localized wavefunction (BLW)-EDA [63–65, 185]) is a more recent variational EDA that separates the total interaction into contributions from frozen interactions (FRZ), POL and CT. Its main feature is the use of two intermediate states: an antisymmetrized Heitler-London wavefunction constructed from converged MOs of the monomers directly (for the evaluation of FRZ), and a variationally optimized state whose associated AO-to-MO coefficient matrix is constrained to be fragment-block-diagonal (to separate POL and CT), using the so-called “self-consistent field for molecular interactions” (SCF-MI) approach[99, 145, 186]. Recent improvements to the ALMO-EDA include the development of the fragment electrical response function (FERF) model [187] that yields POL (and CT) energies with a meaningful complete basis set (CBS) limit, and a decomposition of the frozen term into contributions from permanent electrostatics, Pauli repulsion and dispersion [188]. These advances define the second generation of the ALMO-EDA method. [70] Additionally a new connection between ALMO-EDA energy contributions and experimental observables has been achieved with the “adiabatic” ALMO-EDA[189] that optimizes the structure and evaluates properties such as vibrational frequencies and dipole moments on each constrained potential energy surface.

Some recent developments encourage us to formulate an EDA scheme based on ALMOs for intermolecular interactions involving excited states. The first is the development of ALMO-CIS[102], a local variant of the configuration interaction singles (CIS) method[9, 10]. The ALMO-CIS wavefunction is constructed from superposition of on-fragment single excitations, i.e., from a fragment-localized occupied orbital, we only allow excitations to virtual orbitals that are tagged to the same fragment. ALMO-CIS excludes inter-fragment charge transfer in a natural way and one can prove that it conserves fragment Mulliken populations[71]. This suggests that the CT term can be defined as the difference between excited state energies evaluated by ALMO-CIS and standard CIS, generalizing the ground state CT which is the difference between converged SCF-MI and full SCF energies. The second development is that the ALMO-EDA has been recently extended from SCF wavefunctions to post-SCF methods at the MP2 level[101, 190]. In MP2-ALMO-EDA, the MP2 correlation energy is separated into contributions from four components: FRZ, POL, CT and dispersion, and the first three are then added to their counterparts in the Hartree-Fock ALMO-EDA. Here we may follow a similar procedure to formulate a CIS-based EDA, as the CIS wavefunction is generated from the HF wavefunction, and the CIS excited state energy can be expressed as a sum of the ground state (HF) energy and the excitation energy.

In this work, we present a new EDA scheme for the study of intermolecular interaction involving excited molecules based on CIS (or linear response theory for single excitations, to be more general, including time-dependent density functional theory (TDDFT)[9, 31–33], particularly in the Tamm-Dancoff approximation (TDA)[34]). We focus our methodology development on cases where the excitation can be assigned to a single molecule within a complex, as is appropriate for solvatochromism, for example. The remainder of the paper is organized as follows: in Sec. 5.2, we outline the theory for this new ALMO-EDA scheme. We then present a series of case studies in Sec. 4.3. Some limitations of the method are discussed in Sec. 4.4 including types of systems where the current scheme could fail.

4.2 Theory

The EDA presented here uses linear response theory for single substitutions to treat the excited state. In this section, we present the approach as generally as possible, using CIS in one or two specific places where it is necessary to illustrate the formalism. Thus the general expressions below may be specialized to the CIS case by identifying ground state energies as Hartree-Fock, $E = E_{\text{HF}}$, unconstrained excited state energies as CIS, $E^* = E^*_{\text{CIS}}$, and ALMO ground and excited states as ALMO-HF and ALMO-CIS respectively. The EDA scheme is readily extensible to TDDFT in the TDA approximation (and we have implemented the method for this latter case also). Since nonorthogonal orbitals are used at the frozen and polarized level, we occasionally need to employ tensor notation, where subscripts imply covariant quantities (like orbitals or matrix elements), and superscripts imply contravariant quantities such as excitation amplitudes[104].

The interaction energy associated with an excited cluster is defined as the difference between the excited supersystem energy, E^*, and the corresponding sum of fragment energies, E^*_{frag}, with a counterpoise correction for basis set superposition error (BSSE):

$$\Delta E^{\star}_{\text{INT}} = E^* - E^*_{\text{frag}} + \Delta E^*_{\text{BSSE}} \tag{4.1}$$

To define E^*_{frag}, we assume that one of the fragments (labeled as fragment 1) has an excitation energy lower than the other fragments, as might be the case for a solute embedded in a solvent cluster. In that way, E^*_{frag} is the sum of isolated fragment energies, with fragment 1 excited and the rest remaining in the ground state:

$$E^*_{\text{frag}} = E^*_1 + \sum_{J>1} E_J \tag{4.2}$$

Since $E^* = E + \omega$ and $E^*_{\text{frag}} = \sum_J E_J + \omega_1$ (ω_1 is the excitation energy of the isolated fragment $F1$), we can separate the contribution from ground state and excitation energy as:

$$\Delta E^*_{\text{INT}} = \Delta E_{\text{INT}} + \Delta\omega_{\text{INT}} \tag{4.3}$$

where $\Delta E_{\text{INT}} = E - \sum_J E_J$ is the ground state interaction energy and $\Delta\omega_{\text{INT}} = \omega - \omega_1$.

We note that there are different choices for the geometries of the isolated fragments as well as the complex. Using optimized ground state geometries for both fragment and complex is appropriate for a vertical excitation as a model of absorption spectra. On the other hand, geometries optimized for excited states (E^* for the complex, E^*_1 for isolated fragment $F1$) are also required for studying emission spectra. We shall confine ourselves to the absorption case here.

First we briefly recapitulate the decomposition of the ground state interaction energy ΔE_{INT}. Given a fixed geometry of a complex, the first-generation ground state ALMO-EDA[68] decomposes the ground state interaction energy (ΔE) into frozen (FRZ), polarization (POL) and charge transfer (CT) contributions:

$$\Delta E_{\text{INT}} = \Delta E_{\text{FRZ}} + \Delta E_{\text{POL}} + \Delta E_{\text{CT}} \tag{4.4}$$

The separation of these three terms is achieved by defining the frozen and polarized intermediate states. The frozen MO coefficient matrix is constructed by concatenating the isolated fragment MOs, and the energy of the frozen state (E_{FRZ}) is computed using the associated one-particle density matrix. At the polarized level, the MOs are relaxed subject to the constraint that the MO coefficient matrix is fragment-block-diagonal, i.e., the MOs are "absolutely localized". [68, 145] The energy lowering relative to the frozen state defines the polarization energy (ΔE_{POL}). Finally, an unconstrained SCF calculation is performed for the whole system, yielding the fully relaxed ground state energy denoted as E. The ground state FRZ, POL and CT terms are thus defined as:

$$\Delta E_{\mathrm{FRZ}} = E_{\mathrm{FRZ}} - \sum_J E_J \tag{4.5}$$

$$\Delta E_{\mathrm{POL}} = E_{\mathrm{POL}} - E_{\mathrm{FRZ}} \tag{4.6}$$

$$\Delta E_{\mathrm{CT}} = E - E_{\mathrm{POL}} + \Delta E_{\mathrm{BSSE}} \tag{4.7}$$

In the excited state EDA, we want to define the frozen and polarized wavefunctions for the excited system (and their associated energies E^*_{FRZ} and E^*_{POL}) so that the excited state interaction energy (E^*) can be decomposed into the same three terms as in the ground state EDA.

$$\Delta E^*_{\mathrm{INT}} = \Delta E^*_{\mathrm{FRZ}} + \Delta E^*_{\mathrm{POL}} + \Delta E^*_{\mathrm{CT}} \tag{4.8}$$

For the reasons discussed in the introduction, we use the ALMO-CIS wavefunction (or its TDDFT or TDDFT/TDA analog as appropriate) to describe the polarized excited system, whose energy is labeled as E^*_{POL}. The CT contribution to the excited state interaction energy is then accounted for by the difference between the unconstrained and polarized excited state energies (with basis set superposition error correction included also).

$$\Delta E^*_{\mathrm{CT}} = E^* - E^*_{\mathrm{POL}} + \Delta E^*_{\mathrm{BSSE}} \tag{4.9}$$

Recalling that in the ground state ALMO-EDA, $\Delta E_{\mathrm{CT}} = E - E_{\mathrm{POL}} + \Delta E_{\mathrm{BSSE}}$, the CT term can also be rewritten as:

$$\Delta E^*_{\mathrm{CT}} = \Delta E_{\mathrm{CT}} + \Delta\omega_{\mathrm{CT}} \tag{4.10}$$

where $\Delta\omega_{\mathrm{CT}} = \omega - \omega_{\mathrm{POL}} + \Delta E^*_{\mathrm{BSSE}} - \Delta E_{\mathrm{BSSE}}$.

Next, at the frozen level, we want to freeze both the orbitals and the excitation amplitudes. Then we calculate the frozen excitation energy using the isolated fragment amplitudes $\mathbf{t}_1$. The effect of other fragments enter only through the frozen Fock matrix. Specializing to CIS, we obtain:

$$\begin{aligned}\omega_{\mathrm{FRZ}} = &\sum_{i,a,j,b\in F1} (F_{ab}S_{ij}t_1^{ia}t_1^{jb} - F_{ij}S_{ab}t_1^{ia}t_1^{jb}) \\ &+ \sum_{i,a,j,b\in F1} \langle\psi_i\psi_b||\psi_a\psi_j\rangle t_1^{ia}t_1^{jb} \\ &+ 2\sum_{i,a\in F1} F_{ia}z_1^{ia}\end{aligned} \tag{4.11}$$

The form of the first two terms in the above equation are the same as the non-orthogonal CIS energy with isolated fragment amplitudes, $\mathbf{t}_1$. The last term, which involves the occupied-virtual block of the relaxed density of the isolated fragment ($\mathbf{z}_1$), is a correction term that is necessary to obtain the correct electrostatics in the non-overlapping regime[101]. To understand this latter term, one should notice that at long distance, the frozen term is dominated by electrostatics and we expect:

$$\frac{\partial\omega_{\mathrm{FRZ}}}{\partial\mathbf{E}} = \boldsymbol{\mu}^1_{\mathrm{CIS}} \tag{4.12}$$

Differentiating the first two terms in eq. 5.7 gives $\mathrm{Tr}(\boldsymbol{\mu}\mathbf{P}_1)$, where $\boldsymbol{\mu}$ is the dipole matrix in the AO basis, and $\mathbf{P}_1$ is the unrelaxed CIS difference density of fragment 1:

$$\begin{aligned} P_1^{ab} &= S_{ij} t_1^{ia} t_1^{jb} \\ P_1^{ij} &= -S_{ab} t_1^{ia} t_1^{jb} \end{aligned} \tag{4.13}$$

Only when the last term is present, the correct dipole moment, which is evaluated as $\mathrm{Tr}(\boldsymbol{\mu}\tilde{\mathbf{P}}_1)$ using the relaxed density, $\tilde{\mathbf{P}}_1$, can be recovered. The same issue arose in the MP2-ALMO-EDA, where an additional term is also needed for the frozen energy (see ref. 101 for further discussion). Even so, there remains some ambiguity in the overlapping regime, which we now resolve. When the fragments overlap, we force the virtual space to be orthogonal to the occupied space so as to make the excitation well defined. Moreover, we reorthogonalize the virtual orbitals within fragments so that in this projected-then-reorthogonalized basis, the fragment excited states remain properly orthogonal to each other.

The frozen and polarization interaction of the excited system is defined as:

$$\begin{aligned} \Delta E^*_{\mathrm{FRZ}} &= \Delta E_{\mathrm{FRZ}} + \omega_{\mathrm{FRZ}} - \omega_1 \\ &= \Delta E_{\mathrm{FRZ}} + \Delta\omega_{\mathrm{FRZ}} \end{aligned} \tag{4.14}$$

$$\begin{aligned} \Delta E^*_{\mathrm{POL}} &= \Delta E_{\mathrm{POL}} + \omega_{\mathrm{POL}} - \omega_{\mathrm{FRZ}} \\ &= \Delta E_{\mathrm{POL}} + \Delta\omega_{\mathrm{POL}} \end{aligned} \tag{4.15}$$

So far, we have defined the three terms in the EDA for excited states and shown that all these terms can be split into a contribution from the ground state (ΔE, obtained by the ground state ALMO-EDA) as well as corrections arising from the excitation energies ($\Delta\omega$). This is because with the linear response theory, the wavefunction at each level of EDA uses their ground state counterpart as a reference.

The decomposition of ΔE^* tells us the components of interaction between excited and unexcited fragments, while the decomposition of $\Delta\omega$ is useful to interpret phenomena such as solvatochromic shifts. There is no definite sign for the $\Delta\omega's$. For example, the sign of $\Delta\omega_{\mathrm{POL}}$ can depend on whether polarization in the excited state is more or less favorable than in the ground state. Since ALMO-CIS and standard CIS use different molecular orbitals, the intra-fragment restriction on excitation amplitudes made in ALMO-CIS does not make the ALMO-CIS excitation energy an upper bound to full CIS, which means $\Delta\omega_{\mathrm{CT}}$ can sometimes be positive. Also, there is no guarantee for the relative magnitude of $\Delta\omega$ and ΔE, implying that in extreme cases $\Delta E^*_{\mathrm{POL}}$ and ΔE^*_{CT} can also be positive (which appears unintuitive). This possibility stems from the fact that the excited state is not treated in an equal manner as the ground state, as linear response theory is utilized to evaluate the excitation energies, which uses the ground state wavefunction as the reference.

The frozen interaction can be further decomposed. One simple scheme is to define the electrostatic term as the Coulomb interaction between charge distributions of isolated fragments (the "quasi-classical" definition of electrostatics):

$$\Delta E^*_{\mathrm{CLS\_ELEC}} = \sum_{I<J} \iint d\mathbf{r}_1 d\mathbf{r}_2 \rho_I^{tot}(\mathbf{r}_1) r_{12}^{-1} \rho_J^{tot}(\mathbf{r}_2) \tag{4.16}$$

where $\rho_I^{tot}(\mathbf{r}) = \rho_I^{ele}(\mathbf{r}) + \rho_I^{nuc}(\mathbf{r})$ is the sum of nuclear and electronic densities of an isolated fragment. We use the relaxed CIS state density for the excited fragment and HF density for the rest (or the appropriate DFT analogs).

The Pauli term is then defined as the remainder of the frozen energy:

$$\Delta E^*_{\mathrm{PAULI}} = \Delta E^*_{\mathrm{FRZ}} - \Delta E^*_{\mathrm{CLS\_ELEC}} \tag{4.17}$$

We note that the Pauli term defined in this way is contaminated by dispersion if TDDFT or TDA is used, especially when employing dispersion-corrected functionals. It has been shown that for the ground state, this could lead to a negative Pauli term in the long range, which is deemed unphysical. A more rigorous method has been proposed by Horn *et al.* to decompose the ground state interaction energy into electrostatic, Pauli and dispersion terms[188]. This could potentially be generalized to excited states cases in the future.

4.3 Applications examples

The excited state ALMO-EDA has been implemented in a development version of the Q-Chem electronic structure program[106]. As tests of our EDA scheme, we apply it to five diverse systems: (a) water-charge interaction, (b) neon-helium and helium dimers, (c) formamide-water dimer, (d) pyridine/pyrimidine-water, and (e) halide-water. For systems (a), (c) and (e), the geometries are optimized with MP2[16] and the 6-311++G(2d,2p) basis set[191, 192], and EDAs are performed at the CIS/aug-cc-pVTZ[193, 194] level. For system (b), we also use MP2 for geometry optimization and CIS for EDA, but a modified 6-311(2+)G basis set is employed for the calculations for a better description of the Rydberg States. System (d) uses geometries provided by the supporting information of a related study[195], and the EDA is based on TDDFT with the Tamm-Dancoff approximation (TDA)[34] at the ωB97X-D[158]/6-311++G(d,p)[191] level of theory. Counterpoise corrections for BSSE are applied to all the EDA calculations.

4.3.1 Water-charge

The lowest singlet excited state of water is $1^1\mathrm{B}_1$, with primarily valence character[196]. We investigate its interaction with a +1 point charge placed on the bisector of the HOH angle (on the oxygen side, as shown in Figure 4.1). This system is equivalent to $\mathrm{H_3O^+}$, with one variable OH distance, and two fixed distances. Since there is only one fragment involved, the ALMOs are the canonical MOs and ALMO-CIS is equivalent to full CIS. This means that the charge transfer term is zero by definition. To obtain the frozen and polarization terms, we need to compute (1) ω_1: the excitation energy of water in the absence of the point charge; (2) $\omega_{\mathbf{FRZ}}$: as defined in eq. 5.7, where the amplitudes are frozen and the perturbation enters through the Fock matrix; (3) $\omega_{\mathbf{POL}}$: obtained from a full CIS calculation on water in the presence of the charge.

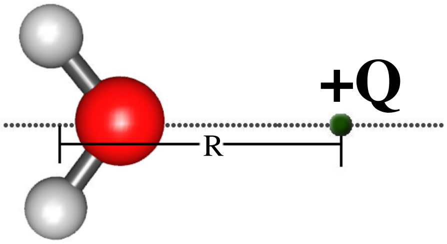

Figure 4.1: Water molecule interacting with a point +1 charge. R is the distance between the center of nuclear charges of water and the point charge.

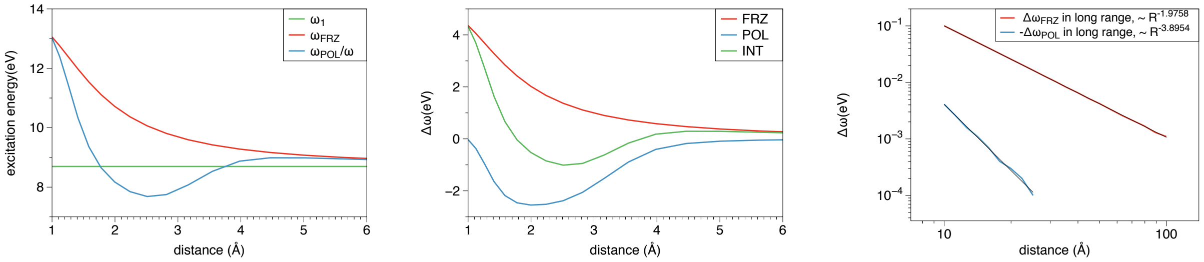

(a) (b) (c)

Figure 4.2: (a) Excitation energy of water in the presence of a +1 charge at the isolated fragment (ω_1), frozen (ω_{FRZ}), and polarized (ω_{POL}) levels. (b) Decomposition of the shifts in excitation energy: the sum of the FRZ and POL contributions gives the total shift ("INT") due to the presence of +1 charge. (c) Plots of $\Delta\omega_{\text{FRZ}}$ and $\Delta\omega_{\text{POL}}$ vs. R at long range, on a logarithmic scale.

We scan the distance between water (using the center of nuclear charges) and the point charge to obtain potential energy curves for each level of excitation energies (Figure 4.2(a)), and the distance dependence of $\Delta\omega_{\mathbf{FRZ}}$, $\Delta\omega_{\mathbf{POL}}$ and $\Delta\omega_{\mathbf{INT}}$ (Figure 4.2(b)). A necessary condition for our EDA scheme to be legitimate is that the frozen and polarization terms must have the correct long-range behavior. Since there is no Pauli repulsion in this case, we expect to see that the frozen term decays as R^{-2}, which is the correct behavior of a permanent charge-dipole interaction. The polarization term, on the other hand, should have an R^{-4} distance dependence, which is the character of a charge-induced dipole interaction. As shown in Figure 4.2 (c), for the data points beyond 10 Å, the plots of $\log(\Delta\omega_{\mathbf{FRZ}})$ and $\log(-\Delta\omega_{\mathbf{POL}})$ vs. $\log R$ have slopes -1.98 and -3.90, respectively, which are each quite close to the expected values.

In the short range, the repulsive frozen (electrostatic) term is simply a consequence of the sign-flipping of the water dipole upon excitation. The short-range behavior of the polarization term is more complicated as it is not monotonic. To understand the polarization behavior, we look at how water's ground and excited state dipole moments vary when a +1

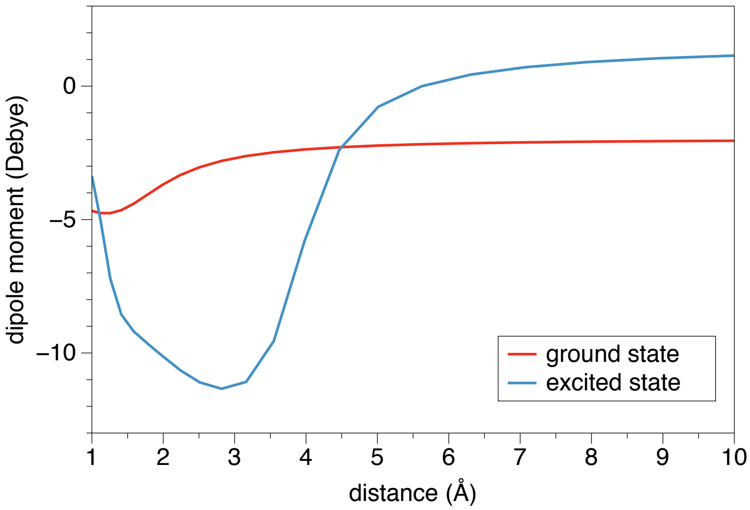

Figure 4.3: Values of the ground and first excited state dipole moments of water varying with its distance from the +1 charge. When the point charge is absent, $\mu(\infty) = -1.98$ D, $\mu^*(\infty) = 1.51$ D.

point charge is approaching (Figure 4.3). In the long range, the dipole moments of the ground and excited states have opposite signs. Nonetheless, the positive charge always pulls electron density towards itself, and the induction effect is substantially stronger in the more polarizable excited state. Therefore, at short distances ($R < 4.5$ Å), the excited state dipole moment becomes even more negative than that of the ground state.

These facts are also reflected in the contour plots of electron densities (Figure 4.4), from which we can see that at both 2.8 Å and 5.0 Å, the electrons move towards the charge and the changes in excited state densities are more substantial. The difference density $\Delta\rho = \rho^* - \rho$ has different patterns at 2.8 Å and 5.0 Å, which is consistent with the relative magnitude of dipole moments for ground and excited states. When the distance becomes smaller than 3 Å, the excited state dipole increases again. This is most likely because now the point charge penetrates the electron density of water and only part of its polarizing effect contributes to the decrease of the dipole moment. This does not happen to the ground state until R is close to 1 Å since the ground state electron density is less diffuse than that of the excited state.

4.3.2 Neon-helium dimer, clusters and helium dimer

The first singlet excited state of Ne is a $2p{\rightarrow}3s$ Rydberg state, at 18.4 eV, whereas the lowest singlet excited state of He ($1s{\rightarrow}2s$) is much higher (21.1 eV). Therefore the lowest singlet excitation of the Ne-He dimer is expected to be Ne($2p{\rightarrow}3s$) perturbed by the presence of helium. The Ne-He distance is scanned from 1 Å to 6 Å. The excitation energy is found to be blue-shifted for distances between 1.9 Å and 4.3 Å, which is mainly due to Pauli repulsion (see Figure 4.5(b)). As the Rydberg excited state is far more diffuse than the ground state, we expect greater Pauli repulsion at long distances for the excited state because of the

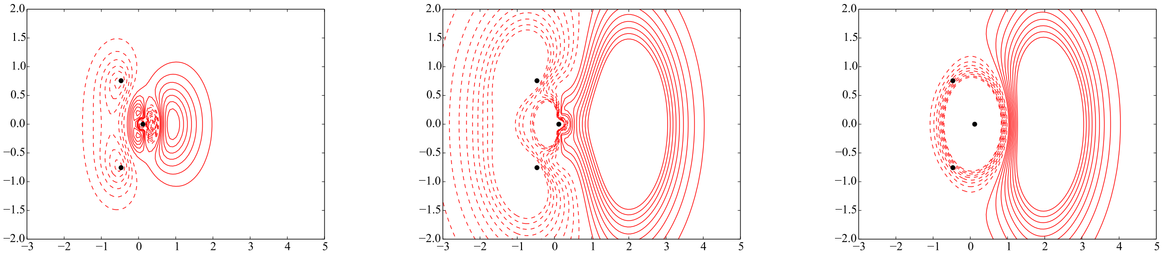

$\rho(2.8\text{Å}) - \rho(\infty)$ $\rho^*(2.8\text{Å}) - \rho^*(\infty)$ $\rho^*(2.8\text{Å}) - \rho(2.8\text{Å})$

(a) +Q at 2.8Å, $\mu = -2.80$ D, $\mu^* = -11.34$ D

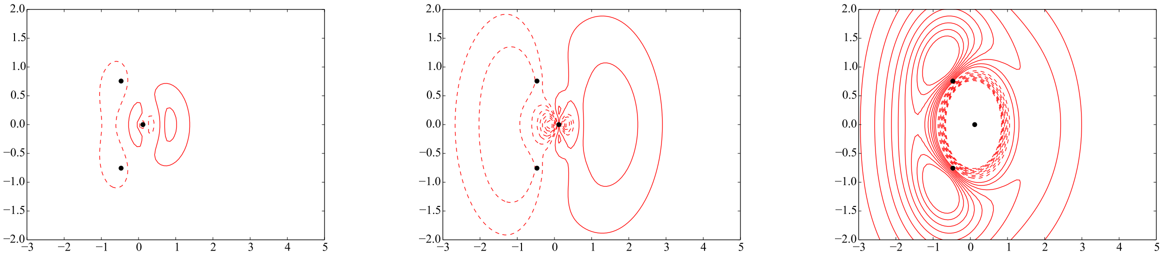

$\rho(5\text{Å}) - \rho(\infty)$ $\rho^*(5\text{Å}) - \rho^*(\infty)$ $\rho^*(5\text{Å}) - \rho(5\text{Å})$

(b) +Q at 5.0Å, $\mu = -2.23$ D, $\mu^* = -0.19$ D

Figure 4.4: Electron density difference (EDD) contours showing changes upon the excitation from the ground to first excited state of water in the presence of a +1 point charge located at $R =$ (a) 2.8 Å and (b) 5 Å. In each row, the first and second panels exhibit the polarization effect due to the +1 point charge, and the third panel shows the difference between the ground and excited state densities. Values plotted are integrated to the molecular plane ($\Delta\rho(x,y) = \int \mathrm{d}z \Delta\rho(x,y,z)$), and the contours are evenly spaced at $0.1\text{e}^-/\text{Å}^3$ with positive ones solid and negative ones dashed. The black dots indicate the positions of water's nuclei.

increased overlap between electronic density of helium and neon.

From Figure 4.5(b), it is interesting to see that the Pauli term begins to drop when the distance becomes smaller, and the excitation energy (Figure 4.5(a)) exhibits a red shift for small enough distances. At small distances, the ground state is also subject to significant Pauli repulsion, so that the difference between excited and ground state becomes less prominent. From Figure 4.5(b), we also see that polarization is significantly more favorable for the excited state (i.e. the Rydberg excited state is far more polarizable than the ground state). CT is also slightly more favorable in the excited state for distances smaller than 4.4 Å.

The spectra of small helium clusters have been studied experimentally[77–79] and theoretically[71, 80, 102]. By examining the eigenstates, it has been shown that the red-edge states mainly come from surface excitations, while the blue-edge states have predominantly bulk character. To explore the origin of this effect with a model system, we perform an EDA

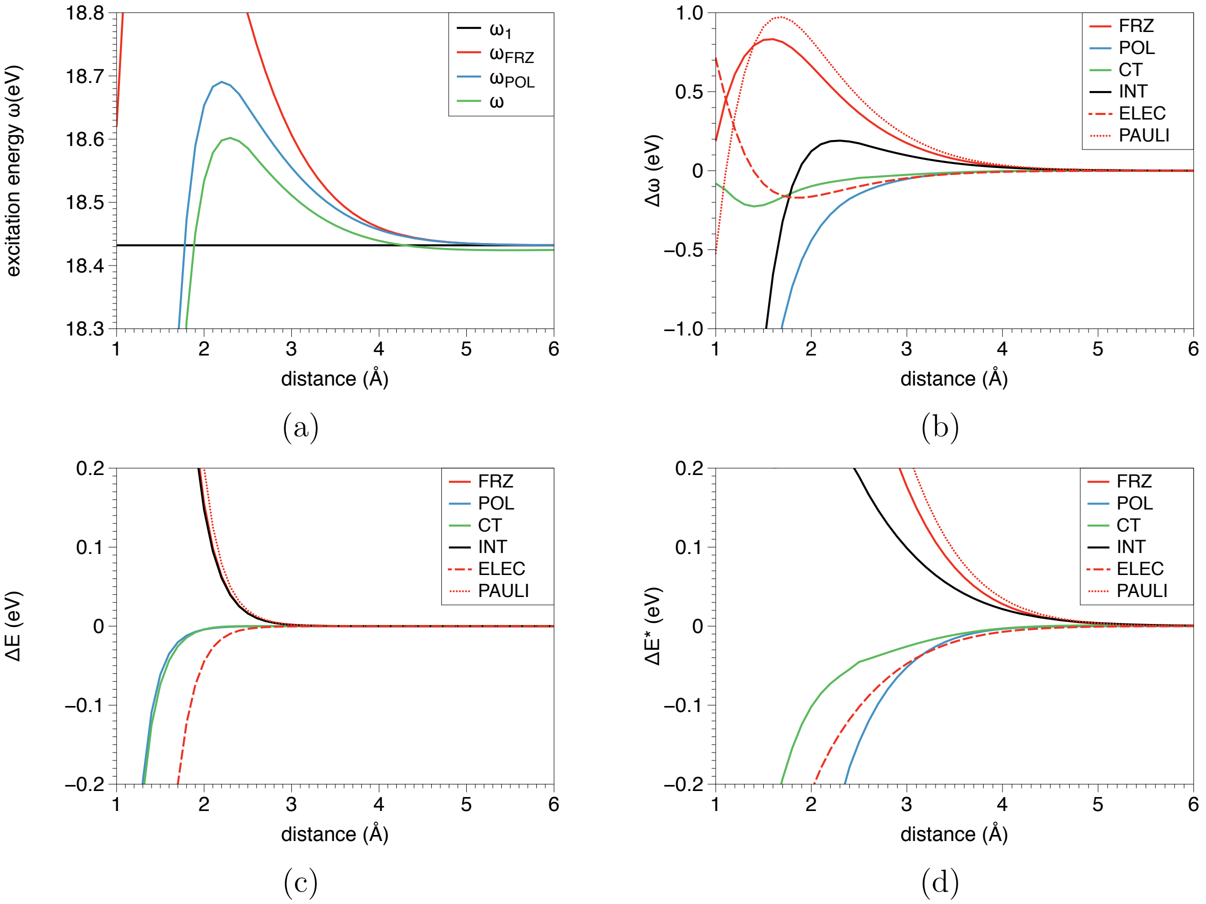

Figure 4.5: EDA results for the Ne-He dimer (in eV): (a) Excitation energies evaluated at different EDA levels; (b), (c), (d): Decomposition of the shifts in excitation energies ($\Delta\omega$), ground state interaction energies (ΔE), and first excited state interaction energies (ΔE^*), respectively.

on the excitation energies of NeHe_N clusters, with one neon atom placed at the center and varying numbers of helium atoms around (see Figure 4.6 for configurations). Every single atom is treated as an individual fragment in these calculations. As shown in Figure 4.7, the blue shift of excitation energy comes from the Pauli repulsion term (the other terms are all negative). This is the main reason for a bulk state to be more blue-shifted than a surface state. In addition, the Pauli repulsion is roughly proportional to the number of helium atoms when N goes from 1 to 6. However, adding a second layer of 8 helium atoms ($N = 14$) barely charges the EDA result, as the interaction between the central neon and the second layer of helium atoms is very weak (the Pauli term decays exponentially with intermolecular distance).

Finally, with some caution, we can also investigate the interaction between two helium atoms. As the two fragments are now identical, the excitation can reside on either helium when the fragments are isolated, so there are two degenerate reference states with excitation

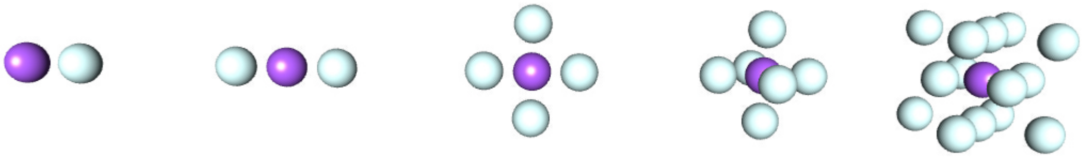

Figure 4.6: Structures of the $NeHe_N$ clusters, where N = 1, 2 (linear), 4 (square), 6 (octahedron), 14 (face-centered cubic). The distances between the center neon and the first layer of helium atoms are 3.43 Å, which comes from a ground state geometry optimization of the Ne-He dimer at the MP2/6-311(2+)G level.

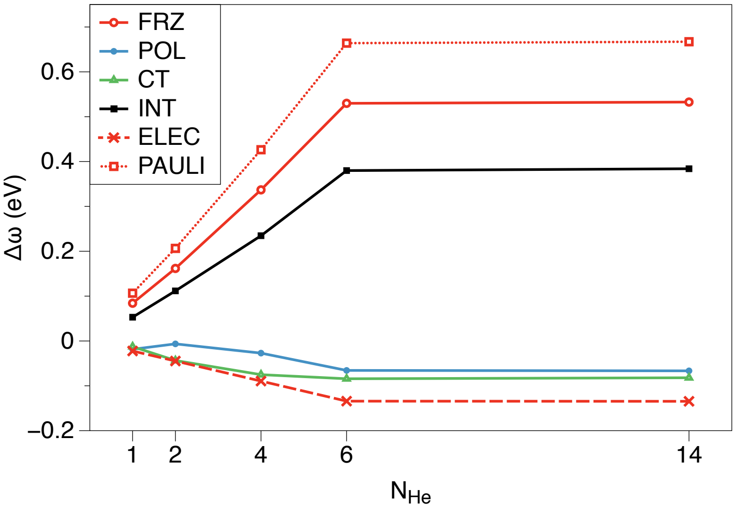

Figure 4.7: Decomposition of the shifts in Ne's $2p \rightarrow 3s$ excitation energy (in eV) in $NeHe_N$ with varying numbers of helium atoms.

energy ω_0. We can use either as the reference, in the current EDA scheme, and they will yield degenerate frozen energies also. Note that one could break the degeneracy at the frozen level through the configuration interaction between these degenerate references (excitons). The effect of this "excitonic splitting" will be discussed in a future publication, but for now, it is included in the polarization term.

Keeping that in mind, we examine the potential energy curves for the helium dimer. The decomposition of excitation energies resembles the neon-helium system, but He-He has stronger polarization (more negative) and weaker Pauli repulsion (less positive), such that that the excitation energy is less blue-shifted at $\sim$ 3 Å and more red-shifted at small distances (Figures 4.8(a) and 4.8(b)). The interaction in the ground state is also less unfavorable for the helium dimer (Figure 4.8(c)). As a result of all these factors, the excited helium dimer is bound at small distances (Figure 4.8(d)), while the interaction between an excited neon

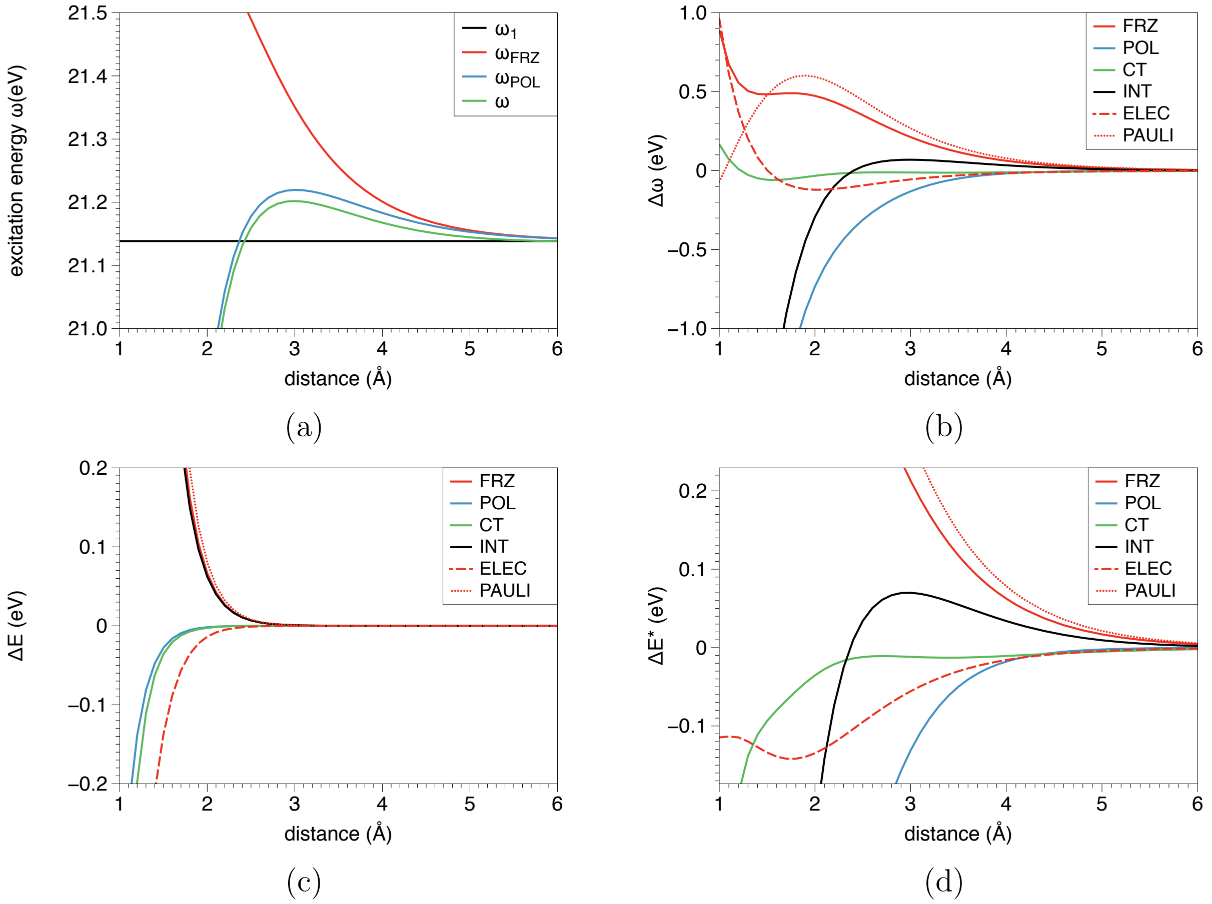

(a)

(b)

(c)

(d)

Figure 4.8: EDA results for the helium dimer (in eV): (a) Excitation energies evaluated at different EDA levels; (b), (c), (d): Decomposition of the shifts in excitation energies ($\Delta\omega$), ground state interaction energies (ΔE), and first excited state interaction energies (ΔE^*), respectively.

atom and a ground state helium atom is always unbound (Figure 4.5(d)). We also remind the reader that dispersion interactions are neglected in CIS theory: they would provide a small amount of additional binding in all states.

4.3.3 Formamide-water

Formamide is the simplest molecule that contains peptide linkage. The first excited state of formamide is known as an $n{\to}\pi^*$ excitation[197]. Experimental studies have shown that in aqueous solutions, the $n{\to}\pi^*$ transition is blue-shifted by 0.27 eV compared to the gas phase result[198, 199]. Gordon and co-workers performed a theoretical study using CIS on the formamide-water complexes with 1–3 water molecules and observed blue-shifted excitation energies in all calculations[200]. With one water, they identified two possible configurations with different hydrogen-bond structures (shown in Figure 4.9), where the (a) configuration

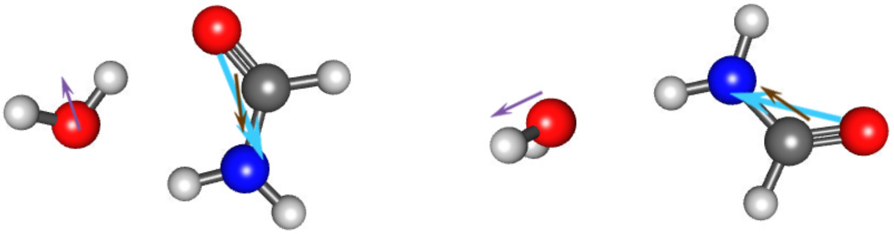
(a) (b)

Figure 4.9: Two configurations of the formamide-water complex. The geometries are optimized with MP2/6-311++G(2d,2p), as in Ref. 200. The ground and excited state dipole moments of formamide are indicated by blue and brown arrows, respectively, and the dipole moments of water are shown by purple arrows.

Table 4.1: EDA results for the formamide-water complex (in eV), including the decomposition of interaction energies in the ground state (ΔE) and the $n \rightarrow \pi^*$ excited state (ΔE^*), as well as the shifts in excitation energies ($\Delta\omega$).

	(a)					(b)				
	FRZ	(ELEC/PAULI)	POL	CT	INT	FRZ	(ELEC/PAULI)	POL	CT	INT
ΔE	-0.068	-0.758/0.691	-0.154	-0.085	-0.306	-0.087	-0.338/0.251	-0.056	-0.029	-0.172
ΔE^*	0.470	-0.353/0.823	-0.108	-0.318	0.045	-0.040	-0.297/0.257	-0.054	-0.036	-0.130
$\Delta\omega$	0.538	0.406/0.133	0.046	-0.233	0.351	0.047	0.041/0.006	0.002	-0.007	0.042

is lower in energy and has a larger blue shift than (b).

Our EDA results in Table 4.1 indicate that the main reason for the blue shifts in both configurations is the frozen interaction, where electrostatics and Pauli repulsion both favor the ground state. It is reasonable that the excited state is subject to stronger Pauli repulsion, as the electronic density is typically more diffuse after excitation. The electrostatic interaction is less favorable in the excited state because when the lone pair electron is promoted to the empty π^* orbital, the carbonyl oxygen is not as negatively charged as in the ground state. To better understand the change in electrostatics, we first look at the dipole moments of water and formamide. In Figure 4.9, we can see that the direction of formamide's dipole moment barely changes after excitation, while its magnitude is significantly reduced. This could result in a less favorable dipole-dipole interaction in the excited state for both configurations.

However, further investigation shows that only looking at the dipole-dipole interaction is probably not enough. In Table 4.2, we report the electrostatic interaction energies calculated

Table 4.2: Comparison between the classical electrostatic terms given by our EDA scheme and results of multipole expansion (up to quadrupole moments) for the formamide-water system (with configurations (a) and (b) shown in Figure 4.9). "d" in subscripts represents dipoles and "q" is for quadrupoles. The energies are reported in eV.

	(a)				(b)			
	distance (Å)	ΔE_{ELEC}	ΔE_{dd}	$\Delta E_{\mathrm{dd+dq+qq}}$	distance (Å)	ΔE_{ELEC}	ΔE_{dd}	$\Delta E_{\mathrm{dd+dq+qq}}$
ground state	2.7	-0.758	-0.240	-0.219	4.2	-0.338	-0.118	-0.154
	10.1	-0.005	-0.004	-0.005	10.2	-0.010	-0.009	-0.010
excited state	2.8	-0.353	-0.098	0.002	4.0	-0.296	-0.067	-0.107
	10.3	-0.002	-0.002	-0.002	10.0	-0.006	-0.004	-0.005

with a multipole expansion. When we pull the two fragments apart, making the distance between the charge centers of water and formamide $\sim$ 10 Å, the Coulomb interaction evaluated by multipole expansion, truncated at the quadrupole-quadrupole level, recovers the classical electrostatics pretty well. However, at the equilibrium distance in (a) and (b), the multipole expansion energy is a very poor approximation to the classical electrostatic term. This fact suggests that at short distance, there is a non-negligible charge penetration effect due to the overlap of monomer densities, which makes the electrostatic interaction more favorable. Only at long distance, can one safely employ the multipole interaction picture to interpret electrostatics.

Gordon *et al.* used the relative orbital energies of HOMO and LUMO to explain the origin of the blue shift[200]. Here, in Table 4.3, we report the orbital energies of the dominant pair of natural transition orbitals (NTOs) (evaluated as $\langle\psi_{NTO}|\hat{F}|\psi_{NTO}\rangle$). The orbital energies of both occupied and virtual NTOs in configuration (a) are red-shifted from monomer to complex, and the occupied has a larger shift so the orbital energy difference is enlarged, which agrees with the picture discussed in Gordon's work. However, for the configuration (b), although we also observe the blue shifts in both occupied and virtual NTO energies, the orbital energy difference is red-shifted, which is opposed to the shift in the excitation energy. Moreover, the orbital energy difference of the NTO pairs is around 17 eV, which is much larger than the excitation energies ($\sim$6.5 eV). On the other hand, we can consider looking at the excitation energy of a singly excited wavefunction Ψ_s where the transition takes place between the dominant NTO pair: $\omega_s = \langle\Psi_s|\hat{H}|\Psi_s\rangle - E_{HF}$. We find that ω_s recovers the CIS excitation energy ω quite well, and has the correct blue-shifting behavior for both (a) and (b) configurations. This indicates that the excitation can be well described by a single orbital transition, but, in this case, the orbital energy difference is a poor approximation to the CIS excitation energy.

Finally, it is interesting to note that CT is more favorable for the excited state in configuration (a), i.e. $\Delta\omega_{\mathrm{CT}} < 0$. This seems to be counterintuitive, as in (a), the $n\rightarrow\pi^*$ excitation

Table 4.3: NTO analysis for the formamide-water complex. The orbital energies of the dominant occupied-virtual NTO pair for the $n{\rightarrow}\pi^*$ excitation and the gap between them ($\Delta\epsilon$) are reported, as well as the excitation energies estimated using the dominant natural transition (ω_s).

	(a)					(b)				
	$\epsilon_{\text{NTO}}^{\textbf{(occ)}}$ (a.u.)	$\epsilon_{\text{NTO}}^{\textbf{(virt)}}$ (a.u.)	$\Delta\epsilon$ (eV)	ω_s (eV)	ω (eV)	$\epsilon_{\text{NTO}}^{\textbf{(occ)}}$ (a.u.)	$\epsilon_{\text{NTO}}^{\textbf{(virt)}}$ (a.u.)	$\Delta\epsilon$ (eV)	ω_s (eV)	ω (eV)
monomer	-0.437	0.187	16.992	6.537	6.448	-0.438	0.188	17.049	6.585	6.493
complex	-0.450	0.180	17.131	6.899	6.799	-0.422	0.203	17.002	6.629	6.536

renders the carbonyl oxygen less negatively charged, so one would expect weaker charge transfer than in the ground state. However, it may be problematic to relate the magnitude of CT energy lowering to the net charge flow between fragments. In some symmetric systems such as He_2, although there is no net charge transfer in both ground and excited states, CIS has lower excitation energy than ALMO-CIS, which is a result of allowing CT from the occupied orbitals of one fragment to the virtuals of the other. From another perspective, the CT energy lowering in the ground state comes from removing the constraints on MOs (MOs no longer have to be block-diagonal), while in the excited state, both MOs and CIS amplitudes are relaxed (the amplitude corresponding to interfragment excitations can be non-zero). The additional variational degree of freedom in the CIS wavefunction is the main reason for CT usually causing a red shift in excitation energy.

4.3.4 Pyridine-water and pyrimidine-water

Hydrogen bonds between heteroaromatic rings such as pyridine and diazines and water are of great interest because of their roles in biological systems[201–203]. Typical geometric configurations include a linear hydrogen bond configuration and an "on-top" configuration where H_2O interacts with the π system (see Figure. 4.10 for illustration of these two configurations). A previous study[195] showed that the linear structure is more stable in the ground state of both pyridine and diazines. However, for the excited state, pyridine is more stable with the on-top structure while the linear one is still preferred for pyridazine and pyrimidine. In order to gain more insight into this interesting fact, we perform EDA with the ωB97X-D functional on the pyridine-water and pyrimidine-water complexes, using the geometries given in the supporting information of Ref. 195, which are optimized for the first excited state ($n{\rightarrow}\pi^*$) at the TDDFT ωB97X-D/6-311++G(d,p) level of theory. All data are collected in Table B.1. The results of EDA with CIS, using the same geometries are also presented in the supporting information (Table S1) for comparison.

Our results show that upon excitation, the interaction between pyridine/pyrimidine and water becomes weaker in the linear structure but stronger in the top structure. Further decomposition shows that this is mainly an electrostatic effect. This is reasonable since we can imagine that during an $n{\rightarrow}\pi^*$ excitation, the electronic density of nitrogen's lone pair

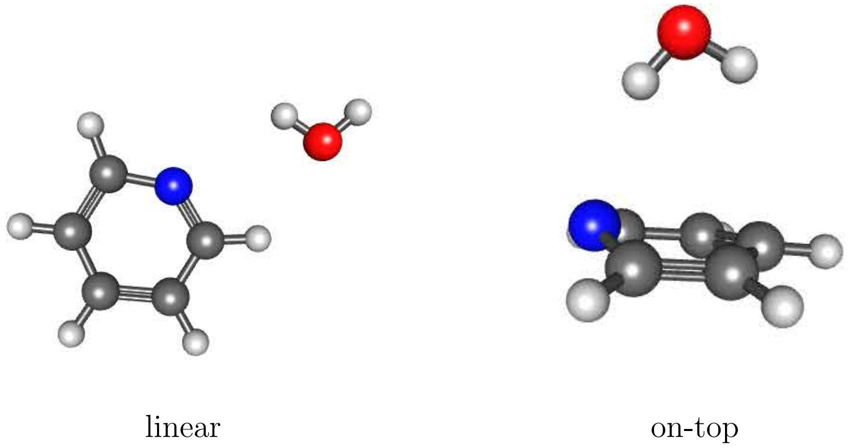

Figure 4.10: The linear and on-top configuration for the pyridine-water complexes.

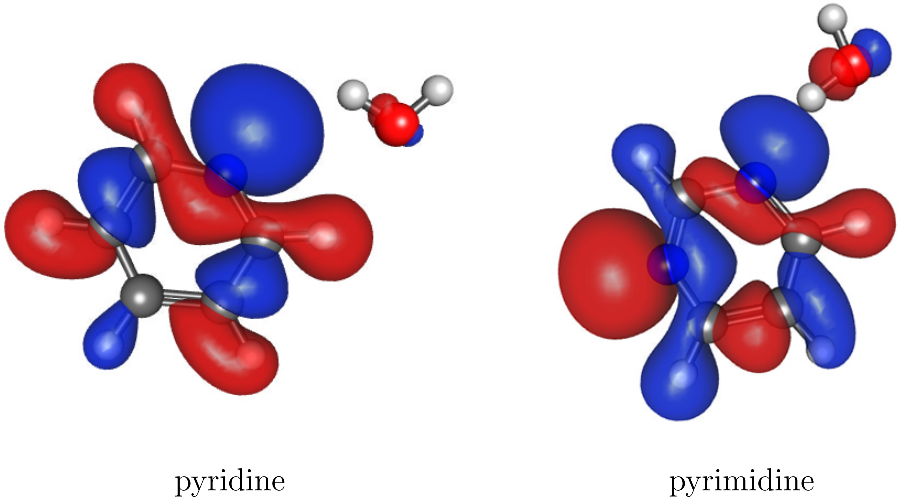

Figure 4.11: The dominant occupied NTOs for the $n \rightarrow \pi^*$ excited states of the pyridine- and pyrimidine-water complexes in linear configuration.

will move towards the π system, which weakens the hydrogen bond in the linear structure but strengthens the interaction between water and the heteroaromatic ring in the on-top configuration. For pyrimidine, the linear structure is much more stable than the on-top one in the ground state (0.3184 eV vs. 0.1455 eV for the binding energy), so the above-mentioned effect does not reverse the order of stability for these two configurations in their excited states. However, in the excited state of pyridine, the on-top configuration becomes more favorable. All these are consistent with the findings in Ref. 195.

It is also interesting that for the linear structures, CT results in a much smaller energy lowering in pyridine than in pyrimidine, for both ground and excited states. A closer look at the optimal geometries of these exciplexes can help us understand why. For pyrimidine-water, the N–H–O angle is 161°, while for pyridine-water this angle is much smaller (113°). An N–H–O angle that is far away from 180° indicates that the hydrogen bond is likely broken in pyridine-water's excited state. For pyrimidine, however, the non-bonding orbitals on both nitrogen atoms can contribute to the $n{\rightarrow}\pi^*$ transition, so the linearity of the hydrogen bond is less affected. The dominant occupied NTOs for the $n{\rightarrow}\pi^*$ excited states of both pyridine and pyrimidine (shown in Figure 4.11) support this assumption, as the non-H-bonded nitrogen atom in pyrimidine is significantly involved in forming the occupied NTO. As a further investigation, we also perform EDAs on the linear structures optimized in the ground state. The resulting structures show typical hydrogen-bonding characters, as the N–H–O angles are 163° and 153° for pyridine and pyrimidine, respectively. With these structures, the energy lowering due to CT for these two complexes becomes more comparable, as shown in Table B.1.

4.3.5 Halide-water

The final system is a challenging example for our current EDA scheme. Halide anions have bound excited states in solution but not in gas phase, which is due to the charge transfer to solvent (CTTS) effect that stabilizes the promoted electron. There have been various studies on the excited states of small halide-water clusters $X^-(H_2O)_N$, and the role of CTTS has been discussed[42–47]. Kim et al.[47] reported TDDFT and CIS excitation energies for X = F, Cl, Br, I and $N = 1$–4. They observed a blue shift in excitation energies when N increases. By examining the amount of charge transfer upon excitation (measured as the change in Mulliken population on X^-), they also pointed out that the CTTS effect is minimal for F^- but significant for Cl^-, Br^- and I^-.

We obtained geometries of $F^-(H_2O)_N$ and $Cl^-(H_2O)_N$ with $N = 1$–4, which are similar to the ones Kim *et al.* used in their studies (see Figure 4.12). Starting from the simplest $N = 1$ case, we first look at the attachment and detachment density at the ALMO-CIS and CIS level (Figure 4.13). For $F^-(H_2O)$, the excitation is mainly located on water. The main difference between ALMO-CIS and CIS is that the CIS detachment density has some small values on F^-. These are consistent with the conclusion in Ref. 47 that charge transfer in $F^-(H_2O)_N$ is small. For $Cl^-(H_2O)$, the detachment density looks similar in ALMO-CIS and CIS. However, when CT is allowed, the attachment density migrates from the vicinity of Cl^- to that of water. Based on the different character of excited states in $F^-(H_2O)_N$ and $Cl^-(H_2O)_N$, we made different choices for the fragment to excite at the isolated fragment level. For $F^-(H_2O)_N$, the waters are excited, which means ω_1 is the excitation energy of the water cluster evaluated in isolation (note: in our calculations for halide-water clusters, all the water molecules are treated as one single fragment). For $Cl^-(H_2O)_N$, the reference contains excited Cl^- and ground state waters. However, as Cl^- has no bound excited state, we take its ionization energy estimated by the HOMO energy of Cl^- as ω_1, which would be the "excitation energy" of a CIS calculation with the virtual being a free electron. To avoid

Table 4.4: EDA results for the pyridine- and pyrimidine-water complexes using the ωB97X-D functional. Presented data (in eV) include the decomposition of interaction energies in the ground state (ΔE) and the $n\rightarrow\pi^*$ excited state (ΔE^*), as well as the shifts in excitation energies ($\Delta\omega$). "gs" denotes that geometries optimized in the ground state are used.

pyridine-water

		FRZ	(ELEC/PAULI)	POL	CT	INT
linear($n\rightarrow\pi^*$)	ΔE	-0.140	-0.204/0.064	-0.024	-0.020	-0.184
	ΔE^*	-0.047	-0.126/0.079	-0.008	-0.047	-0.101
	$\Delta\omega$	0.093	0.078/0.015	0.017	-0.027	0.083
top($n\rightarrow\pi^*$)	ΔE	-0.077	-0.155/0.078	-0.032	-0.048	-0.157
	ΔE^*	-0.131	-0.249/0.117	-0.034	-0.054	-0.220
	$\Delta\omega$	-0.054	-0.094/0.039	-0.002	-0.007	-0.063
linear(gs)	ΔE	-0.120	-0.519/0.399	-0.079	-0.120	-0.319
	ΔE^*	0.394	-0.105/0.499	-0.022	-0.408	-0.036
	$\Delta\omega$	0.514	0.414/0.100	0.057	-0.288	0.283

pyrimidine-water

		FRZ	(ELEC/PAULI)	POL	CT	INT
linear($n\rightarrow\pi^*$)	ΔE	-0.122	-0.530/0.408	-0.078	-0.119	-0.318
	ΔE^*	0.060	-0.399/0.459	-0.104	-0.216	-0.259
	$\Delta\omega$	0.182	0.131/0.052	-0.026	-0.097	0.059
top($n\rightarrow\pi^*$)	ΔE	-0.052	-0.210/0.159	-0.035	-0.059	-0.146
	ΔE^*	-0.072	-0.254/0.182	-0.038	-0.077	-0.187
	$\Delta\omega$	-0.020	-0.044/0.024	-0.003	-0.018	-0.041
linear(gs)	ΔE	-0.128	-0.470/0.342	-0.066	-0.101	-0.296
	ΔE^*	0.164	-0.226/0.182	-0.095	-0.213	-0.144
	$\Delta\omega$	0.292	0.244/-0.160	-0.029	-0.112	0.152

the complexity of redefining ω_{FRZ}, the electrostatics, Pauli repulsion and polarization terms

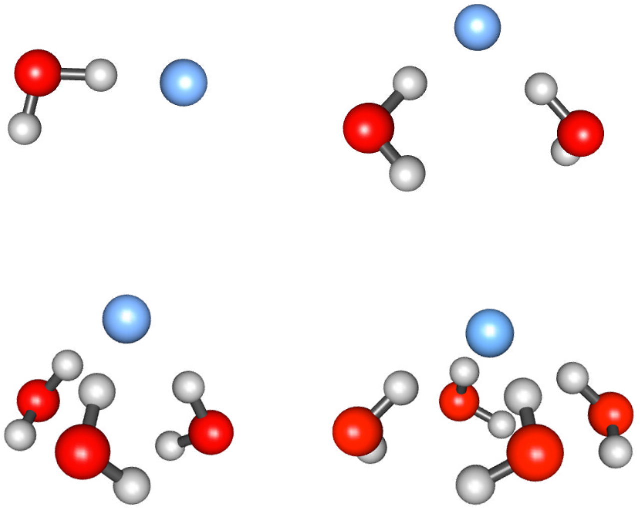

Figure 4.12: Illustration of the structures for $X^-(H_2O)_N$ ($N = 1, 2, 3, 4$). $N = 1$ has the typical linear hydrogen bond geometry, while $N = 2, 3, 4$ have C_2-, C_3-, C_4-like symmetries.

are combined into a single non-CT term by taking the difference between the ALMO-CIS excitation energy and ω_1.

Figure 4.14 shows the excitation energies at different EDA levels, and Table 4.5 summarizes the EDA results for the shifts in excitation energies. For $F^-(H_2O)_N$, it is surprising to see a Pauli repulsion as large as $\sim$ 10 eV. To understand this, we note that there is a significant difference between the attachment density of isolated water and that of $F^-(H_2O)$ (Figure 4.13). It is clear that the excited electron would experience a strong Pauli repulsion from the electronic density around F^-, and the repulsion would be relieved when the system is allowed to polarize. In spite of this, we have reservations about the very large value of the Pauli terms. The effect of other terms decrease as N increases, indicating that the excitation is approaching the bulk limit of pure water. As for $Cl^-(H_2O)_N$, we do observe a relatively large contribution from CT, and its effect on the excitation energy becomes smaller for larger clusters. For both $F^-(H_2O)_N$ and $Cl^-(H_2O)_N$, the excitation energy is blue-shifted when the number of water molecules increases, which is primarily due to the growing magnitude of the unfavorable non-CT effect.

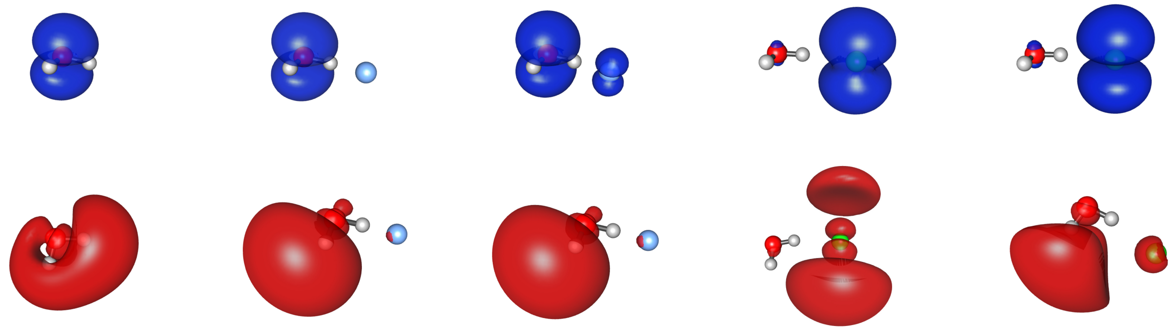

H_2O (CIS) F^-H_2O (ALMO-CIS) F^-H_2O (CIS) Cl^-H_2O (ALMO-CIS) Cl^-H_2O (CIS)

Figure 4.13: Attachment (red) and detachment (blue) densities for the first excited states of an isolated water molecule and the $F^-(H_2O)$, $Cl^-(H_2O)$ complexes. For the latter two complexes, the results of both ALMO-CIS and standard CIS are plotted.

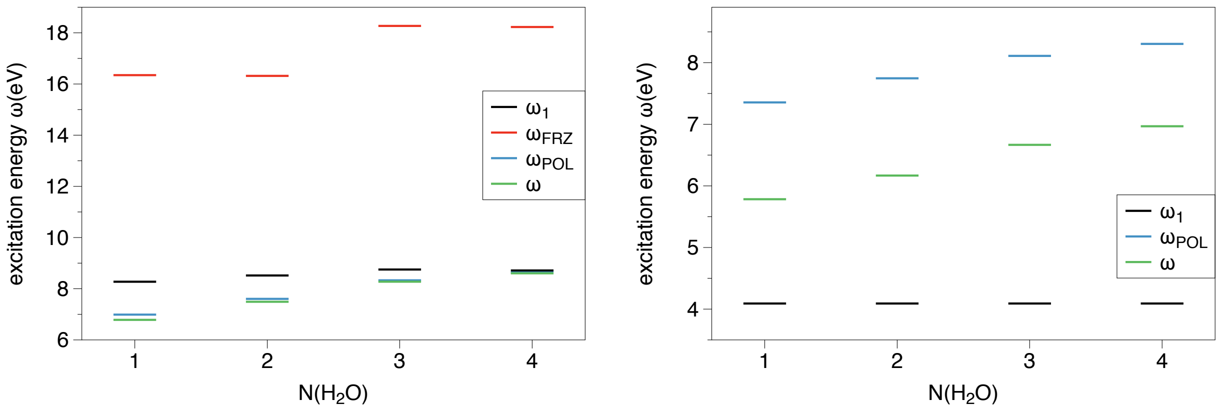

(a) $F^-(H2O)_N$ (b) $Cl^-(H2O)_N$

Figure 4.14: Excitation energies (in eV) for $F^-(H2O)_N$ (a) and $Cl^-(H2O)_N$ (b) computed at different EDA levels. Note that ω_1 is given by the first excitation energy of the water molecules for the former system, while the HOMO energy of Cl^- is used for the latter so that it does not vary with N.

Table 4.5: EDA results (in eV) for the shifts in the lowest excitation energies ($\Delta\omega$) of the $F^-(H_2O)_N$ (a) and $Cl^-(H_2O)_N$ (b) systems.

N	FRZ	(ELEC/PAULI)	POL	CT	INT
1	8.072	-0.803/8.875	-9.358	-0.203	-1.489
2	7.800	-0.746/8.545	-8.714	-0.112	-1.026
3	9.519	-0.745/10.264	-9.941	-0.052	-0.474
4	9.514	-0.709/10.223	-9.595	-0.0265	-0.108

(a) $F^-(H2O)_N$

N	NON-CT(FRZ+POL)	CT	INT
1	3.264	-1.572	1.693
2	3.656	-1.579	2.077
3	4.019	-1.444	2.575
4	4.214	-1.337	2.877

(b) $Cl^-(H2O)_N$

4.4 Conclusion and outlook

In the present paper, we have proposed an EDA scheme for intermolecular interactions that involve molecules in their excited states (i.e. exciplexes). In the spirit of the ground state ALMO-EDA, the energy partitioning is achieved by evaluating the excitation energy of the intermolecular complex at the frozen, polarized, and fully relaxed levels of linear response theory (using CIS as an example in the text below, but equally applicable to TDDFT). These intermediate states are defined by application of constraints to both the MOs and the CI coefficients (CIS amplitudes). The procedure is initiated with the evaluation of a target excited state on a specific isolated fragment. The frozen state is then constructed by embedding this electronically excited fragment into an environment described by ground state fragments with unrelaxed MOs.

The definition of the polarized state, on the other hand, takes advantage of the ALMO-CIS scheme we have previously developed.[102] In ALMO-CIS, the intrafragment relaxation of MOs due to the presence of other fragments is accounted for at the ground state level (via the SCF-MI approach), while the corresponding excited state of the supersystem, constructed as a superposition of intrafragment excitations, is computed based upon these absolutely localized orbitals. This polarized excited state relaxes the amplitudes on the excited fragment, and also permits the excitation to spread to other fragments (though without charge transfer). Finally, the fully relaxed state is given by a standard CIS calculation for the entire system. The differences between the excitation energies evaluated at these intermediate levels (including the initial and the final) define the frozen, polarization, and charge transfer contributions to the shift in excitation energy of this specific fragment due to its interaction with the other molecules in the environment.

This method, to our knowledge, is the first EDA scheme designed for fully *ab initio* intermolecular interactions that involve a molecular complex in an excited state. It is most suitable for scenarios where the complex excitation is reasonably well-localized to a single fragment. In such cases, it reports on the modulation of molecular excited states by the surrounding environment. Illustrated by the proof-of-concept applications, useful insights on changes in excitation energies induced by intermolecular interactions are obtained by using this EDA method. For example, from the study of the NeHe_N clusters, we find that Pauli interaction between the excited neon and the ground state helium atoms is responsible for the blue shift in neon's $2p \to 3s$ excitation (when the Ne–He distances are greater than 2 Å); and for a hydrogen-bonding system such as the formamide-water complex, the diminished permanent electrostatics associated with the $n \to \pi^*$ transition turns out to be the primary reason for the blue shift in the corresponding excitation energy.

As a first effort to extend EDA schemes to intermolecular interactions involving molecules in their excited states, our method still has several limitations. (i) Total energies of excited states are not fully variational (MOs optimized in the ground state are employed for excited states). Therefore, the negative semi-definite terms in the ground state ALMO-EDA (polarization and CT) are indefinite for the exciplex (see Sec. 5.2). Although this rarely occurs in practice, a scheme that ensures these terms are negative semi-definiteness would be preferable. (ii) Our method is most appropriate for exciplexes where most excitation amplitude belongs to one fragment and connects to an excited state of that fragment in isolation. However, sometimes the fragment excited state does not exist in isolation (e.g. CTTS excitation of $\mathrm{Cl}^-(\mathrm{H_2O})_N$). In other cases, the excited state may strongly couple with excitations in the environment that are close in energy (e.g. the exciton splitting effect mentioned in Sec. 4.3.2. (iii) The present EDA method can only handle one single excited fragment at separation, so cases involving multiple excited fragments would be an interesting future extension.

Chapter 5

Energy Decomposition Analysis for Excimers

5.1 Introduction

Excimers are excited dimers that, while weakly bound in the ground state, are much more strongly interacting in the electronic excited state. In fluorescence spectra, excimer emission typically appears as a broad, structureless band at lower energy than the structured molecular band. One well-known example of excimers occurs in the noble gas dimers[204]. He_2^* was the first singlet excimer to be identified though fluorescence spectra[205]. It can be thought of as a He_2^+ core (with bond order 1/2), and an outer Rydberg electron. An intense continuum between 60 nm and 100 nm was attributed to the transition from He_2^* to the dissociated ground state (He + He). Other noble gases excimers (Ne_2^*, Ar_2^*, Kr_2^*) were subsequently discovered[206–208]. Aromatic molecules can also form excimers in solution, as well as in neat liquid, molecular crystals and polymers [204]. The most stable excimer structure is usually perfectly stacked, consisting of a symmetric pair of parallel molecules. The pyrene dimer was the first experimentally studied aromatic system[209], and its fluorescence quenching has been used as an effective analytical tool[210–214].

There are two main types of configuration interaction (CI) which can contribute to excimer formation: (1) exciton resonance (ER) caused by interaction between localized excited states ($A^*B \leftrightarrow AB^*$), where the electron and hole are placed on the same molecule. (2) charge resonance (CR) due to interaction between charge transfer states ($A^+B^- \leftrightarrow A^-B^+$). The excimer states originate from a mixture of ER and CR states, and simplified models of excimer formation based only on ER or CR may not properly explain some experimental results[204]. The Frenkel-Davydov exciton model[177, 178], for example, only gives rise to pure ER states as its wavefunction is constructed in the basis of neutral excitations:

$$|\Phi\rangle = c_A|\Psi_A^*\Psi_B\rangle + c_B|\Psi_A\Psi_B^*\rangle \tag{5.1}$$

and the coefficient c_A and c_B are solved from the corresponding secular equation. The off-diagonal term $\langle\Psi_A^*\Psi_B|\hat{H}|\Psi_A\Psi_B^*\rangle$, coming from the coupling between localized excitations, are sometimes estimated as Coulomb integrals over transition densities[215] or simply within a dipole approximation. This will tend to be inaccurate at short separations. *Ab initio* implementation of the Frenkel exciton model, which takes account of exact exchange and the overlap between localized states was recently proposed by Herbert and coworkers[92]. In order to study systems where charge-transfer (CT) plays an important role, efforts have been made to go beyond the Frenkel exciton model, often by expanding the basis space for CI to include charge-transfer basis states[216, 217].

The formation of excimers can also be viewed from the perspective of intermolecular interactions. Energy decomposition analysis (EDA) is a powerful tool to study intermolecular interactions[218, 219]. An EDA decomposes the total interaction energy into several interpretable components, such as electrostatics, Pauli repulsion, dispersion, polarization and charge transfer, thereby allowing an assessment of their relative importance. Many EDA schemes have been proposed and used for studying intermolecular interactions between ground state molecules, [49–70, 101, 189, 190] and we believe that a suitably designed EDA can also help in understanding the relative roles of the different driving forces that given rise to excimers. For example, it would be very useful to distinguish the comparative magnitude of the ER and CR effects mentioned above. It should be mentioned that many wavefunction analysis schemes have been proposed to quantify the ER and/or CR characters of excited states using quantities related to the transition or difference density matrix. [220–226] Nonetheless, these “top-down” analysis schemes focus more on the composition and general character of an excited state wavefunction rather than the energy components that lead to the formation of an excimer. In broader terms, there is far greater chemical understanding of intermolecular interactions in the ground state of complexes than those in excited states, and therefore a well-posed EDA for excited states can be even more valuable than one for ground states. One reason for this is that monomer properties such as polarizabilities and Lewis acidity or basicity can be drastically different in excited states, and another reason is that the exciton resonance effect is unfamiliar from ground states.

There are very few reported EDA approaches for unraveling the electronic structure of complexes in excited states. Recently, we proposed an EDA scheme for understanding intermolecular interactions involving excited molecules.[72] This EDA was formulated in the framework of linear response theory for single excitations (e.g. configuration interaction singles (CIS)[9, 10] and time-dependent density functional theory (TDDFT)[9, 31–33] within the Tamm-Dancoff approximation (TDA)[34]) and utilized absolutely localized molecular orbitals (ALMOs) [95, 99] to define the intermediate (frozen and polarized) states. The formulation of that method assumes that one of the fragments has an excitation energy considerably lower than the other fragments, so the excitation can be assigned to a single molecule within a complex (i.e. exciplexes). This assumption is appropriate for cases such as solvated chromophores, but not for excimer systems.

In this work, we take up the challenge of generalizing the previously proposed EDA scheme for exciplexes to treat excimers. Briefly speaking, in the exciplex EDA, the shift in excitation energy when an excited molecule interacts with the environment was separated into three terms: frozen (FRZ), polarization(POL) and charge transfer(CT), and each term was then added to its counterparts obtained from the original ground state ALMO-EDA[68, 69]. Here, we will introduce a new term which we call excitonic-splitting (EXSP) to account for the coupling between local excitations (i.e. the ER effect). Details of the excimer EDA formulation are presented in Sec. 5.2. In Sec. 5.3, we apply the new EDA scheme to several representative examples, including the noble gas and aromatic excimers.

5.2 Theory

The new EDA scheme employed in this paper is closely related to the ALMO-EDA for exciplexes that we proposed recently.[72] The two schemes share the same definition for the frozen and polarized states. Therefore, we will first review our previous scheme but carefully write down the derivation for multiple states, as at least two states are considered in excimer systems. Then we introduce the excitonic splitting term and the excitonic coupling intermediate state, which are important for excimers. Finally we propose a state tracking approach that is essential for connecting the initial fragment-localized states to the final delocalized excited states of the complex.

In this section and the rest of this paper, molecular orbitals are denoted by lowercase letters i, j (occupied) and a, b (virtual). Capital letters I, J are used as subscript indicate fragments indexes. The state indexes are denoted in the superscript: s, t for fragment states, κ, κ' for supersystem states, "$*$" for a generic excited state and superscripts are often dropped in the case of a ground state. In Sec. 5.3, we also use symbols for irreducible representations to specify excited states based on the symmetry of molecular wavefunctions.

5.2.1 Review of ALMO-EDA for exciplexes

By definition, the interaction energy is the counterpoise (CP)-corrected [**boys1970calculation**] difference between the excited supersystem energy E^* and the sum of isolated fragment energies, E^*_{frag}:

$$\Delta E^*_{\text{INT}} = E^* - E^*_{\text{frag}} + \Delta E_{\text{BSSE}} \tag{5.2}$$

where the last term represents the basis set superposition error (BSSE). When the excitation of interest is mainly localized on one fragment (assuming it is fragment 1 without loss of generality), E^*_{frag} is defined as the sum of excited state energy of fragment 1 and ground state energies of other fragments. Equivalently, this is equal to the sum of ground state energies for all fragments and ω_1, the excitation energy of fragment 1 in isolation.

$$E^*_{\text{frag}} = E^*_1 + \sum_{J>1}^{N} E_J = \sum_{J=1}^{N} E_J + \omega_1 \tag{5.3}$$

Let us turn to systems composed of identical fragments. Assume there are M excitations of the isolated fragments that are close in energy. This will typically be one excitation per fragment if the fragments are identical, but can in principle involve more than one excited state per fragment. We can now define M different E_{frag}'s, each one corresponding to a particular excitation from the M degenerate excitations. For example, the κ^{th} reference energy, which corresponds to excited state s of fragment I is:

$$E^{\kappa}_{\text{frag}} = E^{s}_{I} + \sum_{J \neq I}^{N} E_J = \sum_{J}^{N} E_J + \omega^{s}_{I}$$

The M fragment excitations are likely to mix when the fragments interact, and form M supersystem excited states that are delocalized across fragments. Let us label these state energies as E^{κ}. While the local excitations are degenerate or near-degenerate, the supersystem states will usually split due to interaction, resulting in a range of different E^{κ} values.

To understand the effect of interaction, one needs to look at a set of M interaction energies, one for each resulting state: $\Delta E^{\kappa}_{\text{INT}} = E^{\kappa} - E^{\kappa}_{\text{frag}} + \Delta E^{\kappa}_{\text{BSSE}}$. For each such interaction energy, $\Delta E^{\kappa}_{\text{INT}}$, the contribution from the ground state interaction energy, ΔE_{INT} and the shift in excitation energy, $\Delta\omega_{\text{INT}}$, can be separated:

$$\Delta E^{\kappa}_{\text{INT}} = \Delta E_{\text{INT}} + \Delta\omega^{\kappa}_{\text{INT}} \tag{5.4}$$

where $\Delta E_{\text{INT}} = E - \sum_{I=1}^{N} E_I$, $\Delta\omega^{\kappa}_{\text{INT}} = \omega^{\kappa} - \omega^{s}_{I}$. Our exciplex EDA scheme[72] decomposes the excited cluster interaction energy into three terms, frozen (FRZ), polarization (POL) and charge transfer (CT). This is achieved by first defining the frozen and polarized wavefunction of excited states. Now, with the degeneracy between fragments present, we need to consider M frozen and polarization intermediate states, each defined in a similar way as before.

Polarized excited systems are described by the ALMO-CIS[102] wavefunction (or its TDDFT or TDDFT/TDA analog as appropriate), and E^{κ}_{POL} is given by the ALMO-CIS energy of state κ. The difference between E^{κ}_{POL} and E^{κ} results from the constraint in ALMO-CIS that the excitation can only take place between an occupied and a virtual orbital on the same fragment, and the ALMOs only contain contributions from the atomic orbital (AO) basis functions that reside on the given fragment. With these constraints, the ALMO-CIS states are intuitively CT-free (see the Appendix of ref. 71 for a proof). Thus the CT terms can be defined as:

$$\Delta E^{\kappa}_{\text{CT}} = E^{\kappa} - E^{\kappa}_{\text{POL}} + \Delta E^{\kappa}_{\text{BSSE}} \tag{5.5}$$

Recalling that in the ground state ALMO-EDA, SCF(MI) is used to compute the polarized system energy E_{POL}, the CT term can also be rewritten as:

$$\begin{aligned}\Delta E^{\kappa}_{\text{CT}} &= (E - E_{\text{POL}} + \Delta E_{\text{BSSE}}) \\ &\quad + (\omega^{\kappa} - \omega^{\kappa}_{\text{POL}} + \Delta E^{\kappa}_{\text{BSSE}} - \Delta E_{\text{BSSE}}) \\ &= \Delta E_{\text{CT}} + \Delta\omega^{\kappa}_{\text{CT}}\end{aligned} \tag{5.6}$$

In the frozen wavefunction, both amplitudes and orbitals are frozen. We compute the κ^{th} frozen excitation energy using the singles amplitudes of the isolated fragment, $t^{\kappa} \equiv t_I^s$:

$$\begin{aligned}\omega_{\mathrm{FRZ}}^{\kappa} = &\sum_{i,a,j,b\in I} \left(F_{ab} S_{ij} t_I^{s,ia} t_I^{s,jb} - F_{ij} S_{ab} t_I^{s,ia} t_I^{s,jb}\right) \\ &+ \sum_{i,a,j,b\in I} \langle \psi_i \psi_b || \psi_a \psi_j \rangle t_I^{s,ia} t_I^{s,jb} + 2 \sum_{i,a\in I} F_{ia} z_I^{s,ia}\end{aligned} \tag{5.7}$$

where $\mathbf{F}$ and $\mathbf{S}$ are the Fock and overlap matrices in the MO basis, respectively, and ψ's represent the MOs. The necessity of including the occupied-virtual block of the relaxed density of the isolated fragment (z_I) is discussed by Thirman *et al.* in the development of MP2-ALMO-EDA[101], as well as in our previous EDA scheme for exciplexes.[72] The frozen contribution to the excitation energies and the excited system energies are:

$$\begin{aligned}\Delta\omega_{\mathrm{FRZ}}^{\kappa} &= \omega_{\mathrm{FRZ}}^{\kappa} - \omega_I^s \\ \Delta E_{\mathrm{FRZ}}^{\kappa} &= \Delta E_{\mathrm{FRZ}} + \Delta\omega_{\mathrm{FRZ}}^{\kappa}\end{aligned} \tag{5.8}$$

Further decomposition of the frozen energy is also possible in ground state EDA.[188] A simple scheme (e.g. see ref. 227) is to use the "quasi-classical" definition for permanent electrostatics, and to classify the remainder of the frozen energy as Pauli repulsion:

$$\begin{aligned}&\Delta E_{\mathrm{ELEC}}^{\kappa} = \sum_{K<L} \int\int \mathrm{d}\mathbf{r}_1 \mathrm{d}\mathbf{r}_2 \rho_K^{\mathrm{tot}}(\mathbf{r}_1) r_{12}^{-1} \rho_L^{\mathrm{tot}}(\mathbf{r}_2) \\ &\text{with} \\ &\rho_K^{\mathrm{tot}} = \begin{cases} \rho_I^s(\mathbf{r}) + \rho_I^{\mathrm{nuc}}(\mathbf{r}) & K = I \\ \rho_K(\mathbf{r}) + \rho_K^{\mathrm{nuc}}(\mathbf{r}) & K \neq I \end{cases}\end{aligned} \tag{5.9}$$

and

$$\Delta E_{\mathrm{PAULI}}^{\kappa} = \Delta E_{\mathrm{FRZ}}^{\kappa} - \Delta E_{\mathrm{ELEC}}^{\kappa} \tag{5.10}$$

where ρ represents the ground state fragment electronic density, ρ_I^s is the s^{th} excited state electronic density of fragment I, and ρ^{nuc} and ρ^{tot} are the nuclear and total fragment charge densities, respectively. Defined in this way, the Pauli term will inevitably be contaminated by dispersion if the employed model chemistry incorporates long-range correlation effects (e.g. van der Waals density functionals).

5.2.2 Introducing the excitonic splitting term

Up to this point, the derivation largely follows the previous EDA scheme, except that the terms are now defined explicitly for each state. We will now introduce the main generalization needed in order to study the role of excitonic couplings, as are expected to be prevalent in systems with degenerate monomer excited states. Previously, any interaction energy difference between the frozen and polarized intermediate states was attributed to polarization effects. Now, as more than one fragment may make a significant contribution to the supersystem excitation, any coupling between these local excitations may break the degeneracy of the isolated monomer excitations. For identical fragments (and identical environment for each fragment), the frozen states are also degenerate, and the splitting due to configuration interaction between degenerate states will occur as soon as it is allowed (i.e. at the polarized level).

To separate the splitting effect due to “pure excitonic coupling” (i.e. the mixing of degenerate configurations) from polarization (i.e. changes in the on-fragment charge distributions due to the electrostatic environment), we propose a new EDA term, $\Delta\omega_{\mathrm{EXSP}}$, whose associated intermediate state has the form of a linear combination of the (degenerate) local excitations:

$$|\Phi_{\mathrm{EXSP}}\rangle = \sum_{\kappa}^{M} c^{\kappa} |\Psi_1 \Psi_2 ... \Psi_I^s ... \Psi_N\rangle \tag{5.11}$$

The coefficients $c^{\kappa} \equiv c_I^s$ and the corresponding excitonic-splitting excitation energies ω_{EXSP} are determined by solving the Schrödinger equation in the basis of the local excitations:

$$\mathcal{A}c = \omega_{\mathrm{EXSP}} \mathcal{G} c \tag{5.12}$$

The Hamiltonian $\mathcal{A}$ and metric $\mathcal{G}$ have dimension $M \times M$, with M being the total number of degenerate local excitations considered. This excitonic term is to be evaluated *before* the polarized intermediate state is considered.

The matrix elements are computed as:

$$\begin{aligned}
\mathcal{A}_{\kappa\kappa'} &= \langle \Psi_{\kappa} | \hat{H} - E_{\mathrm{FRZ}} | \Psi_{\kappa'} \rangle + \text{response} \\
&= \sum_{i,a \in I, j, b \in J} (F_{ab} S_{ij} t_I^{s,ia} t_J^{r,jb} - F_{ij} S_{ab} t_I^{s,ia} t_J^{r,jb}) \\
&\quad + \sum_{i,a \in I, j, b \in J} \langle \psi_i \psi_b || \psi_a \psi_j \rangle t_I^{s,ia} t_J^{r,jb} + \sum_{i,a \in I} F_{ia} z_I^{s,ia} \delta_{\kappa\kappa'} \\
\mathcal{G}_{\kappa\kappa'} &= \langle \Psi_{\kappa} | \Psi_{\kappa'} \rangle = \sum_{i,a \in I, j, b \in J} S_{ij} S_{ab} t_I^{s,ia} t_J^{r,jb}
\end{aligned}$$

Here, in general, index κ corresponds to state s on fragment I, and κ' corresponds to state r on fragment J. In the simple case of one degenerate state per fragment, κ reduces to simply be a fragment index. Note that the occupied orbitals are projected out of the virtual space, and the virtual orbitals are reorthogonalized within each fragment (as in Eq. 5.7). The response terms are added to the diagonal to ensure that the diagonal elements are the same as in Eq. 5.7. For simplicity, the off-diagonal elements are unmodified. Apart from simplicity, a further argument for this choice is $z_{IJ} = 0$, as the RHS of the z vector equation is in fact the response of energy to orbital rotations, and interfragment orbital rotation is forbidden at the frozen level. In this way, the new model is consistent with the previous one, since if the energy gap between different local excitations is large (compared to the magnitude of coupling), the eigenvalues of Eq. 5.12 are just the diagonal elements, i.e., the frozen energies. The other extreme is that all local excitations are degenerate.

In the simplest case of two identical fragments each contributing one state, we have a 2×2 generalized eigenvalue problem:

$$\begin{pmatrix} \omega_{\mathrm{FRZ}} & V \\ V & \omega_{\mathrm{FRZ}} \end{pmatrix} \begin{pmatrix} c_1 \\ c_2 \end{pmatrix} = \omega_{\mathrm{EXSP}} \begin{pmatrix} 1 & S \\ S & 1 \end{pmatrix} \begin{pmatrix} c_1 \\ c_2 \end{pmatrix}$$

where V and S are the off-diagonal elements of the Hamiltonian $\mathcal{A}$ and the metric $\mathcal{G}$, respectively. The solution to this 2×2 problem is

$$\begin{aligned} |\Phi^{-}_{\mathrm{EXSP}}\rangle &= (|\Psi_1^*\Psi_2\rangle - |\Psi_1\Psi_2^*\rangle)/\sqrt{2(1-S)} \\ \omega^{-}_{\mathrm{EXSP}} &= \frac{(1+S)(\omega_{\mathrm{FRZ}} - V)}{1-S} \\ |\Phi^{+}_{\mathrm{EXSP}}\rangle &= (|\Psi_1^*\Psi_2\rangle + |\Psi_1\Psi_2^*\rangle)/\sqrt{2(1+S)} \\ \omega^{+}_{\mathrm{EXSP}} &= \frac{(1-S)(\omega_{\mathrm{FRZ}} + V)}{1+S} \end{aligned} \tag{5.13}$$

One can see that the two resulting states are fully delocalized, with the one state having lower excitation energy compared to the localized frozen states, the other state has an increased excitation energy. This shares the same spirit as the Frenkel exciton model.

ω_{EXSP}'s are the excitation energies taking the excitonic coupling effect into account, but are free of polarization and charge transfer. Therefore, we can define the excitonic splitting terms as the shift from excitation energies at the frozen level:

$$\Delta\omega^{\kappa}_{\mathrm{EXSP}} = \omega^{\kappa}_{\mathrm{EXSP}} - \omega^{\kappa}_{\mathrm{FRZ}} \tag{5.14}$$

Subsequently the polarization term can then be evaluated via ALMO-CIS/ALMO-TDDFT as

$$\begin{aligned} \Delta\omega^{\kappa}_{\mathrm{POL}} &= \omega^{\kappa}_{\mathrm{POL}} - \omega^{\kappa}_{\mathrm{EXSP}} \\ \Delta E^{\kappa}_{\mathrm{POL}} &= E^{\kappa}_{\mathrm{POL}} - E^{\kappa}_{\mathrm{EXSP}} \\ &= (E_{\mathrm{POL}} + \omega^{\kappa}_{\mathrm{POL}}) - (E_{\mathrm{FRZ}} + \omega^{\kappa}_{\mathrm{EXSP}}) \\ &= \Delta E_{\mathrm{POL}} + \Delta\omega^{\kappa}_{\mathrm{POL}} \end{aligned} \tag{5.15}$$

To summarize, the new EDA scheme requires computing five different energies that correspond to progressively weaker constraints: (1) isolated fragment energies ($E^{\kappa}_{\mathrm{frag}}$); (2) the frozen energy ($E^{\kappa}_{\mathrm{FRZ}}$), which is the energy of the supersystem subject to the constraint that the fragments keep their orbitals and amplitudes unchanged; (3) the excitonic-splitting energy ($E^{\kappa}_{\mathrm{EXSP}}$), which takes the coupling between frozen fragment excited states into account; (4) the energy of polarized states ($E^{\kappa}_{\mathrm{POL}}$) evaluated with ALMO-CIS/ALMO-TDDFT; (5) the full system energy (E^{κ}) evaluated without any constraint. Every time we move to the next level (i.e. to a weaker constraint) the resulting energy change is designated as an EDA term. Among the four EDA terms, the excitonic-splitting term is unique to excited states (in other words, for the ground state $E_{\mathrm{EXSP}} = 0$). The other three terms (FRZ, POL and CT) all involve a contribution from the ground state (ΔE, obtained from the ground state ALMO-EDA) as well as a correction arising from the excitation energies ($\Delta\omega^{\kappa}$) that is state-specific.

5.2.3 State-tracking in EDA

Extra caution should be taken when multiple states are involved in EDA. Previously, for systems whose excitations are significantly different, we only focused on the lowest states, which are mainly localized on one fragment and minimally mixed with states on other fragments. Now as the EDA is performed for M excited states, the situation becomes more complicated. There is a straightforward one-to-one mapping only between the isolated fragment states and the frozen states. Defining this mapping is potentially problematic at EDA levels where states are delocalized (EXSP, POL, CT). One cannot simply track state indexes, or even look at just the lowest M states if, say, there is a low-lying charge-resonance state, or the M states switch order since the interactions may affect different states unequally. To make the EDA usable in these interesting and complex settings, we require that the final states maintain the character of the reference isolated fragment states. In other words, it is desirable to be able to view the interfragment interaction as akin to a perturbation, even though we are now allowing a degenerate perturbation theory description.

The problem is addressed by finding the states that most resemble the reference, where the resemblance is measured by the overlaps between states. For example, if Φ_κ is the κ state at one intermediate level, and $\tilde{\Phi}_{\kappa'}$ is the κ' state at another level, the overlap between them is computed as:

$$G_{\kappa\kappa'} = \langle \Phi^\kappa | \tilde{\Phi}^{\kappa'} \rangle = \sum_{ia} \sum_{i'a'} t_\kappa^{ia} S_{ii'} S_{aa'} \tilde{t}_{\kappa'}^{i'a'} \tag{5.16}$$

Here t and $\tilde{t}$ are amplitudes of Φ_κ and $\tilde{\Phi}_{\kappa'}$, respectively, $S_{ii'}$ and $S_{aa'}$ are the MO overlaps, which appear because the frozen, polarized and final wavefunctions use different MOs.

The magnitude of $G_{\kappa\kappa'}$ is between 0 and 1. If $G = |G_{\kappa\kappa'}|$ is close to 1, it means that the two states are very similar. We can keep track of the M states based on the G values: at each intermediate level (including the final), we look for the states that have maximum overlap with states at the previous level, and the EDA terms should take the differences between the pairs of states that overlap the most.

Considering a hypothetical 2×2 case as an example, based on the analysis mentioned above, $G_{11}(\text{FRZ}|\text{EXSP}) \approx G_{22}(\text{FRZ}|\text{EXSP}) \approx 0.5$, as the two local excitations have equal contributions to the EXSP states. After polarization, one may find that $G_{11}(\text{EXSP}|\text{POL}) \approx G_{22}(\text{EXSP}|\text{POL}) \approx 0.99$ while the other overlaps are close to 0. This indicates that the two lowest polarized states are closely related to the EXSP states, and thus the polarization terms would be $\Delta E^1_{\text{POL}} = E^1_{\text{POL}} - E^1_{\text{ESXP}}$, $\Delta E^2_{\text{POL}} = E^2_{\text{POL}} - E^2_{\text{ESXP}}$. Next, with CT included, assume that $G_{11}(\text{POL}|\text{FINAL}) \approx 0.95$, $G_{23}(\text{POL}|\text{FINAL}) \approx 0.80$, and that overlaps between other final states and the two lowest POL states are insignificant. One can then define $\Delta E^1_{\text{CT}} = E^1 - E^1_{\text{POL}} + \Delta E^1_{\text{BSSE}}$, $\Delta E^2_{\text{CT}} = E^3 - E^2_{\text{POL}} + \Delta E^2_{\text{BSSE}}$. The G values also hint at the relative importance of each EDA term. For example, in the above case, CT is likely to have more influence than POL. Note that in these analyses, at most M final states can eventually be mapped into the original fragment states, and these are the exciton resonance states. For states with strong CT character (e.g. the final state 2 above), one may consider

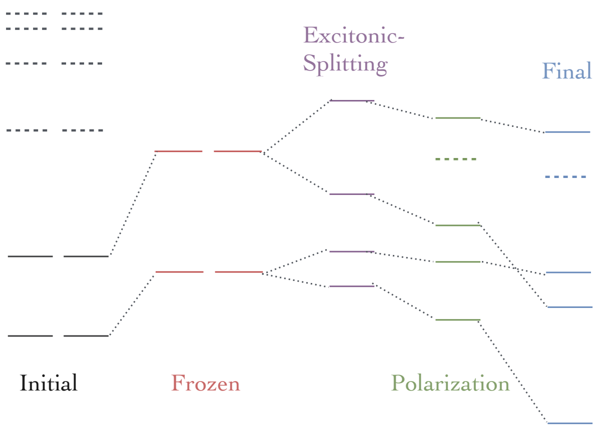

Figure 5.1: Illustration of EDA scheme.

utilizing $F1^{+}F2^{-}/F1^{-}F2^{+}$ instead of $F1^{*}F2/F1F2^{*}$ as reference states. However, we will not examine these charge resonance states any further in this work.

Before moving on, we refer the reader to Fig. 5.1 for a schematic illustration of the overall scheme associated with this EDA, where we exemplified how excited states at five distinct stages of constraint (initial, frozen, excitonic-splitting, polarized, and final) are related to each other as well as the possible effects of state crossing.

5.3 Application Examples

The generalized excited state ALMO-EDA has been implemented in a development version of the Q-Chem electronic structure program[106]. As tests of the new EDA scheme, we apply it to five systems: He_2^*, Ne_2^*, 2-pyridone dimer, benzene excimer and perylene excimer. For all TDDFT calculations, the Tamm-Dancoff approximation (TDA) is employed. All EDA results are CP-corrected, which slightly affects the CT term and the total interaction. For example, for the perylene excimer at the equilibrium structure of the lowest excited (B_{3g}) state, the BSSE estimated by subtracting the CP-corrected and uncorrected interaction energy is 0.125 eV, amounting to roughly 9% of the CP-corrected interaction energy for that state. The basis sets employed for other excimers are larger and therefore the magnitude of the BSSE is smaller in those cases (see Table S1 of the Supporting Information).

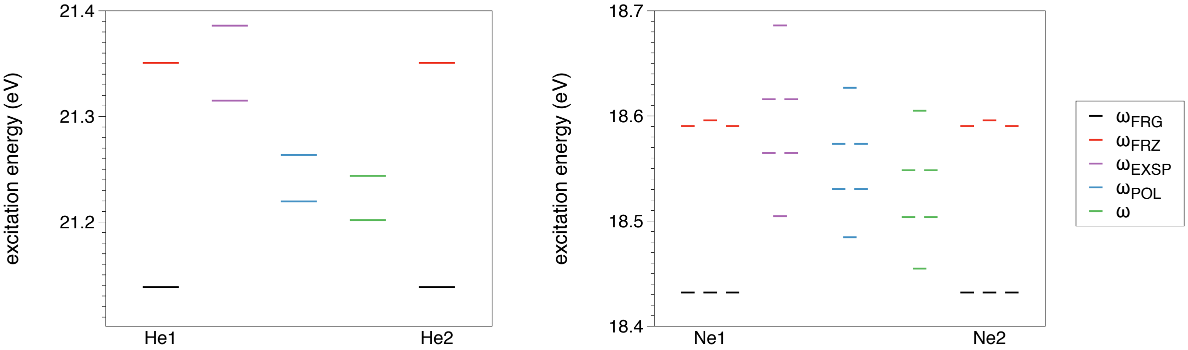

(a) He_2^* (b) Ne_2^*

Figure 5.2: Excitation energies at different EDA levels for (a) He_2^* and (b) Ne_2^*, The interatomic distance is chosen to be 3.0 Å for both cases. The two states for He_2^* correspond to $1s \to 2s$ monomer excitations. The six states for Ne_2^* are derived from the $2p_x \to 3s$, $2p_y \to 3s$ and $2p_z \to 3s$ monomer excitations.

5.3.1 Noble gas excimer: He_2^* and Ne_2^*

To explore how the new EDA scheme works, we first apply it to He_2^* and Ne_2^*, at an interatomic distance of 3.0 Å (close to the ground state equilibrium geometry). The calculation is performed with CIS (since it is self-interaction-free and these are Rydberg excitations) and a customized 6-311(2+)G basis, which includes two additional sets of diffuse functions to enable a better description of the Rydberg states. Fig. C.1 shows the energy levels of these two systems.

For He_2^*, we consider the two lowest singlet excited states (2^1A_{1g}, $^1A_{1u}$) that originate from the $1s \to 2s$ monomer state. The frozen states remain degenerate, but their excitation energies are 0.212 eV higher than the isolated monomer states. This can be explained by the fact that Pauli repulsion is more unfavorable for the excited states as the electronic density becomes more diffuse upon excitation ($\Delta E_{\mathrm{PAULI}} = 0.001$ eV, $\Delta E^{1,2}_{\mathrm{PAULI}} = 0.269$ eV, $\Delta\omega^{1,2}_{\mathrm{PAULI}} = 0.268$ eV). The splitting of the two states starts at the excitonic coupling stage, with the excitation energy of one state lowered by 0.035 eV, and the other raised by 0.035 eV. When polarization and charge transfer are incorporated subsequently, the excitation energies of both states red-shift, while the splitting is still present.

In the Ne_2^* case, as each monomer has three degenerate excitations, $2p_x \to 3s$, $2p_y \to 3s$ and $2p_z \to 3s$, six fragment states are taken into account. In the supersystem, the two $2p_z \to 3s$ excitations are inequivalent to $2p_x \to 3s$ and $2p_y \to 3s$ (the z axis is along the vector between Ne atoms), thus their frozen states are slightly higher in energy than the other four. The six states further split when they are allowed to mix. The lowest and highest excitonic states (of A_{1g} and A_{1u} symmetries, respectively) are the in-phase and out-of-phase combination of two fragment $2p_z \to 3s$ excitations, while the middle four states (two E_{1g} and two E_{1u}) come from $2p_x \to 3s$ and $2p_y \to 3s$ excitations. This can be confirmed by the linear combination coefficients solved from Eq. 5.12. Like the He_2^* case, all six states are

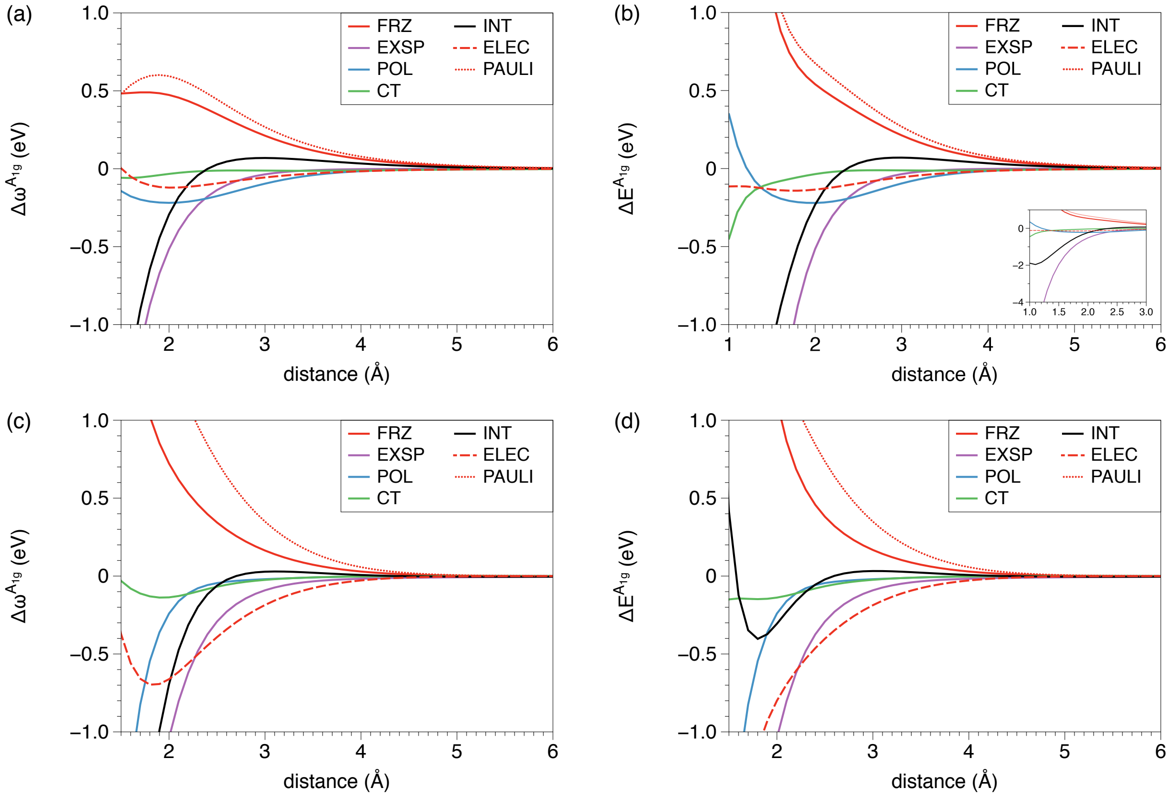

Figure 5.3: EDA results for the lowest singlet excited state (2^1A_{1g}) of He_2^* and Ne_2^* computed at different interatomic distances. (a) Decomposition of the excitation energy of He_2^* relative to the $1s \rightarrow 2s$ excitation energy of an isolated He atom. (b) Decomposition of the excited state interaction energy of He_2^* relative to separated He^* and He. (c) Same format as (a) but for Ne_2^* (d) Same format as (b) but for Ne_2^*.

stabilized by polarization and charge transfer.

Although the EDA terms are generally small at 3.0 Å for both He_2^* and Ne_2^*, the picture can be quite different at the equilibrium distances for the excited states. For He_2^*, the equilibrium is at 1.1 Å, with a well depth of 1.96 eV. For Ne_2^*, the equilibrium is at 1.8 Å, with a well depth of 0.40 eV. The energy levels (as in Fig. C.1) evaluated at the excimer equilibrium distances can be found in the Supporting Information (Fig. S1), where the excitation energy splittings due to excitonic coupling are much larger. The effects of POL and CT also vary significantly: by contrast with Fig. C.1, they do not always lower the excitation energies, and crossing of the higher-energy $2p_z \rightarrow 3s$ and $2p_{x(y)} \rightarrow 3s$ states occurs in Ne_2^* when CT is included.

Before moving on, we want to briefly discuss how to choose the fragment states. In particular, how many local excitations should be taken as the basis in Eq. 5.12? Let us consider what happens if the six $1s \rightarrow 2p$ excitations are also included for He_2^*. Solving the 8×8 generalized eigenvalue problem instead, we find that the results are different from

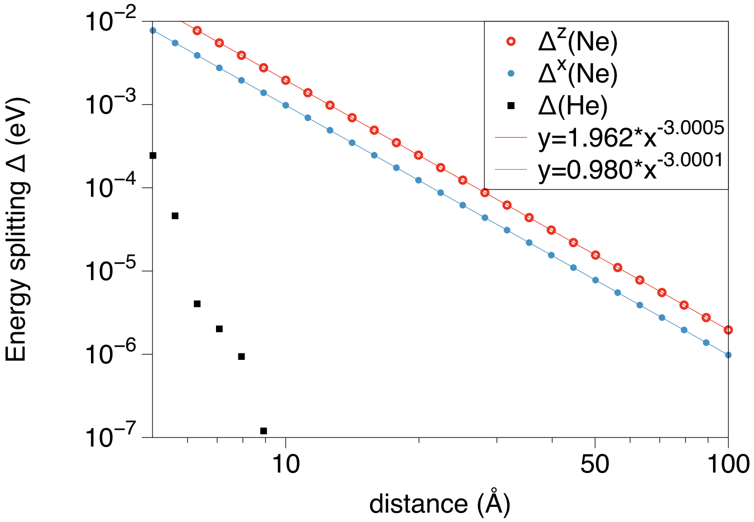

Figure 5.4: Log-log plot of excitonic splitting, Δ, in the lowest singlet excited states of He_2 and Ne_2 at large interatomic distances ($R > 5$ Å). Δ is calculated as $\Delta = |\Delta\omega^-_{\text{EXSP}}| + |\Delta\omega^+_{\text{EXSP}}|$, where $\Delta\omega^-_{\text{EXSP}}$ and $\Delta\omega^+_{\text{EXSP}}$ are the excitonic coupling terms for the out-of-phase and in-phase states, respectively. Excitonic splitting in He_2^* (labeled as Δ; shown as black dots) exhibits rapid decay with R, while it exhibits R^{-3} polynomial decay in Ne_2^*, consistent with Eq. 5.17. For Ne_2^*, Δ^z (red dots) refers to the $2p_z \to 3s$ splitting, while Δ^x (blue dots) refers to the $2p_x \to 3s$ splitting.

those of the 2 × 2 case. $\omega^{1,2}_{\text{EXSP}}$ values are now quite close to $\omega^{1,2}_{\text{POL}}$, that is, $\Delta\omega^{1,2}_{\text{POL}} \approx 0$ ($\omega^1_{\text{EXSP}} = 21.221$ eV, $\omega^2_{\text{EXSP}} = 21.263$ eV, $\omega^1_{\text{POL}} = 21.220$ eV, $\omega^2_{\text{POL}} = 21.264$ eV). A careful examination of the eigenvectors can explain the origin of this change. The first two excitonic states contain contributions from both $1s \to 2s$ and $1s \to 2p_z$ excitations, as $|\Psi_1^{1s\to 2s}\rangle \pm |\Psi_2^{1s\to 2s}\rangle$ are of the same symmetry as $|\Psi_1^{1s\to 2p_z}\rangle \pm |\Psi_2^{1s\to 2p_z}\rangle$ (both are A_{1g}) and they can mix further with each other, which is effectively a relaxation of fragment amplitudes. In other words, a considerable amount of polarization is contained in $\Delta\omega^{1,2}_{\text{EXSP}}$, rendering $\Delta\omega^{1,2}_{\text{POL}}$ tiny. Therefore the best choice of the degenerate subspace from the viewpoint of isolating the excitonic splitting is the minimal space of two strictly degenerate states, rather than the expanded 8-dimensional space, which is at most quasi-degenerate. It may be interesting to using the present EDA to re-analyze the nature of states in larger helium clusters, where a band of $2s$-derived states and another band of $2p$-derived states are found.[71, 80, 102]

For Ne_2^*, although the EDA is performed on the six states all together, excitations of different symmetries (e.g. $2p_x \to 3s$ and $2p_z \to 3s$) are not allowed to mix. In fact, the 6×6 matrices in Eq. 5.12 are block-diagonal and each eigenvector has only two nonzero elements, corresponding to the excitation from the same $2p$ orbital of each Ne atom. This means that the EDA results are the same if we treat $2p_x \to 3s$, $2p_y \to 3s$ and $2p_z \to 3s$ separately.

We then investigate the distance dependence of EDA terms for the 2^1A_{1g} state of He_2^*, and the 2^1A_{1g} state of Ne_2^*. The results are shown in Fig. 5.3. These two states are the lowest dimer states of their respective systems at all distances we studied. It is clear that in the binding regime, the most favorable term is the excitonic splitting. The large value of $\Delta\omega_{\mathrm{EXSP}}$ leads to the formation of excimers while the ground states are repulsive. For both He_2^* and Ne_2^*, polarization and charge transfer have minimal effects on energies, especially at larger distances. This is consistent with the value of the overlaps, $\langle \Phi_{\mathrm{EXSP}} | \Phi_{\mathrm{POL}} \rangle$ and $\langle \Phi_{\mathrm{POL}} | \Phi_{\mathrm{FINAL}} \rangle$, which are very close to one. The long-range behavior of $\Delta\omega_{\mathrm{EXSP}}$, on the other hand, are different for He_2^* and Ne_2^*. Asymptotically, the energy splitting from excitonic coupling is proportional to the interaction between the two transition dipole moments of fragment excitations:

$$\Delta = \frac{2\mu_1\mu_2}{R^3} |(\cos(\theta_1 - \theta_2) - 3\cos\theta_1\cos\theta_2)| \tag{5.17}$$

where μ_1 and μ_2 are the magnitude of transition dipoles for non-interacting fragment 1 and 2, respectively. θ_1 and θ_2 are the angles between transition dipoles and the line connecting two fragments. For He_2^*, $\boldsymbol{\mu}(1s \to 2s) = \mathbf{0}$, and hence $\Delta\omega_{\mathrm{EXSP}}$ quickly decays to zero, although at short range it is the vital piece. As for Ne_2^*, monomer CIS calculations gives $\mu_1 = \mu_2 = 0.349$ a.u. Eq. 5.17 gives $\Delta^z = 1.959$ $(\mathrm{eV} \cdot \mathrm{\AA}^3) R^{-3}$ for the splitting between the two states with $2p_z \to 3s$ parentage ($\theta_1 = \theta_2 = 0$). The splitting between the two states with $2p_{x/y} \to 3s$ parentage ($\theta_1 = \theta_2 = 90°$) should be $\Delta^{x,y} = 0.979$ $(\mathrm{eV} \cdot \mathrm{\AA}^3) R^{-3}$. We plot the calculated Δ^z and Δ^x against R for $R > 5$ Å in Fig. 5.4, which shows excellent agreement with the predicted relations. Meanwhile, the energy splitting of He_2^* is also shown in Fig. 5.4, and decays fast with distance.

5.3.2 2-pyridone dimer

The 2-pyridone (2-PY) dimer, a complex formed through cyclic, double N–H$\cdots$O=C hydrogen bonds, is analogous to nucleotide base pairs. The S1/S2 exciton splitting in the 2-PY dimer has been investigated both experimentally and theoretically[228–232].

The ground state geometry of the 2-PY dimer (optimized at the ωB97X-D/6-311++G(d,p) level of theory[233]) is near-planar and has a C_{2h} symmetry (Fig. 5.5). The intermolecular center-of-mass distance R is found to be 5.25 Å.

With ωB97X-D/6-311++G(d,p), the first excitation energy of the monomer (using its geometry in the dimer) is found to be 4.738 eV. The lowest two excited states of the dimer system, whose excitation energies are 4.805 eV and 4.957 eV, respectively, correspond to the out-of-phase and in-phase coupling of the first monomer excitation:

$$\begin{aligned} S_1 : \Phi^{A_g} &= \Psi_1\Psi_2^* - \Psi_1^*\Psi_2 \\ S_2 : \Phi^{B_u} &= \Psi_1\Psi_2^* + \Psi_1^*\Psi_2 \end{aligned}$$

Note that S_1 and S_2 states have A_g and B_u symmetry, respectively. The calculated energy splitting (0.152 eV) is in fairly good agreement with the CC2 result (0.136 eV) by Sagvolden and coworkers[232], who found that density functionals with large fractions of exact exchange are necessary to reproduce the CC2 splittings. The influence of the percentage of exact

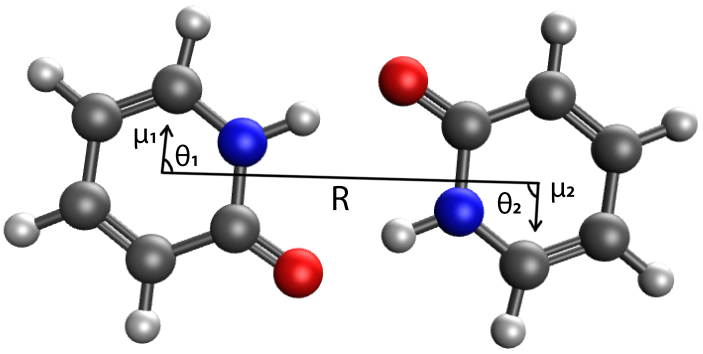

Figure 5.5: The structure of the ground state 2-PY dimer optimized with ωB97X-D/6-311++G(d,p).

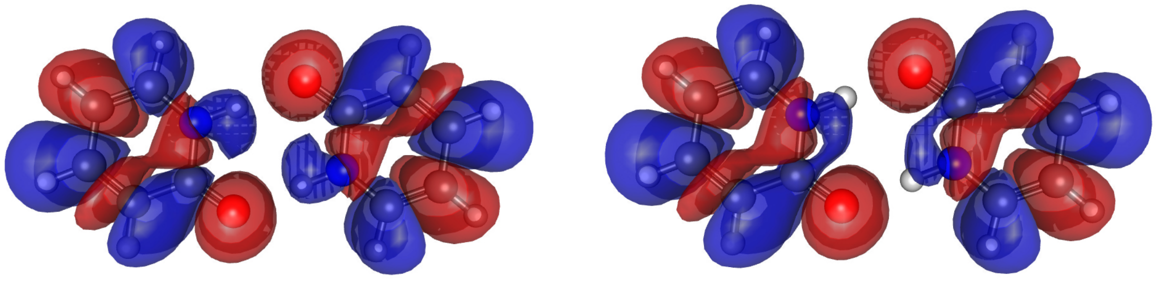

(a) S1

(b) S2

Figure 5.6: Difference density ($\Delta\rho = \rho^* - \rho$) plots for the lowest two excited states for the 2-PY dimer. The contour planes are placed at 0.0002 a.u.$^{-3}$, with positive ones in blue and negative ones in red.

exchange was further investigated by Neugebauer *et al.* using subsystem TDDFT calculations based on coupled frozen density embedding, [234, 235] which revealed that the effect of exact exchange is mainly on monomer transition densities. [236]

The EDA results are shown in Table C.2. The two hydrogen bonds in the ground state give binding energy of around 1 eV, with roughly 40% of the stabilization originating from CT, which is consistent with other hydrogen-bonded systems described by the ALMO-EDA.[237] Despite the excitonic splitting, the excimer EDA reveals that the complex is slightly destabilized in both S_1 and S_2 states compared to the ground state, mostly as a result of the less favorable electrostatics. This may be related to the weakening of hydrogen bonds. The difference densities $\Delta\rho = \rho^* - \rho$ of the excited states support this assumption, as the electronic densities are depleted on oxygen atoms and increased on hydrogen atoms upon excitation (see Fig. 5.6).

Table 5.1: EDA results of the 2-PY dimer (in eV), including the decomposition of interaction energies in the ground state and the first two excited states, as well as the shifts in excitation energies.

	FRZ	(ELEC/PAULI)	EXSP	POL	CT	INT
ΔE	-0.228	-1.610/1.381	-	-0.378	-0.437	-1.043
ΔE^{A_g}	-0.076	-1.483/1.406	-0.062	-0.381	-0.454	-0.973
$\Delta\omega^{A_g}$	0.152	0.127/0.025	-0.062	-0.004	-0.017	0.070
ΔE^{B_u}	-0.076	-1.483/1.406	0.062	-0.383	-0.424	-0.821
$\Delta\omega^{B_u}$	0.152	0.127/0.025	0.062	-0.005	0.013	0.222

The degeneracy of the monomer excitations breaks once the two states delocalize. The splitting due to excitonic coupling is $\Delta = 2 \times 0.062$ eV $= 0.124$ eV, while the full calculation gives $\Delta = (0.222 - 0.070)$ eV $= 0.152$ eV, suggesting that the splitting caused by polarization and charge transfer (in this case, mainly CT) cannot be overlooked. We can also estimate the splitting based purely on the interaction between monomer transition dipoles, i.e, using Eq. 5.17. Based on our electronic structure calculation, $\mu_1 = \mu_2 = 1.161$ a.u., $\theta_1 = \theta_2 = 88.3°$, which gives $\Delta = 0.075$ eV at $R = 5.252$ Å. This is an underestimation compared to the exciton model, most likely because the exchange effect is absent in the dipole-dipole model. Our results qualitatively agree with the CC2/aug-cc-pVTZ results reported by Leutwyler *et al.*[229], in which a full *ab initio* calculation of vertical excitation energies predicted $\Delta = 1125$ cm^{-1}(0.139 eV), and the dipole-dipole model gave $\Delta = 745$ cm^{-1}(0.092 eV).

Finally, it is noteworthy that experimentally, as the out-of-phase transition is dipole-forbidden, one has to break the symmetry, typically by introducing isotopes, to observe the energy splitting. Leutwyler and coworkers measured the fluorescence emission of 2-PY dimer and found a splitting of 43.5 cm^{-1}(0.0053 eV[228], which is $\sim$ 25 times smaller than the *ab initio* value. They showed that by multiplying the pure electronic splitting with a quenching factor, $\Gamma = \exp(-\sum_i S_i)$, where S_i is the Huang-Rhys factor of the i-th vibrational coordinate, the experimental result can be nicely reproduced[231].

We also report the EDA results for the S_1 and S_2 states at their separately optimized geometries in the Supporting Information (Table S2). For S_1 and S_2, the intermolecular center-of-mass distances are 5.28 Å and 5.32 Å, respectively. The results, in general, are very similar to those reported in Table C.2. It is noteworthy that the EXSP terms at the S_1 and S_2 minima are of slightly larger magnitude than that calculated at the ground state minimum, despite the smaller intermolecular separation in the latter. This might be associated with variations of the monomer geometries in these optimized complex structures.

5.3.3 Benzene excimer

The smallest aromatic excimer is the benzene excimer. In its ground state, the parallel displaced configuration is most stable, while the sandwich configuration (with D_{6h} symmetry) is preferred in the excited state. At large distances, the lowest four states are the exciton resonance states, which originate from the two singlet excitation on each monomer (B_{2u}, B_{1u}):

$$\begin{aligned}
\Phi^{B_{1g}} &= \Psi_1^{A_{1g}}\Psi_2^{B_{2u}} - \Psi_1^{B_{2u}}\Psi_2^{A_{1g}} \\
\Phi^{B_{2u}} &= \Psi_1^{A_{1g}}\Psi_2^{B_{2u}} + \Psi_1^{B_{2u}}\Psi_2^{A_{1g}} \\
\Phi^{B_{2g}} &= \Psi_1^{A_{1g}}\Psi_2^{B_{1u}} - \Psi_1^{B_{1u}}\Psi_2^{A_{1g}} \\
\Phi^{B_{1u}} &= \Psi_1^{A_{1g}}\Psi_2^{B_{1u}} + \Psi_1^{B_{1u}}\Psi_2^{A_{1g}}
\end{aligned}$$

We performed EDA calculations on the D_{6h} dimers at varying intermolecular distances ranging from 2.6 Å to 6.0 Å. The monomer geometry is optimized with the ωB97X-D functional[233] and 6-311++G(d,p) basis[238] and remains unchanged in the scan of intermolecular separation. The EDA is performed at the TD-ωB97X-D/6-311++G(d,p) level of theory.

With the values of $\langle\Phi_{\text{EXSP}}|\Phi_{\text{POL}}\rangle$ and $\langle\Phi_{\text{POL}}|\Phi_{\text{FINAL}}\rangle$ in hand, we are able to track the four states listed above. The magnitude of the overlaps between excitonic states and polarized states are very close to 1 (> 0.97 for all distances and all four states), which implies minimal polarization. On the other hand, the overlaps between polarized states and final states are considerably smaller, especially when the two benzene molecules are close to each other. The smallest magnitude of POL-FINAL overlap is ~ 0.74. This is still adequate to indicate a one-to-one connection between the final state (i.e. including charge transfer effects) and the polarized states.

The EDA results for the B_{1g} state are shown in Fig. 5.7. The excitonic splitting effect is rather small, which is not surprising as the corresponding monomer state has zero transition dipole moment. Meanwhile, CT plays the most essential role. The large magnitude of $\Delta\omega_{\text{CT}}$ at binding region suggests that the stabilization effect of CT is much stronger in the excited state than in the ground state. The EDA results reveal a different mechanism for the formation of benzene excimer than the noble gas excimers, where the latter are mainly stabilized by the excitonic splitting effect. It was proposed that the formation of aromatic excimers is due to configuration mixing between ER states and CR states of the same symmetry. In 1965, Azumi and McGlynn[239] identified low-lying CR states of benzene dimer with B_{1g}, B_{2u}, B_{2g} and B_{1u} symmetries that can mix with the corresponding ER states. This is consistent with our results, as in the EDA procedure, the energy lowering due to CT mostly comes from removal of the constraint on excitation amplitudes (only intrafragment amplitudes can be nonzero), that is, allowing the charge-transfer type of configurations to be mixed into the wavefunctions.

We also obtain the potential energy curves of the ground state (A_{1g}) and four ER states with B_{1g}, B_{2u}, B_{2g} and B_{1u} symmetries (Fig. 5.8(c)). Significant binding is found for the B_{1g}

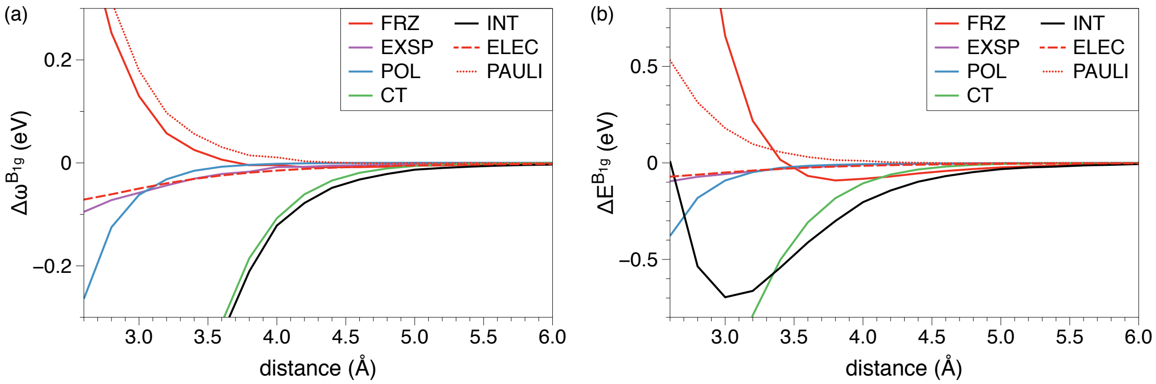

Figure 5.7: EDA results for the benzene dimer at different intermolecular distances. Decomposition of (a) the shifts in excitation energies and (b) excited state interaction energies for the B_{1g} state are presented.

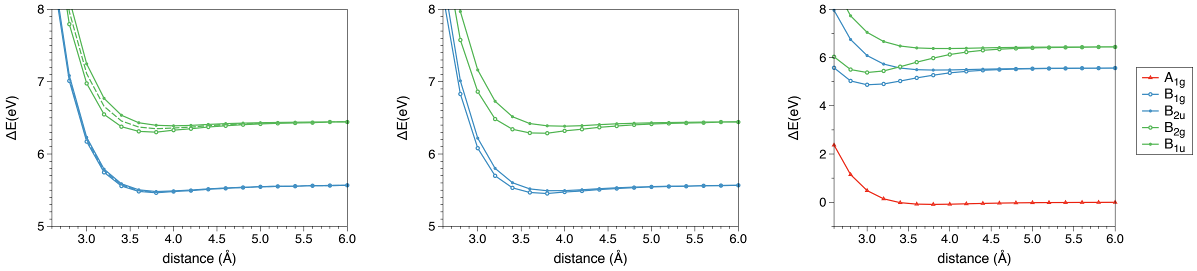

(a) EXSP/FRZ (b) POL (c) FINAL

Figure 5.8: The potential energy surfaces for the ground state (A_{1g}) and four excited states (B_{1g}, B_{2u}, B_{2g} and B_{1u}) of the benzene dimer (of D_{6h} symmetry). The energies are referenced to the energy of the ground-state monomers at infinite separation. The distance between two benzene rings is varied from 2.6 Å to 6.0 Å. (a): The energies after excitonic coupling (solid line) and frozen energies (dashed line); (b): The energies after polarization; (c): The energies of final wavefunctions (with CT included).

.

and B_{2g} states, which are more favored by CT than the other two excited states. A crossing between B_{2u} and B_{2g} is observed at ~ 3.3 Å. This crossing has been predicted by other authors, but at a different distance (~ 2.8 Å)[240]. Asymptotically, the energies of all states approach the corresponding monomer state limit. Potential energy curves are also plotted for other intermediate wavefunctions(Fig. 5.8(a),(b)). The polarized PESs show no strong binding for all states, and no state-crossing either, which again emphasizes the importance of CT. The excitonic curves deviate only slightly from the frozen curves (indicated by dashed lines in Fig. 5.8(a)), as both parent monomer states are dipole-forbidden.

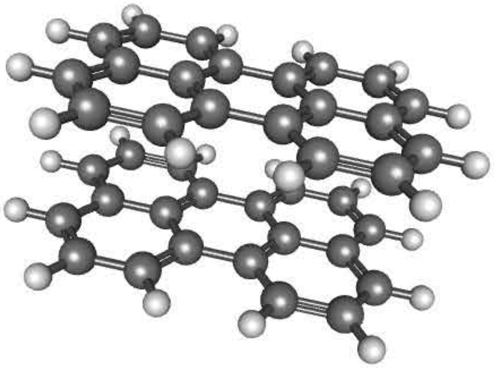

Figure 5.9: Structure of the D_{2h} perylene dimer constructed from monomer geometries optimized with ωB97X-D/6-31+G(d).

5.3.4 Perylene excimer

Now we turn to another aromatic excimer, the perylene excimer. EDA calculations are performed on the sandwich dimer with D_{2h} symmetry (Fig. 5.9). The monomer geometry optimization employs the ωB97X-D functional and 6-31+G(d) basis, and the EDA is performed at the TD-ωB97X-D/6-31+G(d) level of theory. We investigated the two states that come from the lowest monomer state (B_{2u}):

$$\begin{aligned} \Phi^{B_{3g}} &= \Psi_1^{A_{1g}}\Psi_2^{B_{2u}} - \Psi_1^{B_{2u}}\Psi_2^{A_{1g}} \\ \Phi^{B_{2u}} &= \Psi_1^{A_{1g}}\Psi_2^{B_{2u}} + \Psi_1^{B_{2u}}\Psi_2^{A_{1g}} \end{aligned} \tag{5.18}$$

Like the benzene dimer, the magnitude of overlaps imply small polarization and relatively large charge transfer, yet the EDA results (shown in Fig. 5.10) still reveal some unique features in the perylene case.

In contrast to benzene's $\Phi^{B_{1g}}$ states, the $\Phi^{B_{3g}}$ of perylene corresponds to a monomer state with large transition dipole moment (2.728 a.u.), thus we expect a strong stabilization effect from the exciton coupling. This is verified by the EDA results, shown in Fig. 5.10. Charge transfer is strongly favorable as well. However, the distance dependence of charge transfer and excitonic splitting are quite different. Close to the equilibrium distance (~ 3.4 Å), CT is dominant, and for this reason we regard it as the most crucial factor in the formation of perylene excimer. At larger distances, CT rapidly diminishes as it is believed to be correlated with the overlap between two fragments, which decays exponentially. The excitonic splitting term, as we discussed before, has an R^{-3} asymptotic behavior, allowing it to eventually surpass CT and become the most important term. Our EDA predicts this turnover at ~ 4.2 Å, where the curves corresponding to $\Delta\omega_{\mathrm{EXSP}}^{B_{3g}}$ and $\Delta\omega_{\mathrm{CT}}^{B_{3g}}$ cross.

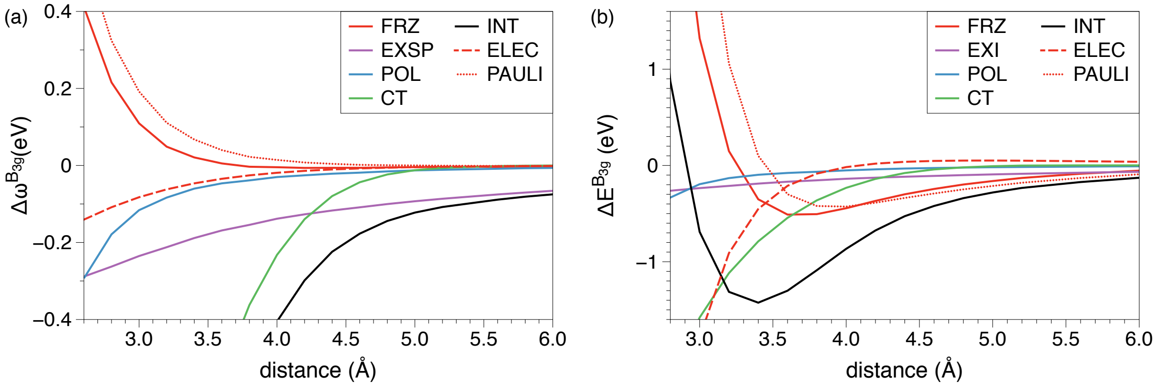

Figure 5.10: EDA results for the perylene dimer at different intermolecular distances. Decomposition of (a) the shift in excitation energies and (b) excited state interaction energies for the B_{3g} state are presented.

The potential energy surfaces for the ground state (A_{1g}) and two excited states (B_{3g}, B_{2u}) of the D_{2h} perylene dimer are shown in Fig. 5.11. The B_{3g} state has a binding energy that is notably larger than that of the ground state, owing to its more favorable CT. Meanwhile, the weaker binding of B_{2u} state is more likely due to dispersion rather than CT as it is already present at the frozen stage. Recalling that in the benzene dimer, the B_{2u} and B_{1u} states are not much favored by CT either, we wonder if it is a general trend that CT is stronger in the out-of-phase states than in the in-phase states. We also note that all binding energies are $\sim$ 0.9 eV stronger than those computed by Kuhlman and coworkers previously[241], who utilized BH&HLYP/6-31G(d) [242] level of theory. We attribute this discrepancy to the dispersion interaction, which is not accounted for by BH&HLYP. A comparison of EDA results using BH&HLYP and ωB97X-D is shown in Table S3 of the Supporting Information. At 3.6 Å, the major difference comes from the Pauli term of the ground state (about 1 eV more favorable with ωB97X-D), which, under the current scheme, incorporates all non-electrostatic effects at the frozen level, including dispersion.

5.4 Conclusion

In the present paper, we have generalized the previously proposed ALMO-EDA scheme[72] for intermolecular interactions involving excited molecules in exciplexes to include the excitonic coupling that can be important for describing excimers. The EDA is based on linear response theory (e.g. CIS, TDDFT), and it connects degenerate initial (reference) states of monomers to the final supersystem states of an excited complex.

The energy difference between the final and initial states defines the interaction energy, which is decomposed into frozen (FRZ), excitonic splitting (EXSP), polarization (POL) and charge-transfer (CT) terms. The partition is achieved by evaluating the energy of three intermediate states subject to different constraints, i.e., the frozen, excitonic splitting and

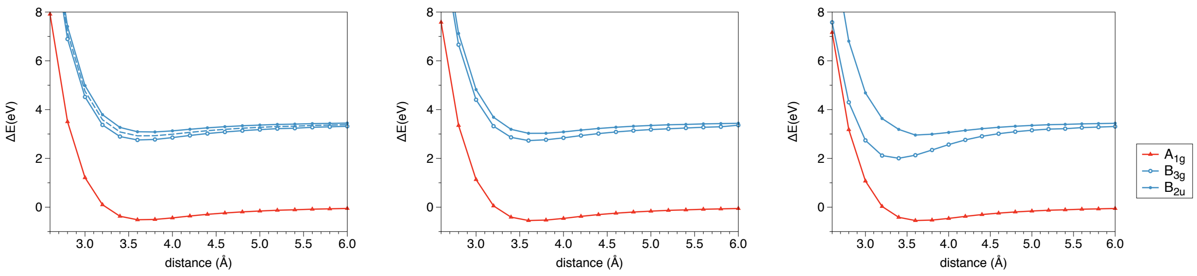

(a) EXSP/FRZ (b) POL (c) FINAL

Figure 5.11: The potential energy surfaces for the ground state (A_{1g}) and two excited states (B_{3g}, B_{2u}) of the D_{2h} perylene dimer. The energies are referenced to the energy of the ground-state monomers at infinite separation. The distance between two benzene rings is varied from 2.6 Å to 6.0 Å. (a): The energies after excitonic coupling (solid line) and frozen energies (dashed line); (b): The energies after polarization; (c): The energies of the final states (with CT included).

polarized states.

At the frozen level, both MOs and amplitudes are unrelaxed (taking their values from isolated fragment calculations), and each excited fragment state corresponds to one frozen state, constructed by embedding the fragment state into the environment of other ground state fragments. The exciton-splitting states are the new intermediate states introduced in this paper to describe the excitonic coupling effect in excimers. They are linear combinations of the frozen states, obtained by solving the secular equation in the basis of the frozen states. The ALMO-CIS wavefunctions[102] are utilized as the polarized states. In ALMO-CIS, intra-fragment relaxation of MOs and amplitudes is allowed and the excited states of the supersystem are constructed as superposition of intrafragment excitations.

From another point of view, more configurations are allowed to contribute to each supersystem wavefunction when the constraints are gradually removed: the excitonic states allow mixing between nearly degenerate local excitations on different fragments, the polarized states allow mixing of all intrafragment excitations, and the final states further incorporate all interfragment (CT-type) excitations.

While there is a one-to-one mapping between fragment states and frozen states, starting at the excitonic level, the mapping between states at different levels is non-trivial as the excitations become delocalized. We followed a “maximum overlap” scheme to track the states at each intermediate level, so that the new EDA scheme is able to treat multiple states in a reasonable way. Moreover, the overlap between intermediate states can often serve as a complementary validation for the EDA results.

With the generalization of the excited state EDA scheme, we are able to deal with situations where the excitation is delocalized across the whole system (e.g. excimers). We employed the EDA to study noble gas excimers including He_2^* and Ne_2^*, aromatic excimers including benzene and perylene excimer, as well as (2-pyridone)$_2$, a hydrogen bonded system. We are able to reveal the dominant forces that contribute to the formation of these excimers. For example, the excitonic splitting effect is important for noble gas excimers, while CT is significant in aromatic excimers. The EDA terms are also shown to have correct asymptotic behavior.

Although this work focused on excimer systems, the current EDA scheme is fully compatible with localized excitations (e.g. exciplexes), which was the main subject of our initial report.[72] In exciplexes, typically one fragment has an excited state whose excitation energy is significantly lower than possible excitations on other fragments, so this state only weakly couples with other fragment states because of the large energy gap. This will result in an EXSP term that is zero by definition, and the improved EDA scheme then reduces to its previous form.

Finally, we note that the current method still retains some limitations of the previous EDA scheme for exciplexes: (i) lack of an explicit separation of dispersion effects (they are lumped as part of the FRZ term); (ii) lack of a useful basis set limit for the POL and CT terms. The latter shortcoming has been discussed in the context of ground state EDA, [184, 187, 243, 244] and the fragment electric response function (FERF) approach [187] was proposed to address this issue. Using a given truncated multipole order for the FERFs, the convergence of POL (and thus CT) with respect to the size of the employed basis set can be restored. It is an interesting open question as to whether such the FERF approach can be usefully extended or generalized to excited states.

While the method presented here is already of practical use, the limitations mentioned above, as well as the quest for an EDA based on higher-level theories for excited states, raise non-trivial challenges for future work. Furthermore, we have always been taking local excitations as reference states and considering the EDA terms in a sequence that goes from (typically) longest to shortest range. Such a sequence is certainly not unique, and it may be interesting to develop an EDA scheme starting from charge-transfer states for cases where they are of greater importance.

Appendix A

Proof that ALMO-CIS is free of charge transfer.

Here we show that in the ALMO-CIS model, the Mülliken population on each fragment is conserved during excitation. In this section, we follow the Einstein summation convention for indicies that are summed over the whole space, but explicitly write out the summation if an index is only summed over a certain fragment. Also, a quantity that is built by projected virtuals is indicated by "~", for example, $\tilde{C}_a^\mu$ is the projected virtual coefficient while C_a^μ is the unprojected virtual coefficient.

The Mülliken population on a given fragment F_I is defined as

$$\rho_I = \sum_{\mu \in F_I} P^{\mu\nu} S_{\mu\nu} \tag{A.1}$$

where P is the density matrix. It has been proven that for ground state calculation with ALMO constraint (SCF(MI)), a fragment's Mülliken population remains the same as it is in an isolated fragment. So just need to prove that the difference density matrix of an excited state does not introduce any change on the fragment Mülliken population, i.e., $\sum_{\mu \in F_I} \Delta P^{\mu\nu} S_{\mu\nu} = 0$. The (unrelaxed) difference density matrix for ALMO-CIS is defined as follows:

$$\begin{aligned}
\Delta P^{\mu\nu} &= \Delta P_{OO}^{\mu\nu} + \Delta P_{VV}^{\mu\nu} \\
&= C_i^\mu P_{OO}^{ij} C_j^\nu + \tilde{C}_a^\mu P_{VV}^{ab} \tilde{C}_b^\nu \\
P_{OO}^{ij} &= -t^{\overset{\sqcap}{ia}} \tilde{S}_{ab} t^{\overset{\sqcap}{jb}} \\
P_{VV}^{ab} &= t^{\overset{\sqcap}{ia}} S_{ij} t^{\overset{\sqcap}{jb}}
\end{aligned} \tag{A.2}$$

The $t^{\overset{\sqcap}{ia}}$ here is the ALMO-CIS amplitude with i and a on a same fragment.

Now we have to do some math work. The sum over occupied part gives:

$$\begin{aligned}\sum_{\mu\in F_I}\Delta P^{\mu\nu}_{OO}S_{\mu\nu} &= -\sum_{\mu,i,a\in F_I} C^{\mu}_{i}t^{\overbracket{ia}}\tilde{S}_{ab}t^{\overbracket{jb}}C^{\nu}_{j}S_{\mu\nu}\\ &= -\sum_{i,a\in F_I} t^{\overbracket{ia}}\tilde{S}_{ab}t^{\overbracket{jb}}\sum_{\mu\in F_I}C^{\mu}_{i}S_{\mu\nu}C^{\nu}_{j}\\ &= -\sum_{i,a\in F_I} t^{\overbracket{ia}}\tilde{S}_{ab}t^{\overbracket{jb}}S_{ij}\end{aligned} \tag{A.3}$$

The last equal sign holds because the occupied MO coeffient is block diagonal, so the restriction on $\mu \in F_I$ can be dropped and $C^{\mu}_{i}S_{\mu\nu}C^{\nu}_{j}$ is just the occupied overlap metric S_{ij}.

The virtual part is a little more complicated because here we have some projected virtual coefficients, which are not block diagnoal.

$$\begin{aligned}\sum_{\mu\in F_I}\Delta P^{\mu\nu}_{VV}S_{\mu\nu} &= \sum_{\mu\in F_I}\tilde{C}^{\mu}_{a}t^{\overbracket{ia}}S_{ij}t^{\overbracket{jb}}\tilde{C}^{\nu}_{b}S_{\mu\nu}\\ &= \sum_{\mu,i,a\in F_I}\tilde{C}^{\mu}_{a}t^{\overbracket{ia}}S_{ij}t^{\overbracket{jb}}\tilde{C}^{\nu}_{b}S_{\mu\nu} + \sum_{\mu\in F_I}\sum_{F_K\neq F_I}\sum_{i,a\in F_K}\tilde{C}^{\mu}_{a}t^{\overbracket{ia}}S_{ij}t^{\overbracket{jb}}\tilde{C}^{\nu}_{b}S_{\mu\nu}\\ &= \sum_{i,a\in F_I}t^{\overbracket{ia}}S_{ij}t^{\overbracket{jb}}\sum_{\mu\in F_I}\tilde{C}^{\mu}_{a}S_{\mu\nu}\tilde{C}^{\nu}_{b} + \sum_{F_K\neq F_I}\sum_{i,a\in F_K}t^{\overbracket{ia}}S_{ij}t^{\overbracket{jb}}\sum_{\mu\in F_I}\tilde{C}^{\mu}_{a}S_{\mu\nu}\tilde{C}^{\nu}_{b}\end{aligned} \tag{A.4}$$

For the first sum, we notice $\tilde{C}^{\mu}_{a} = N_a C^{\mu}_{a}$, because the diagonal block of project virtuals takes contribution from only the unprojected virtuals. On the other hand, the overlap between projected virtual a and b is:

$$\begin{aligned}\tilde{S}_{ab} = \tilde{C}^{\mu}_{a}S_{\mu\nu}\tilde{C}^{\nu}_{b} &= N_a(C^{\mu}_{a} - C^{\mu}_{i}(\sigma^{-1})^{ij}S_{ia})S_{\mu\nu}\tilde{C}^{\nu}_{b}\\ &= N_a C^{\mu}_{a}S_{\mu\nu}\tilde{C}^{\nu}_{b} = \sum_{\mu\in F_I}N_a C^{\mu}_{a}S_{\mu\nu}\tilde{C}^{\nu}_{b}\end{aligned} \tag{A.5}$$

The first equal holds because the projected virtual does not overlap with the occupied, and the second equal comes from the fact that the unproject virtual coefficient are block diagonal. In the end, the first terms becomes $\sum_{i,a\in F_I} t^{\overbracket{ia}}S_{ij}t^{\overbracket{jb}}\tilde{S}_{ab}$.

As for the second term, since the off-diagonal projected virtual coefficient comes from the occupied, we have $\tilde{C}^{\mu}_{a} = -N_a C^{\mu}_{i}(\sigma^{-1})^{ij}S_{ja}, \mu, i \in F_I, a \in F_K \neq F_I$. The constraint $\mu \in F_I$ can then be dropped as C^{μ}_{i} is block diagonal. We then find an $\tilde{S}_{ib}$ in the second term, which is zero and so is the second term.

Eventually, we have $\sum_{\mu\in F_I}\Delta P^{\mu\nu}S_{\mu\nu} = 0$ because $-\sum_{\mu\in F_I}\Delta P^{\mu\nu}_{OO}S_{\mu\nu} = \sum_{\mu\in F_I}\Delta P^{\mu\nu}_{VV}S_{\mu\nu} = \sum_{i,a\in F_I} t^{\overbracket{ia}}\tilde{S}_{ab}t^{\overbracket{jb}}S_{ij}$.

Appendix B

Additional Information for EDA for exciplexes

Table B.1: EDA results for the pyridine- and pyrimidine-water complexes using CIS. Presented data (in eV), include the decomposition of interaction energies in the ground state (ΔE) and the $n{\rightarrow}\pi^*$ excited state (ΔE^*), as well as the shifts in excitation energies ($\Delta\omega$).

pyridine-water

		FRZ	(ELEC/PAULI)	POL	CT	INT
linear($n{\rightarrow}\pi^*$)	ΔE	-0.088	-0.204/0.116	-0.025	-0.010	-0.122
	ΔE^*	-0.017	-0.122/0.139	-0.013	-0.040	-0.036
	$\Delta\omega$	0.105	0.083/0.022	0.012	-0.030	0.087
top($n{\rightarrow}\pi^*$)	ΔE	-0.041	-0.169/0.210	-0.029	-0.024	-0.012
	ΔE^*	-0.015	-0.211/0.226	-0.030	-0.019	-0.034
	$\Delta\omega$	-0.026	-0.042/0.016	-0.001	0.005	-0.022

pyrimidine-water

		FRZ	(ELEC/PAULI)	POL	CT	INT
linear($n{\rightarrow}\pi^*$)	ΔE	-0.049	-0.540/0.491	-0.083	-0.070	-0.202
	ΔE^*	0.242	-0.334/0.576	-0.123	-0.191	-0.073
	$\Delta\omega$	0.291	0.206/0.085	-0.040	-0.121	0.129
top($n{\rightarrow}\pi^*$)	ΔE	0.039	-0.232/0.270	-0.034	-0.029	-0.025
	ΔE^*	-0.051	-0.228/0.279	-0.036	-0.045	-0.030
	$\Delta\omega$	0.013	0.004/0.009	-0.002	-0.016	-0.005

Appendix C

Additional Information for EDA for excimers

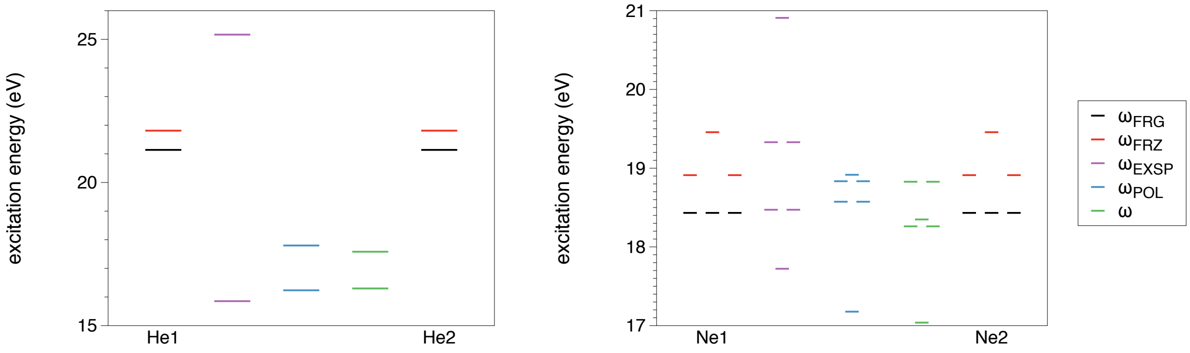

(a) He_2^*

(b) Ne_2^*

Figure C.1: Excitation energies at different EDA levels for (a) He_2^* at 1.1 Å and (b) Ne_2^* at 1.8 Å, which are the equilibrium distances of these two systems. The two states for He_2^* correspond to $1s \to 2s$ monomer excitations, and the six states for Ne_2^* are derived from the $2p_x \to 3s$, $2p_y \to 3s$ and $2p_z \to 3s$ monomer excitations.

Table C.1: Comparison of counterpoise-corrected (CP) and uncorrected (noCP) equilibrium interaction energies (in eV) for the lowest singlet excited state of each excimer. For each system, the calculations are performed with the same model chemistry as in the main paper. The BSSEs are estimated as the difference between $\Delta E^*_{\mathrm{INT}}$(CP) and $\Delta E^*_{\mathrm{INT}}$(noCP), and the percentage BSSEs are evaluated with respect to the CP-corrected interaction energies.

	$\Delta E^*_{\mathrm{INT}}$(noCP)	$\Delta E^*_{\mathrm{INT}}$(CP)	BSSE	%BSSE
He_2^*	-1.970	-1.962	0.008	0.4%
Ne_2^*	-0.430	-0.403	0.027	6.7%
(2-pyridone)$_2$	-1.008	-0.972	0.036	3.7%
(benzene)$_2$	-0.752	-0.696	0.056	8.0%
(perylene)$_2$	-1.550	-1.425	0.125	8.8%

Table C.2: EDA results (in eV) for the S1 (A_g) and S2 (B_u) states of the 2-PY dimer at their own equilibrium geometries. Decompositions of the ground and excited state interaction energies as well as the shifts in excitation energies are presented.

S1 (A_g) equilibrium geometry						
	FRZ	(ELEC/PAULI)	EXSP	POL	CT	INT
ΔE	-0.278	-1.632/1.354	-	-0.386	-0.437	-1.101
ΔE^{A_g}	-0.116	-1.490/1.374	-0.067	-0.378	-0.452	-1.013
$\Delta\omega^{A_g}$	0.162	0.142/0.019	-0.067	0.008	-0.014	0.088
S2 (B_u) equilibrium geometry						
	FRZ	(ELEC/PAULI)	EXSP	POL	CT	INT
ΔE	-0.353	-1.523/1.170	-	-0.349	-0.384	-1.087
ΔE^{B_u}	-0.197	-1.383/1.186	0.063	-0.344	-0.368	-0.846
$\Delta\omega^{B_u}$	0.156	0.139/0.017	0.063	0.005	0.016	0.240

Table C.3: EDA results for the perylene dimer at 3.6 Å, using BH&HLYP and ωB97X-D functionals. Presented data (in eV) include the decomposition of interaction energies in the ground state and the B_{2g} excited state, as well as the shifts in excitation energies. The two functionals qualitatively agree with each other except for the ground state Pauli term.

BH&HLYP

	FRZ	(ELEC/PAULI)	EXSP	POL	CT	INT
ΔE	0.506	-0.231/0.737	-	-0.021	0.031	0.517
$\Delta E^{B_{2g}}$	0.520	-0.273/0.793	-0.176	-0.073	-0.604	-0.333
$\Delta\omega^{B_{2g}}$	0.014	-0.042/0.056	-0.176	-0.053	-0.635	-0.850

ωB97X-D

	FRZ	(ELEC/PAULI)	EXSP	POL	CT	INT
ΔE	-0.516	-0.177/-0.339	-	-0.031	-0.001	-0.548
$\Delta E^{B_{2g}}$	-0.510	-0.211/-0.299	-0.169	-0.078	-0.544	-1.301
$\Delta\omega^{B_{2g}}$	0.005	-0.035/0.040	-0.169	-0.046	-0.543	-0.753

References

(1) Dirac, P. A. M., *The principles of quantum mechanics*; 27; Oxford university press: 1981.

(2) Sakurai, J. J.; Commins, E. D. Modern quantum mechanics, revised edition., 1995.

(3) Griffiths, D. J.; Schroeter, D. F., *Introduction to quantum mechanics*; Cambridge University Press: 2018.

(4) Born, M.; Oppenheimer, R. Zur quantentheorie der molekeln. *Ann. Phys. (Berl.)* **1927**, *389*, 457–484.

(5) Combes, J. M.; Duclos, P.; Seiler, R. In *Rigorous Atomic and Molecular Physics*, Velo, G., Wightman, A. S., Eds.; Springer US: Boston, MA, 1981, pp 185–213.

(6) Szabo, A.; Ostlund, N. S., *Modern quantum chemistry: introduction to advanced electronic structure theory*; Courier Corporation: 2012.

(7) Sherrill, C. D. An introduction to Hartree-Fock molecular orbital theory. *School of Chemistry and Biochemistry Georgia Institute of Technology* **2000**.

(8) Jensen, F., *Introduction to computational chemistry*; John wiley & sons: 2017.

(9) Dreuw, A.; Head-Gordon, M. Single-reference ab initio methods for the calculation of excited states of large molecules. *Chem. Rev.* **2005**, *105*, 4009–4037.

(10) Foresman, J. B.; Head-Gordon, M.; Pople, J. A.; Frisch, M. J. Toward a systematic molecular orbital theory for excited states. *J. Phys. Chem.* **1992**, *96*, 135–149.

(11) Surján, P. R. In *Second quantized approach to quantum chemistry: an elementary introduction*; Springer Science & Business Media: 2012.

(12) Davidson, E. R. The iterative calculation of a few of the lowest eigenvalues and corresponding eigenvectors of large real-symmetric matrices. *J. Comput. Phys.* **1975**, *17*, 87–94.

(13) Stratmann, R. E.; Scuseria, G. E.; Frisch, M. J. An efficient implementation of time-dependent density-functional theory for the calculation of excitation energies of large molecules. *J. Chem. Phys.* **1998**, *109*, 8218–8224.

(14) Pople, J.; Seeger, R; Krishnan, R. Variational configuration interaction methods and comparison with perturbation theory. *Int. J. Quantum Chem.* **1977**, *12*, 149–163.

(15) Knowles, P. J.; Handy, N. C. A new determinant-based full configuration interaction method. *Chem. Phys. Lett.* **1984**, *111*, 315–321.

(16) Møller, C.; Plesset, M. S. Note on an approximation treatment for many-electron systems. *Phys. Rev.* **1934**, *46*, 618.

(17) Krishnan, R; Pople, J. A. Approximate fourth-order perturbation theory of the electron correlation energy. *Int. J. Quantum Chem.* **1978**, *14*, 91–100.

(18) Purvis III, G. D.; Bartlett, R. J. A full coupled-cluster singles and doubles model: The inclusion of disconnected triples. *J. Chem. Phys.* **1982**, *76*, 1910–1918.

(19) Raghavachari, K.; Trucks, G. W.; Pople, J. A.; Head-Gordon, M. A fifth-order perturbation comparison of electron correlation theories. *Chem. Phys. Lett.* **1989**, *157*, 479–483.

(20) Head-Gordon, M.; Rico, R. J.; Oumi, M.; Lee, T. J. A doubles correction to electronic excited states from configuration interaction in the space of single substitutions. *Chem. Phys. Lett.* **1994**, *219*, 21–29.

(21) Stanton, J. F.; Bartlett, R. J. The equation of motion coupled-cluster method. A systematic biorthogonal approach to molecular excitation energies, transition probabilities, and excited state properties. *J. Chem. Phys.* **1993**, *98*, 7029–7039.

(22) Werner, H.-J.; Knowles, P. J. An efficient internally contracted multiconfiguration–reference configuration interaction method. *J. Chem. Phys.* **1988**, *89*, 5803–5814.

(23) Gagliardi, L.; Roos, B. O. Multiconfigurational quantum chemical methods for molecular systems containing actinides. *Chem. Soc. Rev.* **2007**, *36*, 893–903.

(24) Szalay, P. G.; Muller, T.; Gidofalvi, G.; Lischka, H.; Shepard, R. Multiconfiguration self-consistent field and multireference configuration interaction methods and applications. *Chem. Rev.* **2011**, *112*, 108–181.

(25) Roos, B. O. The complete active space self-consistent field method and its applications in electronic structure calculations. *Advances in Chemical Physics: Ab Initio Methods in Quantum Chemistry Part 2* **1987**, *69*, 399–445.

(26) Krylov, A. I. Spin-flip configuration interaction: an electronic structure model that is both variational and size-consistent. *Chem. Phys. Lett.* **2001**, *350*, 522–530.

(27) Krylov, A. I. Size-consistent wave functions for bond-breaking: the equation-of-motion spin-flip model. *Chem. Phys. Lett.* **2001**, *338*, 375–384.

(28) Krylov, A. I. Spin-flip equation-of-motion coupled-cluster electronic structure method for a description of excited states, bond breaking, diradicals, and triradicals. *Acc. Chem. Res* **2006**, *39*, 83–91.

(29) Hohenberg, P; Kohn, W. Inhomogeneous electron gas. *Phys. Rev.* **1964**, *136*, B864.

(30) Kohn, W.; Sham, L. J. Self-consistent equations including exchange and correlation effects. *Phys. Rev.* **1965**, *140*, A1133.

(31) Marques, M. A.; Gross, E. K. U. Time-dependent density functional theory. *Annu. Rev. Phys. Chem.* **2004**, *55*, 427–455.

(32) Van Gisbergen, S.; Snijders, J.; Baerends, E. Implementation of time-dependent density functional response equations. *Comput. Phys. Commun.* **1999**, *118*, 119–138.

(33) Casida, M. E. Time-dependent density-functional theory for molecules and molecular solids. *J. Mol. Struc-Theochem* **2009**, *914*, 3–18.

(34) Hirata, S.; Head-Gordon, M. Time-dependent density functional theory within the Tamm- Dancoff approximation. *Chem. Phys. Lett.* **1999**, *314*, 291–299.

(35) Dreuw, A.; Head-Gordon, M. Failure of time-dependent density functional theory for long-range charge-transfer excited states: the zincbacteriochlorin- bacteriochlorin and bacteriochlorophyll- spheroidene complexes. *J. Am. Chem. Soc.* **2004**, *126*, 4007–4016.

(36) Stone, A., *The theory of intermolecular forces*; OUP Oxford: 2013.

(37) Marini, A.; Munoz-Losa, A.; Biancardi, A.; Mennucci, B. What is solvatochromism? *J, Phys. Chem. B* **2010**, *114*, 17128–17135.

(38) Blandamer, M. J.; Fox, M. F. Theory and applications of charge-transfer-to-solvent spectra. *Chem. Rev.* **1970**, *70*, 59–93.

(39) Jortner, J.; Ottolenghi, M.; Stein, G. On the photochemistry of aqueous solutions of chloride, bromide, and iodide ions. *J. Phys. Chem.* **1964**, *68*, 247–255.

(40) Kloepfer, J. A.; Vilchiz, V. H.; Lenchenkov, V. A.; Bradforth, S. E. Femtosecond dynamics of photodetachment of the iodide anion in solution: resonant excitation into the charge-transfer-to-solvent state. *Chem. Phys. Lett.* **1998**, *298*, 120–128.

(41) Lehr, L; Zanni, M.; Frischkorn, C; Weinkauf, R.; Neumark, D. Electron solvation in finite systems: femtosecond dynamics of iodide·(water)$_n$ anion clusters. *Science* **1999**, *284*, 635–638.

(42) Sheu, W. S.; Rossky, P. J. Charge-transfer-to-solvent spectra of an aqueous halide revisited via computer simulation. *J. Am. Chem. Soc.* **1993**, *115*, 7729–7735.

(43) Serxner, D.; Dessent, C. E.; Johnson, M. A. Precursor of the I^-_{aq} charge-transfer-to-solvent (CTTS) band in $I^- \cdot (H_2O)_n$ clusters. *J. Chem. Phys.* **1996**, *105*, 7231–7234.

(44) Chen, H.-Y.; Sheu, W.-S. Precursors of the Charge-Transfer-to-Solvent States in $I^-(H_2O)_n$ Clusters. *J. Am. Chem. Soc.* **2000**, *122*, 7534–7542.

(45) Kim, J.; Lee, H. M.; Suh, S. B.; Majumdar, D; Kim, K. S. Comparative ab initio study of the structures, energetics and spectra of $X^- \cdot (H_2O)_{n=1-4}$ [X=F, Cl, Br, I] clusters. *J. Chem. Phys.* **2000**, *113*, 5259–5272.

(46) Baik, J.; Kim, J.; Majumdar, D; Kim, K. S. Structures, energetics, and spectra of fluoride–water clusters $F^-(H_2O)_n$, n=1–6: Ab initio study. *J. Chem. Phys.* **1999**, *110*, 9116–9127.

(47) Majumdar, D; Kim, J.; Kim, K. S. Charge transfer to solvent (CTTS) energies of small $X^-(H_2O)_{n=1-4}$ (X=F, Cl, Br, I) clusters: Ab initio study. *J. Chem. Phys.* **2000**, *112*, 101–105.

(48) Birks, J. Excimers. *Rep. Prog. Phys.* **1975**, *38*, 903.

(49) Rybak, S.; Jeziorski, B.; Szalewicz, K. Many-body symmetry-adapted perturbation theory of intermolecular interactions. H_2O and HF dimers. *J. Chem. Phys.* **1991**, *95*, 6576–6601.

(50) Jeziorski, B.; Moszynski, R.; Szalewicz, K. Perturbation theory approach to intermolecular potential energy surfaces of van der Waals complexes. *Chem. Rev.* **1994**, *94*, 1887–1930.

(51) Żuchowski, P. S.; Podeszwa, R.; Moszyński, R.; Jeziorski, B.; Szalewicz, K. Symmetry-adapted perturbation theory utilizing density functional description of monomers for high-spin open-shell complexes. *J. Chem. Phys.* **2008**, *129*, 084101.

(52) Szalewicz, K. Symmetry-adapted perturbation theory of intermolecular forces. *Wiley Interdiscip. Rev.: Comput. Mol. Sci.* **2012**, *2*, 254–272.

(53) Hohenstein, E. G.; Sherrill, C. D. Wavefunction methods for noncovalent interactions. *Wiley Interdiscip. Rev.: Comput. Mol. Sci.* **2012**, *2*, 304–326.

(54) Kitaura, K.; Morokuma, K. A new energy decomposition scheme for molecular interactions within the Hartree-Fock approximation. *Int. J. Quantum Chem.* **1976**, *10*, 325–340.

(55) Morokuma, K. Why do molecules interact? The origin of electron donor-acceptor complexes, hydrogen bonding and proton affinity. *Acc. Chem. Res.* **1977**, *10*, 294–300.

(56) Ziegler, T.; Rauk, A. On the calculation of bonding energies by the Hartree Fock Slater method. *Theor. Chem. Acc.* **1977**, *46*, 1–10.

(57) Ziegler, T.; Rauk, A. A theoretical study of the ethylene-metal bond in complexes between copper (1+), silver (1+), gold (1+), platinum (0) or platinum (2+) and ethylene, based on the Hartree-Fock-Slater transition-state method. *Inorg. Chem.* **1979**, *18*, 1558–1565.

(58) Von Hopffgarten, M.; Frenking, G. Energy decomposition analysis. *Wiley Interdiscip. Rev.: Comput. Mol. Sci.* **2012**, *2*, 43–62.

(59) Bagus, P. S.; Hermann, K; Bauschlicher Jr, C. W. A new analysis of charge transfer and polarization for ligand–metal bonding: Model studies of Al_4CO and Al_4NH_3. *J. Chem. Phys.* **1984**, *80*, 4378–4386.

(60) Stevens, W. J.; Fink, W. H. Frozen fragment reduced variational space analysis of hydrogen bonding interactions. Application to the water dimer. *Chem. Phys. Lett.* **1987**, *139*, 15–22.

(61) Su, P.; Li, H. Energy decomposition analysis of covalent bonds and intermolecular interactions. *J. Chem. Phys.* **2009**, *131*, 014102.

(62) Su, P.; Jiang, Z.; Chen, Z.; Wu, W. Energy decomposition scheme based on the generalized Kohn–Sham scheme. *J. Phys. Chem. A* **2014**, *118*, 2531–2542.

(63) Mo, Y.; Gao, J.; Peyerimhoff, S. D. Energy decomposition analysis of intermolecular interactions using a block-localized wave function approach. *J. Chem. Phys.* **2000**, *112*, 5530–5538.

(64) Mo, Y.; Song, L.; Lin, Y. Block-localized wavefunction (BLW) method at the density functional theory (DFT) level. *J. Phys. Chem. A* **2007**, *111*, 8291–8301.

(65) Mo, Y.; Bao, P.; Gao, J. Energy decomposition analysis based on a block-localized wavefunction and multistate density functional theory. *Phys. Chem. Chem. Phys.* **2011**, *13*, 6760–6775.

(66) Wu, Q.; Ayers, P. W.; Zhang, Y. Density-based energy decomposition analysis for intermolecular interactions with variationally determined intermediate state energies. *J. Chem. Phys.* **2009**, *131*, 164112.

(67) Wu, Q. Variational nature of the frozen density energy in density-based energy decomposition analysis and its application to torsional potentials. *J. Chem. Phys.* **2014**, *140*, 244109.

(68) Khaliullin, R. Z.; Cobar, E. A.; Lochan, R. C.; Bell, A. T.; Head-Gordon, M. Unravelling the origin of intermolecular interactions using absolutely localized molecular orbitals. *J. Phys. Chem. A* **2007**, *111*, 8753–8765.

(69) Horn, P. R.; Sundstrom, E. J.; Baker, T. A.; Head-Gordon, M. Unrestricted absolutely localized molecular orbitals for energy decomposition analysis: Theory and applications to intermolecular interactions involving radicals. *J. Chem. Phys.* **2013**, *138*, 134119.

(70) Horn, P. R.; Mao, Y.; Head-Gordon, M. Probing non-covalent interactions with a second generation energy decomposition analysis using absolutely localized molecular orbitals. *Phys. Chem. Chem. Phys.* **2016**, *18*, 23067–23079.

(71) Ge, Q.; Mao, Y.; White, A. F.; Epifanovsky, E.; Closser, K. D.; Head-Gordon, M. Simulating the absorption spectra of helium clusters (N=70, 150, 231, 300) using a charge transfer correction to superposition of fragment single excitations. *J. Chem. Phys.* **2017**, *146*, 044111.

(72) Ge, Q.; Mao, Y.; Head-Gordon, M. Energy decomposition analysis for exciplexes using absolutely localized molecular orbitals. *J. Chem. Phys.* **2018**, *148*, 064105.

(73) Ge, Q.; Head-Gordon, M. Energy decomposition analysis for excimers using absolutely localized molecular orbitals within time-dependent density functional theory and configuration interaction with single excitations. *J. Chem. Theory Comput.* **2018**, *14*, 5156–5168.

(74) Grebenev, S.; Toennies, J. P.; Vilesov, A. F. Superfluidity within a small helium-4 cluster: the microscopic Andronikashvili experiment. *Science* **1998**, *279*, 2083–2086.

(75) Wang, C. C.; Kornilov, O.; Gessner, O.; Kim, J. H.; Peterka, D. S.; Neumark, D. M. Photoelectron imaging of helium droplets doped with Xe and Kr atoms. *J. Phys. Chem. A* **2008**, *112*, 9356–9365.

(76) Peterka, D. S.; Kim, J. H.; Wang, C. C.; Neumark, D. M. Photoionization and photofragmentation of SF_6 in helium nanodroplets. *J. Phys. Chem. B* **2006**, *110*, 19945–19955.

(77) Joppien, M; Karnbach, R; Möller, T. Electronic excitations in liquid helium: The evolution from small clusters to large droplets. *Phys. Rev. Lett.* **1993**, *71*, 2654.

(78) Von Haeften, K.; Laarmann, T.; Wabnitz, H.; Möller, T. Observation of Atomiclike Electronic Excitations in Pure ^{3}He and ^{4}He Clusters Studied by Fluorescence Excitation Spectroscopy. *Phys. Rev. Lett.* **2001**, *87*, 153403.

(79) Von Haeften, K.; Laarmann, T.; Wabnitz, H.; Möller, T.; Fink, K. Size and isotope effects of helium clusters and droplets: identification of surface and bulk-Vvlume excitations. *J. Phys. Chem. A* **2011**, *115*, 7316–7326.

(80) Closser, K. D.; Head-Gordon, M. Ab initio calculations on the electronically excited states of small helium clusters. *J. Phys. Chem. A* **2010**, *114*, 8023–8032.

(81) Closser, K. D.; Gessner, O; Head-Gordon, M. Simulations of the dissociation of small helium clusters with ab initio molecular dynamics in electronically excited states. *J. Chem. Phys.* **2014**, *140*, 134306.

(82) Li, Q.; Li, Q.; Shuai, Z. Local configuration interaction single excitation approach: Application to singlet and triplet excited states structure for conjugated chains. *Synth. Met.* **2008**, *158*, 330–335.

(83) Miura, M.; Aoki, Y. Ab initio theory for treating local electron excitations in molecules and its performance for computing optical properties. *J. Comput. Chem.* **2009**, *30*, 2213–2230.

(84) Miura, M.; Aoki, Y. Linear-scaled excited state calculations at linear response time-dependent Hartree–Fock theory. *Mol. Phys.* **2010**, *108*, 205–210.

(85) Subotnik, J. E.; Dutoi, A. D.; Head-Gordon, M. Fast localized orthonormal virtual orbitals which depend smoothly on nuclear coordinates. *J. Chem. Phys.* **2005**, *123*, 114108.

(86) Li, Z.; Li, H.; Suo, B.; Liu, W. Localization of Molecular Orbitals: From Fragments to Molecule. *Acc. Chem. Res.* **2014**, *47*, 2758–2767.

(87) Kitaura, K.; Ikeo, E.; Asada, T.; Nakano, T.; Uebayasi, M. Fragment molecular orbital method: an approximate computational method for large molecules. *Chem. Phys. Lett.* **1999**, *313*, 701–706.

(88) Mochizuki, Y.; Koikegami, S.; Amari, S.; Segawa, K.; Kitaura, K.; Nakano, T. Configuration interaction singles method with multilayer fragment molecular orbital scheme. *Chem. Phys. Lett.* **2005**, *406*, 283–288.

(89) Mochizuki, Y.; Tanaka, K.; Yamashita, K.; Ishikawa, T.; Nakano, T.; Amari, S.; Segawa, K.; Murase, T.; Tokiwa, H.; Sakurai, M. Parallelized integral-direct CIS (D) calculations with multilayer fragment molecular orbital scheme. *Theor. Chem. Acc.* **2007**, *117*, 541–553.

(90) Chiba, M.; Fedorov, D. G.; Kitaura, K. Time-dependent density functional theory with the multilayer fragment molecular orbital method. *Chem. Phys. Lett.* **2007**, *444*, 346–350.

(91) Wu, F.; Liu, W.; Zhang, Y.; Li, Z. Linear-scaling time-dependent density functional theory based on the idea of from fragments to molecule. *J. Chem. Theory Comput.* **2011**, *7*, 3643–3660.

(92) Morrison, A. F.; You, Z.-Q.; Herbert, J. M. Ab Initio Implementation of the Frenkel–Davydov Exciton Model: A Naturally Parallelizable Approach to Computing Collective Excitations in Crystals and Aggregates. *J. Chem. Theory Comput.* **2014**, *10*, 5366–5376.

(93) Morrison, A. F.; Herbert, J. M. Low-scaling quantum chemistry approach to excited-state properties via an ab initio exciton model: Application to excitation energy transfer in a self-assembled nanotube. *J. Phys. Chem. Lett* **2015**, *6*, 4390–4396.

(94) Herbert, J. M.; Zhang, X.; Morrison, A. F.; Liu, J. Beyond Time-Dependent Density Functional Theory Using Only Single Excitations: Methods for Computational Studies of Excited States in Complex Systems. *Acc. Chem. Res.* **2016**, *49*, 931–941.

(95) Stoll, H.; Wagenblast, G.; Preuß, H. On the Use of Local Basis Sets for Localized Molecular Orbitals. *Theor. Chem. Acc.* **1980**, *57*, 169–178.

(96) Cullen, J. M. An Examination of the Effects of Basis Set and Charge Transfer in Hydrogen-Bonded Dimers with a Constrained Hartree-Fock Method. *Int. J. Quantum Chem.* **1991**, *40*, 193–207.

(97) Gianinetti, E.; Vandoni, A.; Famulari, A.; Raimondi, M. Extenstion of the SCF-MI Method to the Case of K Fragments one of which is an Open-Shell System. *Adv. Quantum Chem.* **1998**, *31*, 251–266.

(98) Nagata, T.; Takahashi, O.; Saito, K.; Iwata, S. Basis set superposition error free self-consistent field method for molecular interaction in multi-component systems: Projection operator formalism. *J. Chem. Phys.* **2001**, *115*, 3553–3560.

(99) Khaliullin, R. Z.; Head-Gordon, M.; Bell, A. T. An efficient self-consistent field method for large systems of weakly interacting components. *J. Chem. Phys.* **2006**, *124*, 204105.

(100) Mo, Y.; Gao, J.; Peyerimhoff, S. D. Energy decomposition analysis of intermolecular interactions using a block-localized wave function approach. *J. Chem. Phys.* **2000**, *112*, 5530–5538.

(101) Thirman, J.; Head-Gordon, M. An energy decomposition analysis for second-order Møller–Plesset perturbation theory based on absolutely localized molecular orbitals. *J. Chem. Phys.* **2015**, *143*, 084124.

(102) Closser, K. D.; Ge, Q.; Mao, Y.; Shao, Y.; Head-Gordon, M. Superposition of Fragment Excitations for Excited States of Large Clusters with Application to Helium Clusters. *J. Chem. Theory Comput.* **2015**, *11*, 5791–5803.

(103) Liu, J.; Herbert, J. M. An efficient and accurate approximation to time-dependent density functional theory for systems of weakly coupled monomers. *J. Chem. Phys.* **2015**, *143*, 034106.

(104) Head-Gordon, M.; Maslen, P. E.; White, C. A. A tensor formulation of many-electron theory in a nonorthogonal single-particle basis. *J. Chem. Phys.* **1998**, *108*, 616–625.

(105) Shao, Y. et al. Advances in methods and algorithms in a modern quantum chemistry program package. *Phys. Chem. Chem. Phys.* **2006**, *8*, 3172–3191.

(106) Shao, Y. et al. Advances in molecular quantum chemistry contained in the Q-Chem 4 program package. *Mol. Phys.* **2015**, *113*, 184–215.

(107) Ren, X.; Rinke, P.; Blum, V.; Wieferink, J.; Tkatchenko, A.; Sanfilippo, A.; Reuter, K.; Scheffler, M. Resolution-of-identity approach to Hartree–Fock, hybrid density functionals, RPA, MP2 and GW with numeric atom-centered orbital basis functions. *New J. Phys.* **2012**, *14*, 053020.

(108) Dunlap, B. I.; Connolly, J. W. D.; Sabin, J. R. On some approximations in applications of Xα theory. *J. Chem. Phys.* **1979**, *71*, 3396–3402.

(109) Vahtras, O.; Almlöf, J.; Feyereisen, M. W. Integral approximations for LCAO-SCF calculations. *Chem. Phys. Lett.* **1993**, *213*, 514–518.

(110) Keesom, W.; Taconis, K. Debije-scherrer exposures of liquid helium. *Physica* **1938**, *5*, 270–280.

(111) Callicoatt, B. E.; Forde, K; Jung, L. F.; Ruchti, T.; Janda, K. C. Fragmentation of ionized liquid helium droplets: A new interpretation. *J. Chem. Phys.* **1998**, *109*, 10195–10200.

(112) Feynman, R. P.; Hibbs, A. R.; Styer, D. F., *Quantum mechanics and path integrals*; Courier Corporation: 2005.

(113) Ceperley, D. M. Path integrals in the theory of condensed helium. *Rev. Mod. Phys.* **1995**, *67*, 279.

(114) Cleveland, C.; Landman, U.; Barnett, R. Energetics and structure of ^{4}He droplets at a finite temperature. *Phys. Rev. B* **1989**, *39*, 117.

(115) Calvo, F; Naumkin, F.; Wales, D. Interplay between charge and vibrational delocalization in cationic helium clusters. *J. Chem. Phys.* **2011**, *135*, 124308.

(116) Sindzingre, P.; Klein, M. L.; Ceperley, D. M. Path-integral Monte Carlo study of low-temperature ^{4}He clusters. *Phys. Rev. Lett.* **1989**, *63*, 1601.

(117) Aziz, R.; Nain, V.; Carley, J.; Taylor, W.; McConville, G. An accurate intermolecular potential for helium. *J. Chem. Phys.* **1979**, *70*, 4330–4342.

(118) Bussi, G.; Parrinello, M. Accurate sampling using Langevin dynamics. *Phys. Rev. E* **2007**, *75*, 056707.

(119) Ceriotti, M.; Parrinello, M.; Markland, T. E.; Manolopoulos, D. E. Efficient stochastic thermostatting of path integral molecular dynamics. *J. Chem. Phys.* **2010**, *133*, 124104.

(120) Peterka, D. S.; Kim, J. H.; Wang, C. C.; Poisson, L.; Neumark, D. M. Photoionization dynamics in pure helium droplets. *J. Phys. Chem. A* **2007**, *111*, 7449–7459.

(121) Herman, M.; Bruskin, E.; Berne, B. On path integral Monte Carlo simulations. *J. Chem. Phys.* **1982**, *76*, 5150–5155.

(122) Curutchet, C.; Mennucci, B. Quantum chemical studies of light harvesting. *Chem. Rev.* **2016**, *117*, 294–343.

(123) Chan, W.-L.; Berkelbach, T. C.; Provorse, M. R.; Monahan, N. R.; Tritsch, J. R.; Hybertsen, M. S.; Reichman, D. R.; Gao, J.; Zhu, X.-Y. The quantum coherent mechanism for singlet fission: Experiment and theory. *Acc. Chem. Res.* **2013**, *46*, 1321–1329.

(124) Yanai, T.; Tew, D. P.; Handy, N. C. A new hybrid exchange–correlation functional using the Coulomb-attenuating method (CAM-B3LYP). *Chem. Phys. Lett.* **2004**, *393*, 51–57.

(125) Rohrdanz, M. A.; Herbert, J. M. Simultaneous benchmarking of ground-and excited-state properties with long-range-corrected density functional theory. *J. Chem. Phys.* **2008**, *129*, 034107.

(126) Chai, J.-D.; Head-Gordon, M. Systematic optimization of long-range corrected hybrid density functionals. *J. Chem. Phys.* **2008**, *128*, 084106.

(127) Stein, T.; Kronik, L.; Baer, R. Reliable prediction of charge transfer excitations in molecular complexes using time-dependent density functional theory. *J. Am. Chem. Soc.* **2009**, *131*, 2818–2820.

(128) Baer, R.; Livshits, E.; Salzner, U. Tuned range-separated hybrids in density functional theory. *Annu. Rev. Phys. Chem.* **2010**, *61*, 85–109.

(129) Subotnik, J. E. Communication: Configuration interaction singles has a large systematic bias against charge-transfer states. *J. Chem. Phys.* **2011**, *135*, 071104.

(130) Liu, X.; Fatehi, S.; Shao, Y.; Veldkamp, B. S.; Subotnik, J. E. Communication: Adjusting charge transfer state energies for configuration interaction singles: Without any parameterization and with minimal cost. *J. Chem. Phys.* **2012**, *136*, 161101.

(131) Liu, X.; Ou, Q.; Alguire, E.; Subotnik, J. E. Communication: An inexpensive, variational, almost black-box, almost size-consistent correction to configuration interaction singles for valence excited states. *J. Chem. Phys.* **2013**, *138*, 221105.

(132) Liu, X.; Subotnik, J. E. The variationally orbital-adapted configuration interaction singles (VOA-CIS) approach to electronically excited states. *J. Chem. Theory Comput.* **2014**, *10*, 1004–1020.

(133) Gilbert, A. T.; Besley, N. A.; Gill, P. M. Self-consistent field calculations of excited states using the maximum overlap method (MOM). *J. Phys. Chem. A* **2008**, *112*, 13164–13171.

(134) Barca, G. M.; Gilbert, A. T.; Gill, P. M. Simple models for difficult electronic excitations. *J. Chem. Theory Comput.* **2018**, *14*, 1501–1509.

(135) Roos, B. O.; Taylor, P. R.; Siegbahn, P. E. M. A complete active space SCF method (CASSCF) using a density matrix formulated super-CI approach. *Chem. Phys.* **1980**, *48*, 157–173.

(136) Andersson, K.; Malmqvist, P.-Å.; Roos, B. O. Second-order perturbation theory with a complete active space self-consistent field reference function. *J. Chem. Phys.* **1992**, *96*, 1218–1226.

(137) Angeli, C.; Cimiraglia, R.; Evangelisti, S; Leininger, T; Malrieu, J.-P. Introduction of n-electron valence states for multireference perturbation theory. *J. Chem. Phys.* **2001**, *114*, 10252–10264.

(138) Broer, R; Hozoi, L; Nieuwpoort, W. Non-orthogonal approaches to the study of magnetic interactions. *Mol. Phys.* **2003**, *101*, 233–240.

(139) Thom, A. J.; Head-Gordon, M. Hartree–Fock solutions as a quasidiabatic basis for nonorthogonal configuration interaction. *J. Chem. Phys.* **2009**, *131*, 124113.

(140) Sundstrom, E. J.; Head-Gordon, M. Non-orthogonal configuration interaction for the calculation of multielectron excited states. *J. Chem. Phys.* **2014**, *140*, 114103.

(141) Mayhall, N. J.; Horn, P. R.; Sundstrom, E. J.; Head-Gordon, M. Spin–flip non-orthogonal configuration interaction: a variational and almost black-box method for describing strongly correlated molecules. *Phys. Chem. Chem. Phys.* **2014**, *16*, 22694–22705.

(142) Yost, S. R.; Head-Gordon, M. Size consistent formulations of the perturb-then-diagonalize Møller-Plesset perturbation theory correction to non-orthogonal configuration interaction. *J. Chem. Phys.* **2016**, *145*, 054105.

(143) Yost, S. R.; Head-Gordon, M. Efficient implementation of NOCI-MP2 using the resolution of the identity approximation with application to charged dimers and long C–C bonds in ethane derivatives. *J. Chem. Theory Comput.* **2018**, *14*, 4791–4805.

(144) Thom, A. J.; Head-Gordon, M. Locating multiple self-consistent field solutions: an approach inspired by metadynamics. *Phys. Rev. Lett.* **2008**, *101*, 193001.

(145) Stoll, H.; Wagenblast, G.; Preuβ, H. On the use of local basis sets for localized molecular orbitals. *Theor. Chem. Acc.* **1980**, *57*, 169–178.

(146) Van Voorhis, T.; Kowalczyk, T.; Kaduk, B.; Wang, L.-P.; Cheng, C.-L.; Wu, Q. The diabatic picture of electron transfer, reaction barriers, and molecular dynamics. *Annu. Rev. Phys. Chem.* **2010**, *61*, 149–170.

(147) Cembran, A.; Song, L.; Mo, Y.; Gao, J. Block-localized density functional theory (BLDFT), diabatic coupling, and their use in valence bond theory for representing reactive potential energy surfaces. *J. Chem. Theory Comput.* **2009**, *5*, 2702–2716.

(148) Ren, H.; Provorse, M. R.; Bao, P.; Qu, Z.; Gao, J. Multistate density functional theory for effective diabatic electronic coupling. *J. Phys. Chem. Lett.* **2016**, *7*, 2286–2293.

(149) Gao, J.; Grofe, A.; Ren, H.; Bao, P. Beyond Kohn–Sham approximation: hybrid multistate wave function and density functional theory. *J. Phys. Chem. Lett.* **2016**, *7*, 5143–5149.

(150) Grofe, A.; Qu, Z.; Truhlar, D. G.; Li, H.; Gao, J. Diabatic-at-construction method for diabatic and adiabatic ground and excited states based on multistate density functional theory. *J. Chem. Theory Comput.* **2017**, *13*, 1176–1187.

(151) Wu, Q.; Cheng, C.-L.; Van Voorhis, T. Configuration interaction based on constrained density functional theory: A multireference method. *J. Chem. Phys.* **2007**, *127*, 164119.

(152) Khaliullin, R. Z.; Bell, A. T.; Head-Gordon, M. Analysis of charge transfer effects in molecular complexes based on absolutely localized molecular orbitals. *J. Chem. Phys.* **2008**, *128*, 184112.

(153) Amos, A.; Hall, G. Single determinant wave functions. *Proc. R. Soc. A* **1961**, *263*, 483–493.

(154) Martin, R. L. Natural transition orbitals. *J. Chem. Phys.* **2003**, *118*, 4775–4777.

(155) Levine, D. S.; Horn, P. R.; Mao, Y.; Head-Gordon, M. Variational energy decomposition analysis of chemical bonding. 1. Spin-pure analysis of single bonds. *J. Chem. Theory Comput.* **2016**, *12*, 4812–4820.

(156) Levine, D. S.; Head-Gordon, M. Energy decomposition analysis of single bonds within Kohn–Sham density functional theory. *Proc. Natl. Acad. Sci.* **2017**, *114*, 12649–12656.

(157) Van Voorhis, T.; Head-Gordon, M. A geometric approach to direct minimization. *Mol. Phys.* **2002**, *100*, 1713–1721.

(158) Chai, J.-D.; Head-Gordon, M. Long-range corrected hybrid density functionals with damped atom–atom dispersion corrections. *Phys. Chem. Chem. Phys.* **2008**, *10*, 6615–6620.

(159) Difley, S.; Van Voorhis, T. Exciton/charge-transfer electronic couplings in organic semiconductors. *J. Chem. Theory Comput.* **2011**, *7*, 594–601.

(160) Maurice, D.; Head-Gordon, M. Configuration interaction with single substitutions for excited states of open-shell molecules. *Int. J. Quantum Chem.* **1995**, *56*, 361–370.

(161) Sears, J. S.; Sherrill, C. D.; Krylov, A. I. A spin-complete version of the spin-flip approach to bond breaking: What is the impact of obtaining spin eigenfunctions? *J. Chem. Phys.* **2003**, *118*, 9084–9094.

(162) Zhang, X.; Herbert, J. M. Spin-flip, tensor equation-of-motion configuration interaction with a density-functional correction: A spin-complete method for exploring excited-state potential energy surfaces. *J. Chem. Phys.* **2015**, *143*, 234107.

(163) Nakayama, A.; Taketsugu, T. Ultrafast nonradiative decay of electronically excited states of malachite green: Ab initio calculations. *J. Phys. Chem. A* **2011**, *115*, 8808–8815.

(164) Wu, E. C.; Ge, Q.; Arsenault, E. A.; Lewis, N. H.; Gruenke, N. L.; Head-Gordon, M. P.; Fleming, G. R. Two-dimensional electronic-vibrational spectroscopic study of conical intersection dynamics: an experimental and electronic structure study. *Phys. Chem, Chem. Phys.* **2019**.

(165) Tomasi, J.; Mennucci, B.; Cammi, R. Quantum mechanical continuum solvation models. *Chem. Rev.* **2005**, *105*, 2999–3094.

(166) Karelson, M. M.; Zerner, M. C. Theoretical treatment of solvent effects on electronic spectroscopy. *J. Phys. Chem.* **1992**, *96*, 6949–6957.

(167) Li, J.; Cramer, C. J.; Truhlar, D. G. Two-response-time model based on CM2/INDO/S2 electrostatic potentials for the dielectric polarization component of solvatochromic shifts on vertical excitation energies. *Int. J. Quantum Chem.* **2000**, *77*, 264–280.

(168) Singh, U. C.; Kollman, P. A. A combined ab initio quantum mechanical and molecular mechanical method for carrying out simulations on complex molecular systems: Applications to the CH_3Cl+Cl^- exchange reaction and gas phase protonation of polyethers. *J. Comput. Chem.* **1986**, *7*, 718–730.

(169) Field, M. J.; Bash, P. A.; Karplus, M. A combined quantum mechanical and molecular mechanical potential for molecular dynamics simulations. *J. Comput. Chem.* **1990**, *11*, 700–733.

(170) Senn, H. M.; Thiel, W. QM/MM methods for biomolecular systems. *Angew. Chem. Int. Ed.* **2009**, *48*, 1198–1229.

(171) Fradelos, G.; Wesołowski, T. A. Importance of the Intermolecular Pauli Repulsion in Embedding Calculations for Molecular Properties: The Case of Excitation Energies for a Chromophore in Hydrogen-Bonded Environments. *J. Phys. Chem. A* **2011**, *115*, 10018–10026.

(172) Nåbo, L. J.; Olsen, J. M. H.; Holmgaard List, N.; Solanko, L. M.; Wüstner, D.; Kongsted, J. Embedding beyond electrostaticsThe role of wave function confinement. *J. Chem. Phys.* **2016**, *145*, 104102.

(173) Arora, P.; Slipchenko, L. V.; Webb, S. P.; DeFusco, A.; Gordon, M. S. Solvent-induced frequency shifts: configuration interaction singles combined with the effective fragment potential method. *J. Phys. Chem. A* **2010**, *114*, 6742–6750.

(174) Slipchenko, L. V. Solvation of the excited states of chromophores in polarizable environment: orbital relaxation versus polarization. *J. Phys. Chem. A* **2010**, *114*, 8824–8830.

(175) Kosenkov, D.; Slipchenko, L. V. Solvent effects on the electronic transitions of p-nitroaniline: A QM/EFP study. *J. Phys. Chem. A* **2010**, *115*, 392–401.

(176) Nakata, H.; Fedorov, D. G.; Yokojima, S.; Kitaura, K.; Sakurai, M.; Nakamura, S. Unrestricted density functional theory based on the fragment molecular orbital method for the ground and excited state calculations of large systems. *J. Chem. Phys.* **2014**, *140*, 144101.

(177) Davydov, A, *Theory of molecular excitons*; Springer: 2013.

(178) Frenkel, J. On the transformation of light into heat in solids. I. *Phys. Rev.* **1931**, *37*, 17.

(179) Herbert, J. M.; Zhang, X.; Morrison, A. F.; Liu, J. Beyond Time-Dependent Density Functional Theory Using Only Single Excitations: Methods for Computational Studies of Excited States in Complex Systems. *Acc. Chem. Res.* **2016**, *49*, 931–941.

(180) Misquitta, A. J.; Podeszwa, R.; Jeziorski, B.; Szalewicz, K. Intermolecular potentials based on symmetry-adapted perturbation theory with dispersion energies from time-dependent density-functional calculations. *J. Chem. Phys.* **2005**, *123*, 214103.

(181) Jansen, G. Symmetry-adapted perturbation theory based on density functional theory for noncovalent interactions. *Wiley Interdiscip. Rev.: Comput. Mol. Sci.* **2014**, *4*, 127–144.

(182) Stone, A. J.; Misquitta, A. J. Charge-transfer in symmetry-adapted perturbation theory. *Chem. Phys. Lett.* **2009**, *473*, 201–205.

(183) Misquitta, A. J. Charge transfer from regularized symmetry-adapted perturbation theory. *J. Chem. Theory Comput.* **2013**, *9*, 5313–5326.

(184) Lao, K. U.; Herbert, J. M. Energy decomposition analysis with a stable charge-transfer term for interpreting intermolecular interactions. *J. Chem. Theory Comput.* **2016**, *12*, 2569–2582.

(185) Steinmann, S. N.; Corminboeuf, C.; Wu, W.; Mo, Y. Dispersion-corrected energy decomposition analysis for intermolecular interactions based on the BLW and dDXDM methods. *J. Phys. Chem. A* **2011**, *115*, 5467–5477.

(186) Gianinetti, E; Vandoni, I; Famulari, A; Raimondi, M Extension of the SCF-MI method to the case of K fragments one of which is an open-shell system. *Adv. Quantum Chem.* **1998**, *31*, 251–266.

(187) Horn, P. R.; Head-Gordon, M. Polarization contributions to intermolecular interactions revisited with fragment electric-field response functions. *J. Chem. Phys.* **2015**, *143*, 114111.

(188) Horn, P. R.; Mao, Y.; Head-Gordon, M. Defining the contributions of permanent electrostatics, Pauli repulsion, and dispersion in density functional theory calculations of intermolecular interaction energies. *J. Chem. Phys.* **2016**, *144*, 114107.

(189) Mao, Y.; Horn, P. R.; Head-Gordon, M. Energy decomposition analysis in an adiabatic picture. *Phys. Chem. Chem. Phys.* **2017**, *19*, 5944–5958.

(190) Thirman, J.; Head-Gordon, M. Efficient implementation of energy decomposition analysis for second-order møller-plesset perturbation theory and application to Anion-π Interactions. *J. Phys. Chem. A* **2016**.

(191) Krishnan, R.; Binkley, J. S.; Seeger, R.; Pople, J. A. Self-consistent molecular orbital methods. XX. A basis set for correlated wave functions. *J. Chem. Phys.* **1980**, *72*, 650–654.

(192) Frisch, M. J.; Pople, J. A.; Binkley, J. S. Self-consistent molecular orbital methods 25. Supplementary functions for Gaussian basis sets. *J. Chem. Phys.* **1984**, *80*, 3265–3269.

(193) Dunning Jr, T. H. Gaussian basis sets for use in correlated molecular calculations. I. The atoms boron through neon and hydrogen. *J. Chem. Phys.* **1989**, *90*, 1007–1023.

(194) Kendall, R. A.; Dunning Jr, T. H.; Harrison, R. J. Electron affinities of the first-row atoms revisited. Systematic basis sets and wave functions. *J. Chem. Phys.* **1992**, *96*, 6796–6806.

(195) Reimers, J. R.; Cai, Z.-L. Hydrogen bonding and reactivity of water to azines in their S_1 (n, π^*) electronic excited states in the gas phase and in solution. *Phys. Chem. Chem. Phys.* **2012**, *14*, 8791–8802.

(196) Buenker, R. J.; Peyerimhoff, S. D. Calculations on the electronic spectrum of water. *Chem. Phys. Lett.* **1974**, *29*, 253–259.

(197) Gingell, J.; Mason, N.; Zhao, H; Walker, I.; Siggel, M. VUV optical-absorption and electron-energy-loss spectroscopy of formamide. *Chem. Phys.* **1997**, *220*, 191–205.

(198) Nielsen, E. B.; Schellman, J. A. The absorption spectra of simple amides and peptides. *J. Phys. Chem.* **1967**, *71*, 2297–2304.

(199) Basch, H.; Robin, M.; Kuebler, N. Electronic spectra of isoelectronic amides, acids, and acyl fluorides. *J. Chem. Phys.* **1968**, *49*, 5007–5018.

(200) De Silva, N.; Willow, S. Y.; Gordon, M. S. Solvent induced shifts in the UV spectrum of amides. *J. Phys. Chem. A* **2013**, *117*, 11847–11855.

(201) Rablen, P. R.; Lockman, J. W.; Jorgensen, W. L. Ab initio study of hydrogen-bonded complexes of small organic molecules with water. *J. Phys. Chem. A* **1998**, *102*, 3782–3797.

(202) Jeffrey, G. A.; Saenger, W., *Hydrogen bonding in biological structures*; Springer Science & Business Media: 2012.

(203) Baker, E.; Hubbard, R. Hydrogen bonding in globular proteins. *Prog. Biophys. Mol. Biol.* **1984**, *44*, 97–179.

(204) Birks, J.; Munro, I. The fluorescence lifetimes of aromatic molecules. *Prog. React. Kinet.* **1967**, *4*, 239.

(205) Hopfield, J. J. New ultra-violet spectrum of helium. *Astrophys. J* **1930**, *72*, 133.

(206) Cheshnovsky, O.; Raz, B.; Jortner, J. Temperature dependence of rare gas molecular emission in the vacuum ultraviolet. *Chem. Phys. Lett.* **1972**, *15*, 475–479.

(207) Freeman, C.; McEwan, M.; Claridge, R.; Phillips, L. Band fluorescence of xenon. *Chem. Phys. Lett.* **1971**, *10*, 530–532.

(208) Oka, T; Rao, K. R.; Redpath, J.; Firestone, R. Mechanism for decay and spontaneous radiative decay constants of the lowest-lying attractive excited states of Ne_2, Ar_2, and Kr_2. *J. Chem. Phys.* **1974**, *61*, 4740–4746.

(209) Förster, T.; Kasper, K Ein konzentrationsumschlag der fluoreszenz des pyrens. *Berichte der Bunsengesellschaft für physikalische Chemie* **1955**, *59*, 976–980.

(210) Conlon, P.; Yang, C. J.; Wu, Y.; Chen, Y.; Martinez, K.; Kim, Y.; Stevens, N.; Marti, A. A.; Jockusch, S.; Turro, N. J.; Tan, W. Pyrene excimer signaling molecular beacons for probing nucleic acids. *J. Am. Chem. Soc.* **2008**, *130*, 336–342.

(211) Dembo, M.; Glushko, V.; Aberlin, M. E.; Sonenberg, M. A method for measuring membrane microviscosity using pyrene excimer formation. Application to human erythrocyte ghosts. *Biochim. Biophys. Acta, Biomembr.* **1979**, *552*, 201–211.

(212) Nagatoishi, S.; Nojima, T.; Juskowiak, B.; Takenaka, S. A pyrene-labeled G-quadruplex oligonucleotide as a fluorescent probe for potassium ion detection in biological applications. *Angew. Chem.* **2005**, *117*, 5195–5198.

(213) Focsaneanu, K.-S.; Scaiano, J. Potential analytical applications of differential fluorescence quenching: pyrene monomer and excimer emissions as sensors for electron deficient molecules. *Photochem. Photobiol. Sci* **2005**, *4*, 817–821.

(214) Schoenfisch, M. H.; Zhang, H.; Frost, M. C.; Meyerhoff, M. E. Nitric oxide-releasing fluorescence-based oxygen sensing polymeric films. *Anal. Chem.* **2002**, *74*, 5937–5941.

(215) Krueger, B. P.; Scholes, G. D.; Fleming, G. R. Calculation of couplings and energy-transfer pathways between the pigments of LH2 by the ab initio transition density cube method. *J. Phys. Chem. B* **1998**, *102*, 5378–5386.

(216) Li, X.; Parrish, R. M.; Liu, F.; Kokkila Schumacher, S. I.; Martínez, T. J. An Ab initio exciton model including charge-transfer excited states. *J. Chem. Theory Comput.* **2017**, *13*, 3493–3504.

(217) Hoffmann, M; Schmidt, K; Fritz, T; Hasche, T; Agranovich, V.; Leo, K. The lowest energy Frenkel and charge-transfer excitons in quasi-one-dimensional structures: application to MePTCDI and PTCDA crystals. *Chem. Phys.* **2000**, *258*, 73–96.

(218) Phipps, M. J. S.; Fox, T.; Tautermann, C. S.; Skylaris, C.-K. Energy decomposition analysis approaches and their evaluation on prototypical proteindrug interaction patterns. *Chem. Soc. Rev.* **2015**, *44*, 3177–3211.

(219) Pastorczak, E.; Corminboeuf, C. Perspective: Found in translation: Quantum chemical tools for grasping non-covalent interactions. *J. Chem. Phys.* **2017**, *146*, 120901.

(220) Plasser, F.; Lischka, H. Analysis of excitonic and charge transfer interactions from quantum chemical calculations. *J. Chem. Theory Comput.* **2012**, *8*, 2777–2789.

(221) Plasser, F.; Wormit, M.; Dreuw, A. New tools for the systematic analysis and visualization of electronic excitations. I. Formalism. *J. Chem. Phys.* **2014**, *141*, 024106.

(222) Plasser, F.; Bäppler, S. A.; Wormit, M.; Dreuw, A. New tools for the systematic analysis and visualization of electronic excitations. II. Applications. *J. Chem. Phys.* **2014**, *141*, 024107.

(223) Plasser, F.; Thomitzni, B.; Bäppler, S. A.; Wenzel, J.; Rehn, D. R.; Wormit, M.; Dreuw, A. Statistical analysis of electronic excitation processes: Spatial location, compactness, charge transfer, and electron-hole correlation. *J. Comput. Chem.* **2015**, *36*, 1609–1620.

(224) Spata, V. A.; Matsika, S. Role of excitonic coupling and charge-transfer states in the absorption and CD spectra of Adenine-based oligonucleotides investigated through QM/MM simulations. *J. Phys. Chem. A* **2014**, *118*, 12021–12030.

(225) Luzanov, A. V.; Casanova, D.; Feng, X.; Krylov, A. I. Quantifying charge resonance and multiexciton character in coupled chromophores by charge and spin cumulant analysis. *J. Chem. Phys.* **2015**, *142*, 224104.

(226) Casanova, D.; Krylov, A. I. Quantifying local exciton, charge resonance, and multiexciton character in correlated wave functions of multichromophoric systems. *J. Chem. Phys.* **2016**, *144*, 014102.

(227) Mao, Y.; Demerdash, O.; Head-Gordon, M.; Head-Gordon, T. Assessing ion-water interactions in the AMOEBA force field using energy decomposition analysis of electronic structure calculations. *J. Chem. Theory Comput.* **2016**, *12*, 54225437.

(228) Müller, A.; Talbot, F.; Leutwyler, S. S1/S2 exciton splitting in the (2-pyridone)$_2$ dimer. *J. Chem. Phys.* **2002**, *116*, 2836–2847.

(229) Ottiger, P.; Leutwyler, S.; Köppel, H. Vibrational quenching of excitonic splittings in H-bonded molecular dimers: the electronic Davydov splittings cannot match experiment. *J. Chem. Phys.* **2012**, *136*, 174308.

(230) Kopec, S.; Ottiger, P.; Leutwyler, S.; Köppel, H. Vibrational quenching of excitonic splittings in H-bonded molecular dimers: Adiabatic description and effective mode approximation. *J. Chem. Phys.* **2012**, *137*, 184312.

(231) Ottiger, P.; Köppel, H.; Leutwyler, S. Excitonic splittings in molecular dimers: why static ab initio calculations cannot match them. *Chem. Sci.* **2015**, *6*, 6059–6068.

(232) Sagvolden, E.; Furche, F.; Köhn, A. Forster energy transfer and davydov splittings in time-dependent density functional theory: Lessons from 2-pyridone dimer. *J. Chem. Theory Comput.* **2009**, *5*, 873–880.

(233) Chai, J. D.; Head-Gordon, M. Long-range corrected hybrid density functionals with damped atom-atom dispersion corrections. *Phys. Chem. Chem. Phys.* **2008**, *10*, 6615–6620.

(234) Casida, M. E.; Wesołowski, T. A. Generalization of the Kohn–Sham equations with constrained electron density formalism and its time-dependent response theory formulation. *Int. J. Quant. Chem.* **2004**, *96*, 577–588.

(235) Neugebauer, J. Couplings between electronic transitions in a subsystem formulation of time-dependent density functional theory. *J. Chem. Phys.* **2007**, *126*, 134116.

(236) König, C.; Neugebauer, J. Exciton coupling mechanisms analyzed with subsystem TDDFT: direct vs pseudo exchange effects. *J. Phys. Chem. B* **2013**, *117*, 3480–3487.

(237) Khaliullin, R. Z.; Bell, A. T.; Head-Gordon, M. Electron donation in the water-water hydrogen bond. *Chem. Eur. J.* **2009**, *15*, 851855.

(238) Frisch, M. J.; Pople, J. A.; Binkley, J. S. Self-consistent molecular-orbital methods.25. Supplementary functions for Gaussian-basis sets. *J. Chem. Phys.* **1984**, *80*, 3265–3269.

(239) Azumi, T.; McGlynn, S. Energy of excimer luminescence. III. Group theoretical considerations of molecular exciton and charge resonance states. *J. Chem. Phys.* **1965**, *42*, 1675–1680.

(240) Vala Jr, M. T.; Hillier, I. H.; Rice, S. A.; Jortner, J. Theoretical studies of transannular interactions. I. Benzene excimer fluorescence and the singlet states of the paracyclophanes. *J. Chem. Phys.* **1966**, *44*, 23–35.

(241) Kuhlman, T. S.; Lemke, H. T.; Sølling, T. I.; Velardez, G. F.; Henriksen, N. E.; Møller, K. B. Comment on "Theoretical Investigation of Perylene Dimers and Excimers and Their Signatures in X-Ray Diffraction". *J. Phys. Chem. A* **2009**, *113*, 6849–6850.

(242) Becke, A. D. A new mixing of Hartree–Fock and local density-functional theories. *J. Chem. Phys.* **1993**, *98*, 1372–1377.

(243) Azar, R. J.; Horn, P. R.; Sundstrom, E. J.; Head-Gordon, M. Useful lower limits to polarization contributions to intermolecular interactions using a minimal basis of localized orthogonal orbitals: Theory and analysis of the water dimer. *J. Chem. Phys.* **2013**, *138*, 084102.

(244) Mao, Y.; Ge, Q.; Horn, P. R.; Head-Gordon, M. On the computational characterization of charge-Transfer effects in noncovalently bound molecular complexes. *J. Chem. Theory Comput.* **2018**, *14*, 2401–2417.